2012

Marker-based head motion measurement system to mitigate motion artifacts in 3D cone-beam tomography

Ujjal Kumar Bhowmik

MARKER-BASED HEAD MOTION MEASUREMENT SYSTEM TO MITIGATE MOTION ARTIFACTS IN 3D CONE-BEAM TOMOGRAPHY

by

UJJAL KUMAR BHOWMIK

A DISSERTATION

Submitted in partial fulfillment of the requirements
for the degree of Doctor of Philosophy
in
The Department of Electrical and Computer Engineering
to
The School of Graduate Studies
of
The University of Alabama in Huntsville

HUNTSVILLE, ALABAMA

2012

In presenting this dissertation in partial fulfillment of the requirements for the degree of Doctor of Philosophy from The University of Alabama in Huntsville, I agree that the Library of this University shall make it freely available for inspection. I further agree that permission for extensive copying for scholarly purposes may be granted by my advisor or, in his/her absence, by the Chair of the Department or the Dean of the School of Graduate Studies. It is also understood that due recognition shall be given to me and to The University of Alabama in Huntsville in any scholarly use which may be made of any material in this dissertation.

(Student signature) (Date)

DISSERTATION APPROVAL FORM

Submitted by Ujjal Kumar Bhowmik in partial fulfillment of the requirements for the degree of Doctor of Philosophy in Electrical Engineering and accepted on behalf of the Faculty of the School of Graduate Studies by the dissertation committee.

We, the undersigned members of the Graduate Faculty of The University of Alabama in Huntsville, certify that we have advised and/or supervised the candidate on the work described in this dissertation. We further certify that we have reviewed the dissertation manuscript and approve it in partial fulfillment of the requirements for the degree of Doctor of Philosophy in Electrical Engineering.

01-11-2012
Committee Chair
(Date)

1/12/2012

1/12/2012

1/13/12

1/17/12

Department Chair

College Dean

3/7/12 Graduate Dean

ABSTRACT

The School of Graduate Studies
The University of Alabama in Huntsville

Degree: Doctor of Philosophy College/Dept. Engineering/Electrical and Computer Engineering.

Name of Candidate: Ujjal Kumar Bhowmik

Title: Marker-based Head Motion Measurement System to Mitigate Motion Artifacts in 3D Cone-beam Tomography

Head motion during Computed Tomographic (CT) brain imaging studies can adversely affect the reconstructed image by causing distortion, loss of resolution and other related problems. While there has been improvement in CT imaging systems over the past several years, there still remains a need to detect and mitigate motion artifacts in the clinical follow-ups of neurological patients with multiple sclerosis, tumors, and strokes. Failure to detect motion artifacts often leads to the wrong diagnosis of diseases. In this dissertation, a marker-based approach is proposed to detect and mitigate motion artifacts in three dimensional cone-beam CT systems without using any external motion tracking sensors. Motion parameters (the six degrees-of-freedom of motions), are estimated using a numerical optimization technique. Artifacts, caused by motions, are mitigated by using a modified form of the Feldkemp-Davis-Kress (FDK) algorithm (which uses the estimated motion parameters in a back-projection stage). The proposed approach has been evaluated on a modified three-dimensional Shepp-Logan phantom with a range of simulated motions. Simulation results demonstrate a quantitative and qualitative validation of motion detection and artifact mitigation techniques.

Abstract Approval: Committee Chair 

Department Chair 

Graduate Dean Rhonda Kay Gaede 3/7/12

ACKNOWLEDGMENTS

The author would like to thank his advisor, Dr. Reza Adhami, for his constant guidance, criticism and moral support during the development of this dissertation. This work could not have been possible without Dr. Adhami's continuous support.

The author would like to thank Dr. Zafar Iqbal, professor of CSE dept., Shahjalal University of Science and Technology (SUST), Bangladesh, for his invaluable suggestions and help during the critical phases of this research. The author is deeply indebted to Dr. Yasmeen Haque (professor, Dept. of Physics, SUST) and Dr. Susanta Kumar Das (professor, Dept. of Physics, SUST). Without their support and help the author could not have pursued his graduate studies in the United States.

The author is also grateful to Dr. Aniruddha Achari, Chief Scientist, Raytheon Pharmaceuticals, Huntsville, AL. From time to time, insightful discussions with Dr. Achari have stirred author's imagination and implanted the idea and inspiration of working on 3D computer tomography in author's mind.

The author would also like to thank Dr. John Stensby and Dr. Merv C. Budge for teaching him several important courses during his graduate studies. In particular, Dr. Budge's challenging problems and Dr. Stensby's rigorous mathematics transformed the author from a student to a scientist. The author would also like to thank Dr. Wells for his encouragement and moral support during the difficult times in graduate studies.

The financial support provided by the UAHuntsville is gratefully acknowledged. The author is grateful to the ECE dept. for providing him graduate teaching assistantship during his graduate studies. The author is also grateful to the Shahjalal University of Science and Technology for providing him study-leave with pay during his graduate studies.

The author would like to thanks the members of the dissertation committee, Dr. John L. Stensby, Dr. Merv C. Budge, Dr. Earl B. Wells and Dr. Daniel Lawrence.

Finally, pursuit of this scholastic work would not have been possible without the immense tolerance and unconditional support of the author's wife, Sarika Deb. The company of author's daughter, Anuprova Deb Bhowmik, made the hard times less stressful.

TABLE OF CONTENTS

LIST OF FIGURES

LIST OF TABLES

Dedicated to my father, late Akhil Chandra Bhowmik (died 19th January 2011). Although my father never went to school but always dreamed of seeing me achieve highest degree in the world.

CHAPTER 1

BACKGROUND AND SIGNIFICANCE

1.1 Introduction

X-ray Computed Tomography (CT), a widely used medical imaging modality, is the process of producing high resolution cross-sectional images of different parts of the human body. This process is done by performing mathematical manipulations (called reconstruction) on the X-ray projections taken around the body. X-ray Computed Tomography has also been used in radio astronomy, electron microscopy, geophysics, stress analysis, and non-destructive industrial applications. Since its invention in 1972 by G.N. Hounsfield and A.M. Cormack [1] [2], new developments have led to faster scanning, better dose usage, and improved image quality. With the advancement of digital computer technology (which facilitates the implementation of complex reconstruction algorithms), the current CT system is now capable of producing three-dimensional (3D) images of the internal structure of the head, chest, and other parts of the human body.

The CT reconstruction process is sensitive to inconsistencies in the X-ray projection data set. Patient motion during the data acquisition process remains one of the major causes of inconsistencies in the projection data set [3]. These inconsistencies will cause errors, called artifacts, in the final reconstructed image. Motion artifacts are

clinically significant because they may obscure one's anatomy from the image and make diagnosis difficult or impossible. In such cases, the radiologist may be forced to discard that particular image and rescan the patient.

In brain imaging, even with substantial head restraint, some amount of motion is inevitable, especially in less cooperative patients like children [4]. Head motion plays a significant role in causing artifacts such as blurring, doubling and loss of resolution in the reconstructed images [5]. While CT systems have been improved over the past several years, there still remains a need to detect and mitigate motion artifacts in clinical follow-ups of neurological patients with multiple sclerosis, tumors, and strokes, in which failure to detect motion artifacts often leads to the misdiagnosis of diseases [6]. In more extreme cases, the artifacts mimic pathology, which may cause the incorrect treatment of diseases. Therefore, it is imperative to detect, compensate or eliminate motion artifacts for diagnostic purposes. A good number of researchers have attempted to eliminate motion artifacts from the two-dimensional reconstruction process [3]. Methods of compensating for 3D motion artifacts have been studied to a comparatively limited degree. Moreover, the existing techniques have not found wide clinical acceptance because of their design complexities, lack of accuracy, and problems with implementation.

In this dissertation, a marker-based head motion measurement system has been proposed to estimate six degrees of freedom of head motion in a 3D cone beam CT system. The proposed system demonstrates a significant improvement in terms of accuracy, linearity, and range compared to the existing external sensor-based method. Mitigation of motion artifacts is achieved by using a modified form of the Feldkamp-Davis-Kress (FDK) algorithm, which uses estimated motion parameters during the

reconstruction process. The proposed method has been evaluated on a modified 3D Shepp-Logan phantom with a range of simulated motions. Simulation results demonstrate a quantitative and qualitative validation of motion detection and artifact mitigation techniques.

The remainder of this chapter is organized in the following sequences. First, a brief literature review of the chronological development of X-ray CT is given. Next, previous work done in the field of motion detection and artifact mitigation is reviewed. After that, the goal of this research is presented. Finally, a brief description of the organization of this dissertation is given.

1.2 Chronological Development of X-ray CT

According to the recent survey conducted by the American Association of Physicists in Medicine (AAPM) [7], the chronological development of X-ray CT in the last fifty years can be divided into the following four periods:

1.2.1. The Aurora of CT (Pre-1970s and 1970s)

The introduction of the first commercial CT scanner by Hounsfield in 1972 was a breakthrough in the field of medical imaging technology. It drew tremendous interest from researchers in academia and industry around the world. Researchers were quick to characterize, improve and apply this new technology, which led to a significant number of publications in that era. While substantial amounts of research were done to characterize the physical properties of CT scanners, image quality and image artifacts also occupied an important part of early research [8], [9]. The effect of the polychromatic

spectrum and beam hardening were also identified [10], [11]. The understanding of the polychromatic spectrum laid the foundation for developing dual-energy scanners [12]. The most significant outcome of that decade was the time efficient fan-beam imaging system, which formed the basis of today's cone-beam CT system [13].

1.2.2. The Stagnancy of CT (the late 1980s)

Following this flourishing decade of CT technology, momentum started falling off substantially after 1983, when another important imaging modality (Magnetic Resonance Imaging) came into the field. Many of the original CT researchers found themselves drawn into this new technology. However, building on research from the 1970s, some important works on reducing image artifacts (including motion artifacts, partial volume artifacts, metal artifacts and X-ray scatter artifacts) were developed [14]. A prototype megavolt CT system and Parker weighting scheme for reconstructing CT images from short scans were also reported in that period [15], [16]. Other significant advancements of that decade included the development of early practical cone-beam CT reconstruction techniques and the debut of the revolutionary FDK algorithm [17].

1.2.3. The Decade of Helical/Spiral CT (the 1990s)

In the early nineties, CT research activity continued to be limited. With the introduction of Spiral CT in the mid 1990s, renewed interest was created among the CT research community, which led to a surge of publications in the 2000s. While Spiral CT offered fast volume scanning, it also deliberately introduced motion inconsistencies in the projection data set. A good number of works on the analysis of image artifacts resulting

from data inconsistencies and algorithms were published in the early 1990s [18]. A great deal of research on understanding image quality issues, including noise, longitudinal resolution, and contrast, was also done during that period [19]. As image quality continued to improve because of this research, the Helical/Spiral method started to replace the conventional CT in clinics. Patient dose and how to reduce radiation dose was also a subject of major research at that time [20], [21], [22]. Soon, the single slice helical CT scanner evolved into a multi-slice CT scanner with a large scanning range, high speed, and very high spatial resolution. All these improvements made possible new applications for cardiac, lung, bone, liver and blood flow imaging [23]. Radiation therapy using CT also evolved during that period [24]. Developments in CT hardware, especially solid state detector technology, were also reported during the 1990s [25].

1.2.4. Volumetric Imaging and the Renaissance of CT (the 2000s)

In the early 2000s, manufacturers started adding more rows in the detector plate in an effort to cover more volume in CT images. Sixteen row detectors were available during 2001, with Toshiba introducing 256 row scanners in 2004 [26], [27]. As the number of detector rows continued to increase in Helical/spiral CT imaging, the interpolation method used to overcome projection data inconsistency in Spiral CT during the 1990s became inadequate due to the cone-beam artifacts introduced by a subtended cone-beam angle. A number of articles on approximate algorithms (based on the FDK algorithm for image reconstruction suitable for the Helican/Spiral CT scanner with multiple detector rows) were published in the early 2000s [28-30]. These approximate algorithms are the foundation for today's reconstruction algorithms used in almost all

commercial Helical/Spiral CT scanners. The significant Filtered Back Projection (FBP) based algorithm, (called Katsevich's algorithm) for exact reconstruction in Helical/Spiral CT was introduced in 2001 [31].

During the mid 2000s, the development of flat panel detectors, which allowed the acquisition of fully volumetric images, was an important advancement in cone-beam CT imaging systems and opened new doors with widespread applications for CT systems. For example, kilovoltage and megavoltage CT for radiation therapy, C-arm flat-panel CT for image guided surgery and interventional radiology are now widespread technologies [32], [33]. Another promising area of CT application is breast imaging as an extension of mammography, where it may offer better diagnosis with a total radiation dose no greater than that of a conventional two-view mammography [34]. However, larger scatter radiation generated in a body remains an area of increasing concern for cone-beam CT systems [35]. Larger scatter radiation reduces the contrast level and creates artifacts. Robust scatter correction algorithms and postpatient anti-scatter grids are two important areas of current research. The improvement of algorithms and hardware for compensating for image artifacts originating from geometric misalignment, beam hardening, and motion artifacts remain major areas of current CT research. Recently, there has been a growing interest in applying digital tomosynthesis to radiation therapy for the localization of radioactive seed and the imaging of the chest, breast, and joints [36], [37]. An emerging research field in current CT technology is the application of digital tomosynthesis using an onboard imager mounted on a treatment system for image-guided radiation therapy [38-43].

1.3 Prior Work on Motion Detection and Artifacts Mitigation

Since motion artifacts are clinically significant, many researchers over the last two decades have attempted to detect and mitigate motion artifacts from CT images. Although a great deal of effort has been invested in developing methods for compensating motion artifacts, only a limited amount of effort has been made to compensate for motion artifacts in a 3D CT system. A large volume of CT research articles on motion artifacts found in the literature are related to lung and cardiac motion artifact mitigation for a 2D CT system. These techniques can be categorized into the following two groups: prospective projection technique, in which projections are taken in such a way that motion is avoided during the scanning process, and retrospective technique, in which an attempt is made to a correct motion-corrupted projection data set [3].

1.3.1. Prospective Techniques

Breath-Holding: In chest imaging, artifacts originating from respiratory motion can be reduced by breath holding techniques. These techniques work well for conscious and cooperative patients. However, in the case of unconscious, elderly, or traumatic patients who cannot suspend respiration, breath-holding is not applicable [44].

Head Restraints: In brain imaging, motion artifacts are minimized by using head restraints. However, clinical reports suggest that some form of small and gradual head motion may occur during the scanning period, thereby creating significant motion artifacts [4].

Overscanning: Overscanning is another method for compensating motion artifacts; essentially, overscanning acquires projections for more than a full revolution and then blends projections that were acquired at the same angle [45]. Overscanning requires extra radiation doses and thus fails to remove artifacts originating from high frequency motions such as heartbeats [46].

Reduced Scan Times: Motion artifacts could also be minimized by reducing the scanning time so that physiologic motion is relatively frozen [47]. However, with the increased scanning speed, the Signal to Noise Ratio (SNR) also drops (which in turn affects the quality of CT images) [48]. There is a physical constraint on scanner speed as well.

Alignment of X-ray Source: Aligning the X-ray source with respect to physiologic motion is another way of minimizing motion artifacts. Mayo et al. [49] first observed that the appearance of double lung fissure structures was related to the direction of motion with respect to the initial direction of the X-ray beam. Crawford et al. [50] also demonstrated through computer simulation that the CT scanner is less sensitive to motion if the scan starts at angles that correspond to the largest component of the physiologic motion. In other words, if the scan starts at such a time that the midpoint of the scan coincides with the midpoint of the quiescent period in the motion, then the CT scanner is minimally sensitive to motion. The Crawford technique works well for reducing artifacts caused by respiratory motion, but artifacts caused by cardiac motion (which has a much shorter quiescent period) cannot be minimized with that alignment technique. This technique is not suitable for brain imaging systems.

Gating: Another well known prospective artifact reduction technique is physiologic gating, which uses the motionless period in physiologic motion as the time for acquiring projections. The CT images of a beating heart can be obtained by using gating at the end diastole. Moore et al. [51] used Electrocardiogram (ECG) data for precise gating at the peak of an R wave. Herman [52], Godwin *et al.*[53] and Oyama *et al.*[54] also used a similar approach, but they used ECG data to decide which projections from the already acquired projections to use during reconstruction. All gating techniques prolong imaging process time and increase X-ray radiation dose. Gating also suffers from misregistration, since the anatomy being imaged can never return to its initial position after each respiratory or cardiac cycle. Moreover, gating technique is not suitable for compensating for head motion artifacts.

1.3.2. Retrospective Techniques

The retrospective artifact reduction technique is a post-scanning process which works on the projection data and/or the reconstructed image that has already been corrupted [55]. There are two types of retrospective correction techniques. One operates on the reconstructed image and uses several filters or some weighting factors to remove artifacts from images. This technique is suitable for removing streaking artifacts, metal artifacts, and beam hardening artifacts. The other technique operates on motion corrupted projections and reconstructed images simultaneously. When motions occur during X-ray acquisition time, some inconsistencies will be created in the corresponding projections. These inconsistent projections can then be eliminated from the projection data set and missing projections can be interpolated from neighboring consistent projections [56].

Joseph *et al.* [57] used some projection interpolation to remove streak artifacts produced by high intensity objects such as bone. A similar approach proposed by Pelc N.J. *et al.* [58] removed artifacts produced by metal clips. Although projection interpolation methods work well to remove streaking artifacts, the downside is that they cause blurring in the reconstructed image. An innovative approach to reduce streaking artifacts without causing blurring is discussed in [59]. Other retrospective methods include the half scan and underscan [58]. In the half scanning method, artifacts are minimized by reducing scan times and allowing selective projections for reconstruction. Shorter scan times reduce the probability of motion occurring during scan time. If motion occurs near the beginning or the end of the scan, half scanning can be used to reconstruct the image using only those selective projections that are not affected by motions. Since half scanning has a lower SNR than the full scanning method, it is only used if reduced SNR is acceptable for fewer motion artifacts. In underscanning, each projection is multiplied by some weighting factor to eliminate inconsistencies between projections. The weighting factor linearly increases from zero to one for the first several projections and decreases from one to zero for the last several projections. To make up those projections that are multiplied by less than one, projections near the midpoint of the scan are multiplied by a factor that increases from one to two and then decreases from two to one. Underscanning works well for reducing streaking artifacts originating from small motion, but it cannot mitigate other motion artifacts such as blurring, doubling, and loss of resolution.

Up to this point, a brief review about retrospective methods that either modify the projection data set and use standard back projection or modify the final image to minimize the artifacts has been presented. In the following section, another retrospective

method called corrective reconstruction is discussed. Corrective reconstruction operates on filtered-backprojection in order to correct in-plane motion.

Corrective Reconstruction: Several corrective reconstruction methods based on known motion parameters have been reported in the literature. Yang *et al.*[60] divided the rigid body motions into translational and rotational components and demonstrated a computer simulation to correct these motions in parallel-beam CT systems. Translational motions were corrected by shifting the pixels during the back projection in the opposite direction of actual motion. Rotational motions were corrected by first detecting which projections were missing or duplicated because of rotation and then considering these projections as missing projections. The projection interpolation method was used to replace the missing projections. Yang *et al.*[60] validated these claims via computer simulation. However, since Yang *et al.*[60] used interpolation, the proposed method would cause blurring in the CT images. Crawford *et al.* [61] proposed a motion model based on a corrective back-projection algorithm called CTX. In CTX, the model was used to alter the position of each pixel during the reconstruction process so that the effects of motion were minimized. This model-based technique works only if the object motions are matched with the model. The Crawford method produced reasonably good respiratory motion correction under certain conditions. That said, in cases with cardiac motion artifacts, this method did not produce the expected results. Ritchie et al.[62] employed a pixel specific back-projection algorithm to reduce the streaking and doubling artifacts. The Ritchie technique has been successfully applied to conventional CT but it is not suitable for cone-beam 3D CT systems. Korin *et al.* [63] proposed a different corrective method whereby the in-plane motion was first measured during data

acquisition time and then this motion information was used to perform corrections on localized bases so that individual sections of the images were optimally corrected. Bergin *et al.* [64] and Noll *et al.* [65] also proposed similar techniques that removed blurring from the MRI images. Although these MRI approaches cannot be adopted directly into the CT system, measuring the motion parameters instead of relying on motion models and performing localized correction concepts could be applied to CT. Some of the recent developments in motion detection and motion-artifacts compensation in 3D CT systems are reviewed below.

Over the past few years, several methods have been reported to detect and correct motion artifacts using external sensors. Goldstein et al. [66] proposed a device that used a triad of three incandescent lights affixed on the patient's head while viewed by two position sensitive detectors. Fulton et al. [67] and Beache et al. [68] also proposed similar approaches that used infrared reflectors and a mechanical motion tracker comprising a base (which housed the electronics and a multiple-jointed lightweight arm). On the other hand, several other approaches (based solely on Sinogram/Linogram information, such as a motion correction method based on a cross-correlation of summed horizontal and vertical Sinograms of successive projection) [69-71] have been proposed and evaluated in the literature. It must be noted that motion detection using external sensors could cause systematic biases in the reconstructed images [72] and Sinogram/Linogram approaches suffer from the common disadvantage of dependence on resolution, sampling, noise characteristics, as well as the activity distribution of the scanned data set [66]. Moreover, the Sinogram approach often fails to detect motion in cases of abrupt and large head motions.

A very limited number of marker-based motion detection techniques have been reported in the literature, most of which are used in MRI systems that employ active markers and external sensors to find head motion [73-74]. D. Schafer *et al.* [75] first proposed a marker-based head motion field estimation system. Schafer *et al.* used some sinusoidal curve fitting functions in the Sinogram space to guess the initial 3D position of markers. Obviously, the Schafer technique suffers from the common disadvantage of depending upon the image quality of a projection data set. There are several other marker-based techniques that use radioactive markers implanted inside the patient, as well as on external skin surface in order to find tumor movement or respiratory movement [76], [77]. These techniques are not suitable for head motion measurement.

1.4 Research Goal

The goal of this research was to develop a system to detect motion and mitigate motion artifacts in a 3D circular cone-beam brain imaging system without using any external motion tracking sensors. This research objective was fulfilled through implementing the following four parts.

First, a computer simulation platform was created to emulate any desired practical head motion artifacts on the 3D Shepp-Logan phantom. The Open Source Cone-Beam Reconstruction (OSCaR-02) [78] implementation steps are used for efficient FDK based 3D reconstruction.

Second, a correlation-based approach was designed to detect and mitigate motion artifacts. This technique produced desired results under certain condition.

Third, a Marker-Based Motion Detector (MBMD) system was designed to detect six degrees of freedom of head motions. Using four markers and a numerical optimization technique, the proposed MBMD system estimated three rotational and three translational parameters of motion.

Fourth, a modified FDK algorithm, MBMD-FDK, was implemented to mitigate motion artifacts during the reconstruction process.

1.5 Organization of this Dissertation

The remainder of this dissertation is organized in the following sequence. Chapter 2 gives a review of the technical aspects of the 3D circular cone-beam CT system. However, in order to get a better understanding of the 3D CT system, this chapter also discusses the 2D parallel-beam and fan-beam CT systems. Chapter 3 gives an elaborate description of the projection equation of the 3D Shepp-Logan phantom. The chapter also discusses the implementation of the FDK algorithm on the 3D Shepp-Logan phantom. Chapter 4 includes a detailed derivation of the modified projection equation (which incorporates all possible forms of real-life head motion), a simulation of desired motion artifacts, and a simple technique for detecting and mitigating motion artifacts. Chapter 5 discusses the design and implementation of a proposed marker-based head motion measurement system. Chapter 6 gives a detailed simulation along, with quantitative and qualitative validations of motion detection and motion artifact mitigation approaches. Finally, a brief description of the challenges and future works (along with a conclusion) is presented in Chapter 7.

CHAPTER 2

A REVIEW OF THE TECHNICAL ASPECT OF 3D CONE-BEAM CT

2.1 Introduction

In three-dimensional (3D) circular Cone-beam CT systems, as shown in Fig. 2.1, the 3D object $f(x, y, z)$ is reconstructed from its projections $R_\beta(m, n)$ taken around the object. The source-detector pair rotates in a circular orbit about the z-axis by angle β, where β varies from 0 to 360^0 with a suitable step size w.r.t. Y-axis. At every step-angle, the source transmits a cone-beam of X-rays through the entire object while the detector plate on the opposite side of the object measures the intensity of the incident rays. The 3D reconstruction process is elaborately explained in section 2.4.

The Feldkamp-Davis-Kress (FDK) [17] algorithm is the most widely used algorithm for 3D Cone-beam reconstruction. Because of its simple one-dimensional filtration and parallel implementation, the FDK algorithm and its variations can be implemented efficiently [78]. The FDK algorithm is the extension of the two-dimensional (2D) fan-beam reconstruction algorithm and falls within the framework of the well-known filtered back projection (FBP). The fan-beam-based 2D reconstruction employs the basic principle of the classical parallel-beam reconstruction. In this chapter, the author first describes the 2D reconstruction using parallel-beam and fan-beam projections and

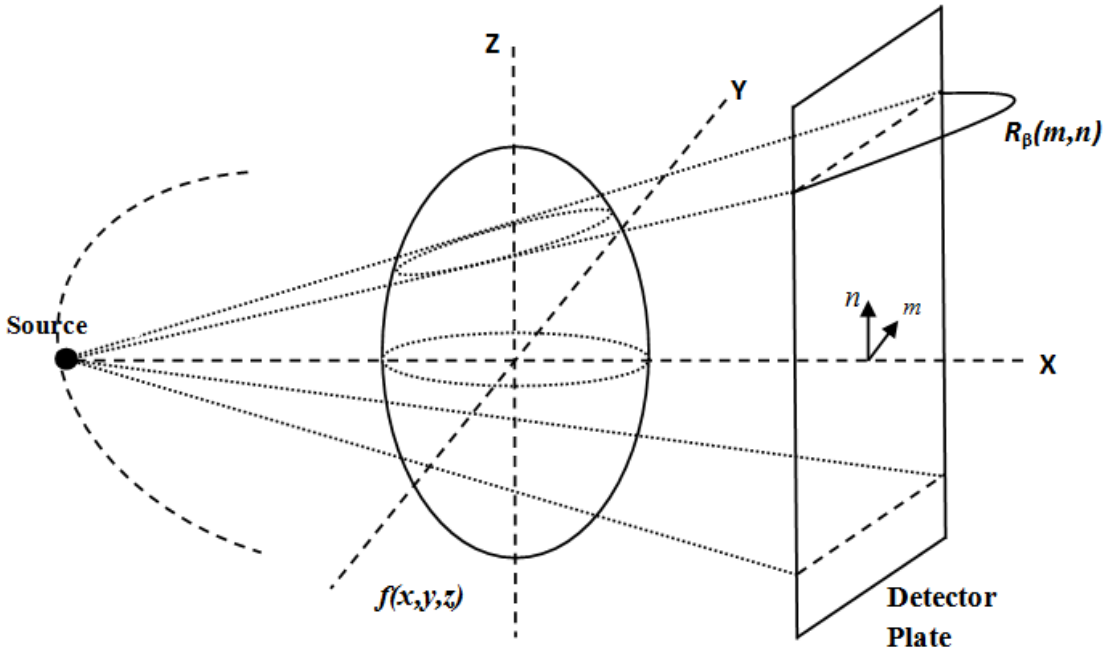

Figure 2.1 Circular Cone-beam CT System

then introduces the FDK algorithm. A more detailed description of the technical aspect of CT systems can be found in Kak *et al.*[80]

2.2 Two-Dimensional Reconstruction from Parallel-beam Projection:

In parallel-beam CT systems, an X-ray source transmits a pencil-beam of X-ray through an object while a detector on the opposite side of the object measures the intensity of the incident ray. When the ray passes through the object, its intensity is attenuated depending upon the matters with which it interacts. Therefore, the measurement on the detector plate indirectly gives the attenuation of the transmitted beam. Determining the attenuation of the X-ray beam is equivalent to computing an integral along a line of constant *t* (as shown in Fig. 2.2) through the plane that represents the cross-section of the object under investigation. After measuring the first line integral, the X-ray source and the detector pair are translated to a new position and the process is repeated until a set of line integrals (called parallel projection) for this particular θ position is acquired. After one projection is acquired, the source-detector pair is rotated to a new θ position and the process is repeated until θ has subtended 180^o.

Consider an object $f(x, y)$ (as shown in Fig 2.2) being modeled as a 2D distribution of the X-ray attenuation constant, with the line integral along the line L representing the total attenuation suffered by an X-ray line when it travels through the object in a straight line.

The equation of a line L (in normal form) is:

$$t = x \cos\theta + y \sin\theta, \quad -\infty < t < +\infty \tag{2.1}$$

where θ is the angle made with the positive x-axis and *t is* the distance from the origin in the *x-y* plane to the line L. For any given value of θ, a set of parallel rays is produced (as *t* varies).

Using Eq. (2.1), the line integral of $f(x,y)$ along the line L can be written as:

$$P_\theta(t) = \int_L f(x,y)ds, \tag{2.2}$$

where ds is the increment of length along L.

Eq. (2.2) can be rewritten using the Dirac delta function,

$$P_\theta(t) = \int_{-\infty}^{\infty}\int_{-\infty}^{\infty} f(x,y)\,\delta(x\cos\theta + y\sin\theta - t)dxdy \tag{2.3}$$

It can be shown that by using the Fourier Slice Theorem and Filtered Back Projection, the object $f(x,y)$, can be reconstructed from the projections $P_\theta(t)$, with θ varying from 0 to 180^0.

2.2.1. Fourier Slice Theorem

The Fourier transform of a parallel projection of an object, $f(x,y)$, taken at an angle of θ gives a slice of the two-dimensional transform of $f(x,y)$ [80].

The 2D Fourier transform of the object, $f(x,y)$ is :

$$F(u,v) = \int_{-\infty}^{\infty}\int_{-\infty}^{\infty} f(x,y)e^{-j2\pi(ux+vy)}dxdy \tag{2.4}$$

Likewise, the Fourier transform of a projection $P_\theta(t)$ at an angle of θ is given by :

$$S_\theta(w) = \int_{-\infty}^{\infty} P_\theta(t)e^{-j2\pi wt}dt \tag{2.5}$$

The simplest form of the Fourier Slice Theorem is given for a projection at $\theta = 0^0$. From Eq. (2.3) it can be written,

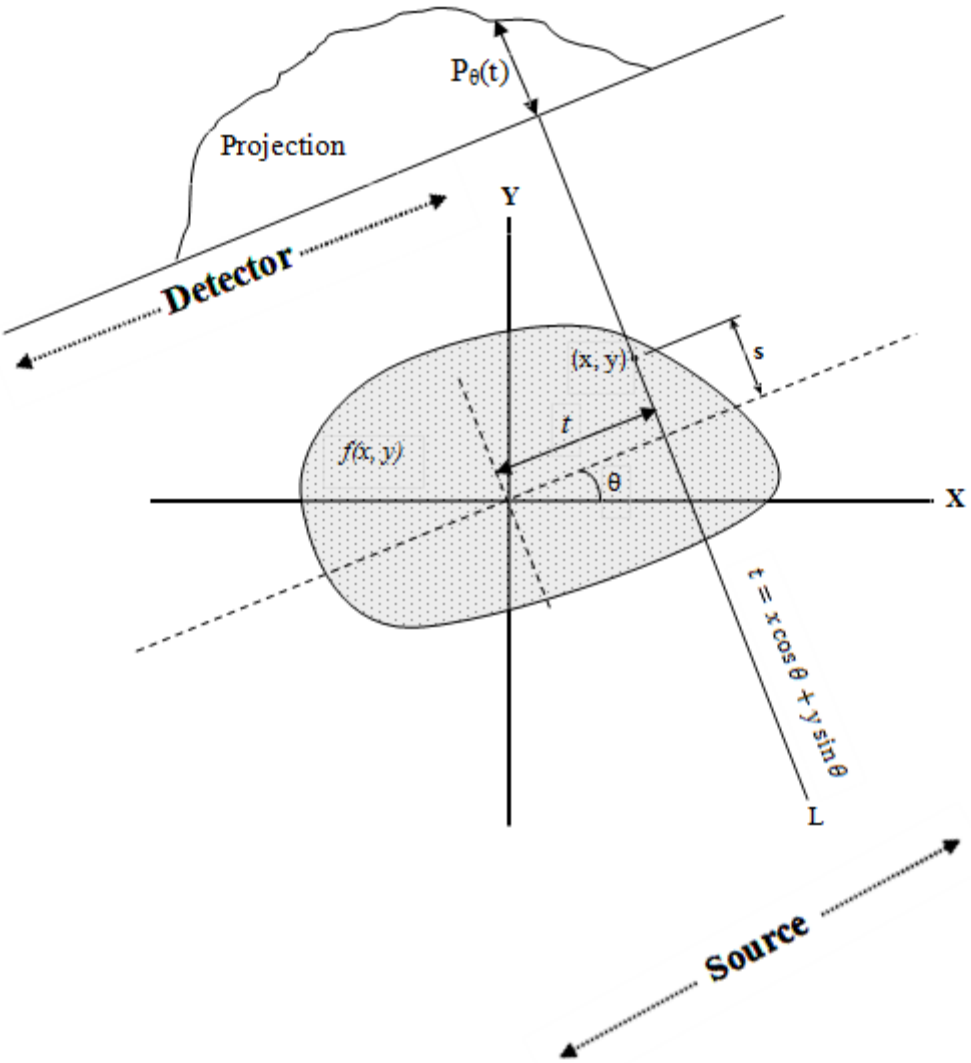

Figure 2.2 An Object *f(x, y)*, and its Projection, $P_\theta(t)$, are Shown For an Angle θ

$$P_0(t) = \iint_{-\infty}^{\infty} f(x,y)\delta(xcos0 + ysin0 - t)dxdy$$
$$= \int_{-\infty}^{\infty} f(t,y)dy$$

$$P_0(x) = \int_{-\infty}^{\infty} f(x,y)dy\Big|_{x=t} \tag{2.6}$$

Now considering $v = 0$ in Eq. (2.4), it can be written as

$$F(u,v)|_{v=0} = \int_{-\infty}^{\infty}\int_{-\infty}^{\infty} f(x,y)e^{-j2\pi ux}dxdy$$

$$= \int_{-\infty}^{\infty}\left[\int_{-\infty}^{\infty} f(x,y)dy\right]e^{-j2\pi ux}dx$$

$$= \int_{-\infty}^{\infty} P_0(x)\, e^{-j2\pi ux}dx$$

Therefore, from Eq. (2.5)

$$F(u,0) = S_0(u) \tag{2.7}$$

Eq. (2.7) is the simplest form of the Fourier Slice Theorem. The general form of the Fourier Slice Theorem can be derived by considering the following coordinate transformation.

$$\begin{bmatrix} t \\ s \end{bmatrix} = \begin{bmatrix} cos\theta & sin\theta \\ -sin\theta & cos\theta \end{bmatrix}\begin{bmatrix} x \\ y \end{bmatrix} \tag{2.8}$$

The (t,s) coordinate system is the rotated version of the original (x,y) coordinate system. In the (t,s) coordinate system, the line integral along the line of constant t is represented as,

$$P_\theta(t) = \int_{-\infty}^{\infty} f(t,s)ds \tag{2.9}$$

Taking 1-D Fourier transform of (2.9) along *t* gives the same Eq. as (2.5)

$$S_\theta(w) = \int_{-\infty}^{\infty} P_\theta(t) e^{-j2\pi wt} dt$$

Using Eq. (2.9), and finding the Jacobian from (2.8), Eqn. (2.5) can be written as,

$$S_\theta(w) = \int_{-\infty}^{\infty} \int_{-\infty}^{\infty} f(x,y) e^{-j2\pi w(x\cos\theta + y\sin\theta)} dx dy \tag{2.10}$$

So Eq. (2.4) can be rewritten as,

$$S_\theta(w) = F(u,v)\big|_{\substack{u = w\cos\theta \\ v = w\sin\theta}} \tag{2.11}$$

The above result indicates that the Fourier transform of each projection of $f(x,y)$ at angles θ_1, θ_2, ..., θ_k gives the values of $F(u,v)$ on radial lines [79]. If an infinite number of projections are taken, then $F(u,v)$ would be known at all points in the (u,v) domain. Thus, $f(x,y)$ can be reconstructed by taking the inverse Fourier transform of $F(u,v)$.

$$f(x,y) = \int_{-\infty}^{\infty} \int_{-\infty}^{\infty} F(u,v) e^{j2\pi(ux+vy)} du dv \tag{2.12}$$

In practice only a finite number of projections can be taken. In other words, $F(u,v)$ is only known along a finite number of radial lines. So, in order to use (2.12) for a successful reconstruction, one has to use some interpolation from these radial points of

$F(u,v)$. Filter Back Projection, discussed below, successfully reconstructs the object $f(x,y)$ from a finite number of projections.

2.2.2. Filtered Back Projection

From (2.11), (u,v) is known as,

$$u = wcos\theta$$
$$v = wsin\theta$$

Exchanging the rectangular coordinate system in the frequency domain, (u,v), for a polar coordinate system, (w,θ), by

$$dudv = J\ dwd\theta = \begin{vmatrix} \frac{\partial u}{\partial w} & \frac{\partial u}{\partial \theta} \\ \frac{\partial v}{\partial w} & \frac{\partial v}{\partial \theta} \end{vmatrix} dwd\theta = w\ dwd\theta \tag{2.13}$$

From (2.12) and (2.13), the inverse Fourier transform of a polar function can be written as,

$$\begin{aligned} f(x,y) &= \int_0^{2\pi}\int_0^{\infty} F(wcos\theta, wsin\theta)e^{j2\pi w(xcos\theta+ysin\theta)} w\ dwd\theta \\ &= \int_0^{\pi}\int_0^{\infty} S_\theta(w)e^{j2\pi w(xcos\theta+ysin\theta)} w\ dwd\theta \\ &+ \int_0^{\pi}\int_0^{\infty} S_{\theta+\pi}(w)e^{j2\pi w[x\cos(\theta+\pi)+y\sin(\theta+\pi)]} w\ dwd\theta \end{aligned} \tag{2.14}$$

Using the property $S_{\theta+\pi}(w) = S_\theta(-w)$, and Eq.(2.8), Eq.(2.14) can be written as,

$$\begin{aligned} f(x,y) &= \int_0^{\pi}\int_{-\infty}^{\infty} S_\theta(w)e^{j2\pi wt}|w|\ dwd\theta \\ &= \int_0^{\pi}\left[\int_{-\infty}^{\infty} S_\theta(w)e^{j2\pi wt}|w|\ dw\right] d\theta \end{aligned} \tag{2.15}$$

Let,

$$Q_\theta(t) = \int_{-\infty}^{\infty} S_\theta(w) e^{j2\pi wt} |w| \, dw \tag{2.16}$$

Thus, Eq. (2.15) can be written as,

$$f(x,y) = \int_0^\pi Q_\theta(x cos\theta + y sin\theta) d\theta \tag{2.17}$$

However, $Q_\theta(t)$ does not exist in its current form. For example, at t =0,

$$Q_\theta(0) = \int_{-\infty}^{\infty} S_\theta(w) |w| \, dw$$

If, $w \longrightarrow \infty$ then, $Q_\theta(0) \rightarrow \infty$

Therefore, (2.15) cannot be realized with the current limits. In practice, however, projections are band limited to a maximum frequency, W, above which any spectral energy in a projection is considered as negligible. By virtue of sampling theory, W will bound the sampling frequency w_s as,

$2W \leq w_s = \frac{1}{\Gamma}$, Γ is the sampling space (interval).

$$H(w) = \begin{cases} |w|, & if\ |w| < W \\ 0, & otherwise \end{cases} \tag{2.18}$$

So,

$$h(t) = \int_{-\infty}^{\infty} H(w) e^{j2\pi wt} dw = \int_{-\frac{1}{2\Gamma}}^{\frac{1}{2\Gamma}} |w| e^{j2\pi wt} dw \tag{2.19}$$

$$= \frac{1}{2\tau^2} \frac{sin2\pi t/2\Gamma}{2\pi t/2\Gamma} - \frac{1}{4\tau^2} \left(\frac{sin\pi t/2\Gamma}{\pi t/2\Gamma} \right)^2$$

Thus, (2.16) can be written as,

$$Q_\theta(t) = \int_{-\infty}^{\infty} S_\theta(w) H(w) e^{j2\pi wt} dw \tag{2.20}$$

Using the convolution theorem,

$$Q_\theta(t) = \int_{-\infty}^{\infty} P_\theta(t')h(t-t')dt' \tag{2.21}$$

Eq. (2.20) and (2.21) ensure that the 2D reconstruction of the object $f(x, y)$, can be achieved from the filtered projection using (2.17). In the following subsection, the parallel-beam reconstruction process is illustrated with the help of an example.

2.2.3. 2D Mathematical Phantom Reconstruction

In order to visualize the parallel-beam reconstruction process, a very well-known 2D Shepp-Logan phantom's reconstruction process is reviewed briefly in this subsection. Mathematical phantoms are widely used tools to verify the accuracy of any reconstruction algorithm in computerized tomography. The 2D Shepp-Logan phantom [81] (as shown in Fig 2.3) has become a de-facto standard in the field of medical imaging technology. The phantom consists of ten superimposed ellipses. Each ellipse has its own attenuation constant, ρ. The parameters of each of these ellipses are listed in Table 2.1. The projection value of any parallel ray through an ellipse, *E*, is the length of the line segment going through *E* multiplied by the attenuation constant of that ellipse. The projection of a ray going through an object comprised of ellipses is just the sum of the projections of each individual ellipse.

Suppose, the projection value of a ray at a distance t_l from the origin of the object under investigation is $P_\theta(t_l)$. The collection of line integrals $P_\theta(t_l)$ $l \in [0,1,2,\dots k]$ comprises a projection at a specific angle of θ. The collection of all

projections $\theta \in [0, \pi]$ constitutes a full set of projections required for a parallel-beam CT system.

Using the equation of the line, Eq. (2.1), and the general equation of an ellipse, the following projection equation of an ellipse centered at an origin can be derived easily.

$$P_\theta(t) = \begin{cases} 0 & for\ \ |t| > a(\theta) \\ \frac{2\rho AB\sqrt{a^2(\theta) - t^2}}{a^2(\theta)} & for\ |t| \le a(\theta) \end{cases} \tag{2.22}$$

where

$$a^2(\theta) = A^2 cos^2(\theta) + B^2 sin^2(\theta)$$

A, B, ρ are the parameters listed in Table 2.1

Each of the ellipses of Table 2.1 can be realized by the following simple rotation and translation operation.

$$\begin{bmatrix} X \\ Y \end{bmatrix} = \begin{bmatrix} \cos\varphi & -\cos\varphi \\ \sin\varphi & \sin\varphi \end{bmatrix} \begin{bmatrix} x - x_o \\ y - y_o \end{bmatrix} \tag{2.23}$$

where

φ, x_o, y_o are the rotation and translation listed in Table 2.1

Now, considering the ellipses described in Table 2.1, the general projection equation of the 2D Shepp-Logan phantom can be written as,

$$P_\theta(t) = P_{\theta - \varphi}(t - T\cos(\varrho - \theta)) \tag{2.24}$$

where

$$T = \sqrt{x_o^2 + y_o^2} \qquad \text{and} \quad \varrho = \tan^{-1}(x_o / y_o)$$

The parallel projections of the 2D Shepp-Logan phantom, as shown in Fig 2.4, can be calculated using Eq. (2.24) and linearity property of projection. For clarity, a single projection at a particular θ is also plotted in Fig. 2.5. After getting the required projections, the filtered back projection discussed in section 2.2.2 is applied to reconstruct the 2D Shepp-Logan phantom from its projection data set. A plot of the reconstructed image is shown in Fig. 2.6.

2.3 Two-dimensional Reconstruction from Fan-beam Projections

In order to reduce data acquisition time, a point source of radiation that emanates in a fan-shaped beam is introduced in 2D reconstructions [13]. A bank of detectors is used to simultaneously capture all X-ray beams in one fan. The sources and the entire bank of detectors are rotated to generate the desired number of fan projections. There are two types of fan-beam projections, depending upon whether the projections are sampled in equiangular or equispaced intervals. FDK based Cone-beam reconstruction employs the basic principles of equispaced fan-beam reconstruction. In this sub-section, the 2D reconstruction from the equispaced fan-beam projection is described briefly.

$R_\beta(s)$ denotes fan-beam projection, as shown in Fig. 2.7 [80], where s is the distance to the detector bank from the intersection of the center line of the projection to the detector line D_1D_2, and β is the source position w.r.t. y-axis. Although the projections are measured along D_1D_2, more efficient calculations assume an imaginary detector line, D_1' D_2' passing through the center of the rotation (axis). Thus in Fig. 2.8 a fan-projection $R_\beta(s)$ will be associated with the imaginary detector line D_1' D_2' [80].

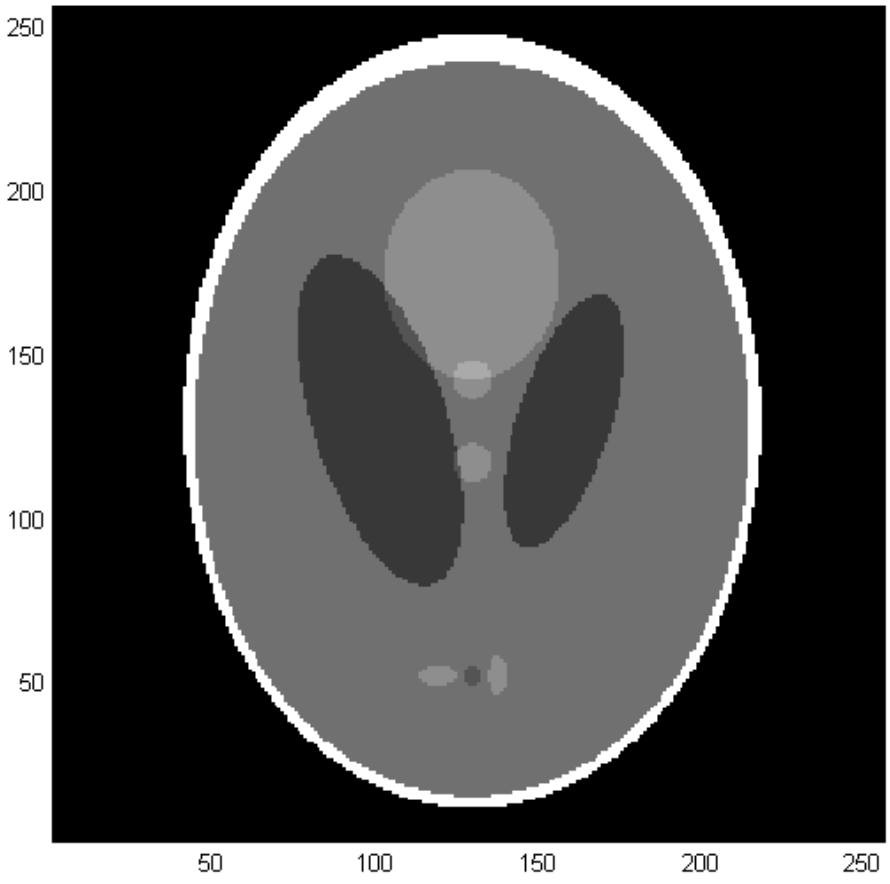

Figure 2.3 Two-dimensional Shepp-Logan Phantom

Table 2.1 Parameters of the 2D Shepp-Logan Phantom

Center coordinate (x_o, y_o)	Major axis (A)	Minor axis (B)	Rotation angle (φ^o)	Attenuation Constant (ρ)
(0, 0)	0.92	0.69	90	2.0
(0, -0.0184)	0.874	0.6624	90	-0.98
(0.22, 0)	0.31	0.11	72	-0.02
(0.22, 0)	0.41	0.16	108	0.01
(0, 0.35)	0.25	0.21	90	0.01
(0, 0.1)	0.046	0.046	0	0.01
(0, -0.1)	0.046	0.046	0	0.01
(-0.08, -0.605)	0.046	0.023	0	0.01
(0, -0.605)	0.023	0.023	0	0.01
(0.06, -0.605)	0.046	0.023	90	0.01

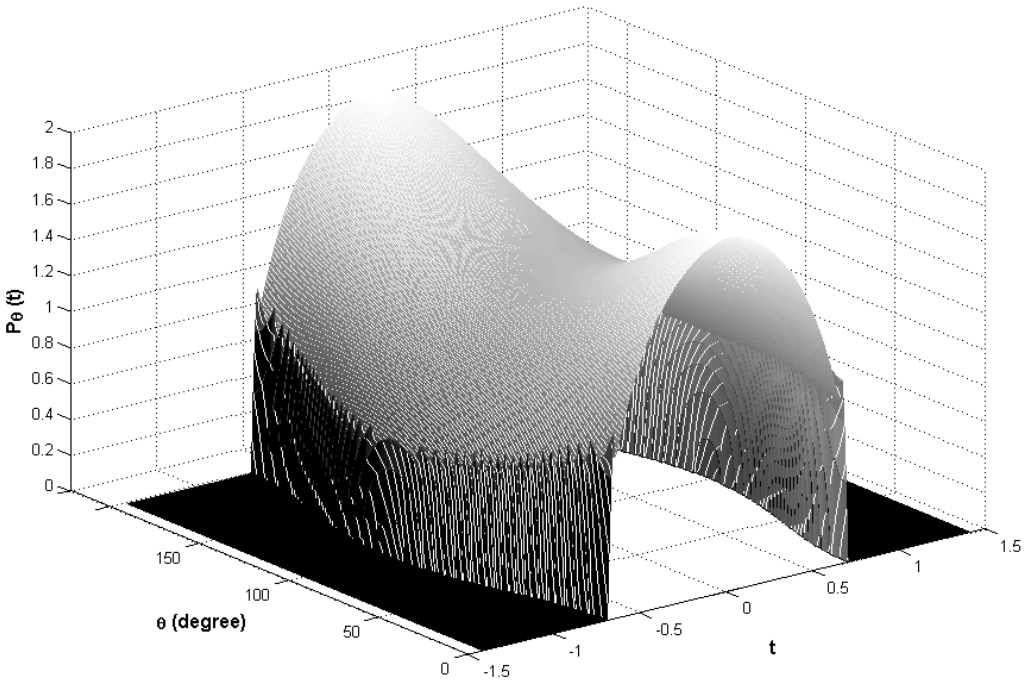

Figure 2.4 Set of Projections for the 2D Shepp-Logan Phantom

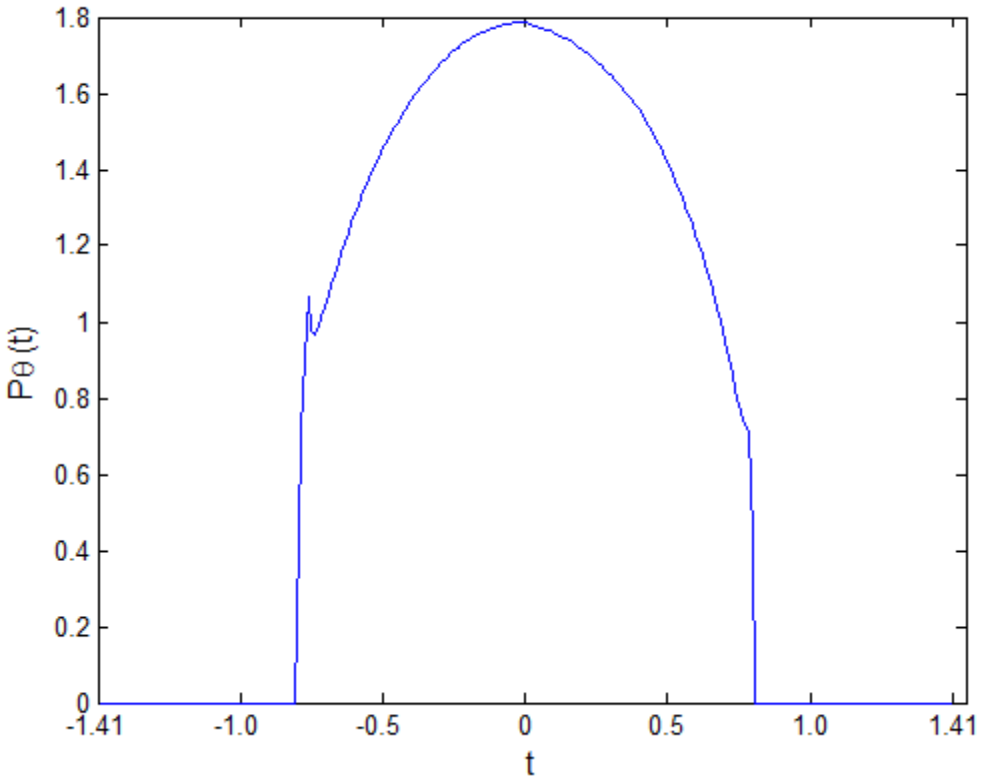

Figure 2.5 A Projection of the 2D Shepp-Logan Phantom Taken at θ =31^{o}

Figure 2.6 Reconstruction of the 2D Shepp-Logan Phantom Using FBP

If parallel projection data were generated for the object under consideration, then the ray *SA* would belong to a parallel projection $P_\theta(t)$, with θ and t as shown in Fig. 2.8. The relationships between fan-beam parameters (β, γ, s, D) and parallel projection parameters (θ, t) are given by,

$$t = s\cos\gamma \qquad \theta = \beta + \gamma$$
$$t = \frac{sD}{\sqrt{D^2+s^2}} \qquad \theta = \beta + \tan^{-1}\frac{s}{D} \tag{2.25}$$

Using parallel-projection Eq. of (2.5), (2.15) and (2.19), $f(x,y)$ can be reconstructed by

$$f(x,y) = \int_0^{\pi}\int_{-\infty}^{\infty} P_\theta(t)\, h(x\cos\theta + y\sin\theta - t)dtd\theta \tag{2.26}$$

That being said, fan-beam projections 180^o apart are not exactly equal. For a fan-beam projection, it is obvious to consider projections around 360^0 for successful reconstruction. So, Eq. (2.26) can be rewritten as

$$f(x,y) = \frac{1}{2}\int_0^{2\pi}\int_{-\infty}^{\infty} P_\theta(t)\, h(x\cos\theta + y\sin\theta - t)dtd\theta \tag{2.27}$$

The derivation of fan-beam projection becomes easier using polar coordinates (as shown in Fig. 2.9), where

$$x = r\cos\phi\,; \qquad y = r\sin\phi$$

Eq. (2.27) can now be rewritten as,

$$f(r,\phi) = \frac{1}{2}\int_0^{2\pi}\int_{-t_m}^{t_m} P_\theta(t)h(r\,cos(\theta+\phi)-t)dtd\theta \tag{2.28}$$

where, t_m is the value of t for which $P_\theta(t) = 0$ with $|t| > t_m$ in all projections.

Now, using the relationships of Eq. (2.25), Eq. (2.28) can be written as,

$$f(r,\phi) = \frac{1}{2}\int_{-\tan^{-1}(s_m/D)}^{2\pi-\tan^{-1}(s_m/D)}\int_{-s_m}^{s_m} P_{\beta+\gamma}\left(\frac{sD}{\sqrt{D^2+s^2}}\right) h\left(rcos\left(\beta+\tan^{-1}\frac{s}{D}-\phi\right)-\frac{Ds}{\sqrt{D^2+s^2}}\right)\frac{D^3}{(D^2+s^2)^{3/2}}dsd\beta \tag{2.29}$$

where, s_m is the largest value of s in each projection and corresponds to t_m for all parallel projection data. And,

$$dt\,d\theta = \frac{D^3}{(D^2+s^2)^{3/2}}ds\,d\beta \tag{2.30}$$

Now, observing the limits of β in Eq. (2.29) and considering the ray *SA* in fan-beam identity, Eq. (2.29) can be written as,

$$f(r,\phi) = \frac{1}{2}\int_0^{2\pi}\int_{-s_m}^{s_m} R_\beta(s)\,h\left(rcos\left(\beta+\tan^{-1}\frac{s}{D}-\phi\right)-\frac{Ds}{\sqrt{D^2+s^2}}\right)\frac{D^3}{(D^2+s^2)^{3/2}}dsd\beta \tag{2.31}$$

where,

$$R_\beta(s) = P_{\beta+\gamma}\left(\frac{sD}{\sqrt{D^2+s^2}}\right) \tag{2.32}$$

Using Fig. 2.8, the argument of h can be written as,

$$r\cos\left(\beta + \tan^{-1}\frac{s}{D} - \phi\right) - \frac{Ds}{\sqrt{D^2+s^2}} =$$

$$r\cos(\beta-\phi)\frac{D}{\sqrt{D^2+s^2}} - (D + r\sin(\beta-\phi))\frac{s}{\sqrt{D^2+s^2}} \tag{2.33}$$

After introducing two new variables (as shown in Fig. 2.9), *U* and *s'* for every pixel in the reconstruction plane, Eq. (2.33) can be written as,

$$r\cos\left(\beta + \tan^{-1}\frac{s}{D} - \phi\right) - \frac{Ds}{\sqrt{D^2+s^2}} = \frac{s'UD}{\sqrt{D^2+s^2}} - \frac{sUD}{\sqrt{D^2+s^2}} \tag{2.34}$$

where,

$$s' = \overline{SO}\frac{\overline{EP}}{\overline{SP}} = D\frac{r\cos(\beta-\phi)}{D+r\sin(\beta-\phi)} \tag{2.35}$$

$$U = \frac{\overline{SO}+\overline{OP}}{D} = \frac{D+r\sin(\beta-\phi)}{D} \tag{2.36}$$

(Variable *U* is the ratio of the distance *SP*, which is the projection of the source-to-pixel distance *SE* on the central line, to the source-to-center distance *D*)

Substituting (2.34) into (2.33), $f(r,\phi)$ can be reconstructed by

$$f(r,\phi) = \frac{1}{2}\int_0^{2\pi}\int_{-s_m}^{s_m} R_\beta(s)\, h\left((s'-s)\frac{UD}{\sqrt{D^2+s^2}}\right)\frac{D^3}{(D^2+s^2)^{3/2}}\,ds\,d\beta \tag{2.37}$$

Using Eq. (2.19), the kernel h can be written as

$$h\left((s'-s)\frac{UD}{\sqrt{D^2+s^2}}\right) = \int_{-\infty}^{\infty}|w|e^{j2\pi w(s'-s)(UD/\sqrt{D^2+s^2})}dw \tag{2.38}$$

Using a new variable

$$w' = w\frac{UD}{\sqrt{D^2+s^2}} \tag{2.39}$$

Eq. (2.38) can be written as

$$h\left((s'-s)\frac{UD}{\sqrt{D^2+s^2}}\right)=\frac{s^2+D^2}{U^2D^2}\int_{-\infty}^{\infty}|w'|e^{j2\pi w(s'-s)w'}dw' \tag{2.40}$$

Therefore

$$h\left((s'-s)\frac{UD}{\sqrt{D^2+s^2}}\right)=\frac{s^2+D^2}{U^2D^2}h(s'-s) \tag{2.41}$$

Now, substituting (2.41) into (2.37), $f(r,\phi)$ can be written as

$$f(r,\phi)=\int_0^{2\pi}\frac{1}{U^2}\int_{-\infty}^{\infty}R_\beta(s)\,g(s'-s)\frac{D}{\sqrt{D^2+s^2}}dsd\beta \tag{2.42}$$

where

$$g(s'-s)=\frac{1}{2}h(s'-s) \tag{2.43}$$

Eq. (2.42) can be simplified further as

$$f(r,\phi)=\int_0^{2\pi}\frac{1}{U^2}Q_\beta(s')d\beta \tag{2.44}$$

where

$$Q_\beta(s')=\int_{-\infty}^{\infty}R'_\beta(s)\,g(s'-s)ds \tag{2.45}$$

$$R'_\beta(s)=R_\beta(s)\frac{D}{\sqrt{D^2+s^2}} \tag{2.46}$$

Eq. (2.44) offers successful reconstruction of the object $f(r,\phi)$, from its fan-beam projections.

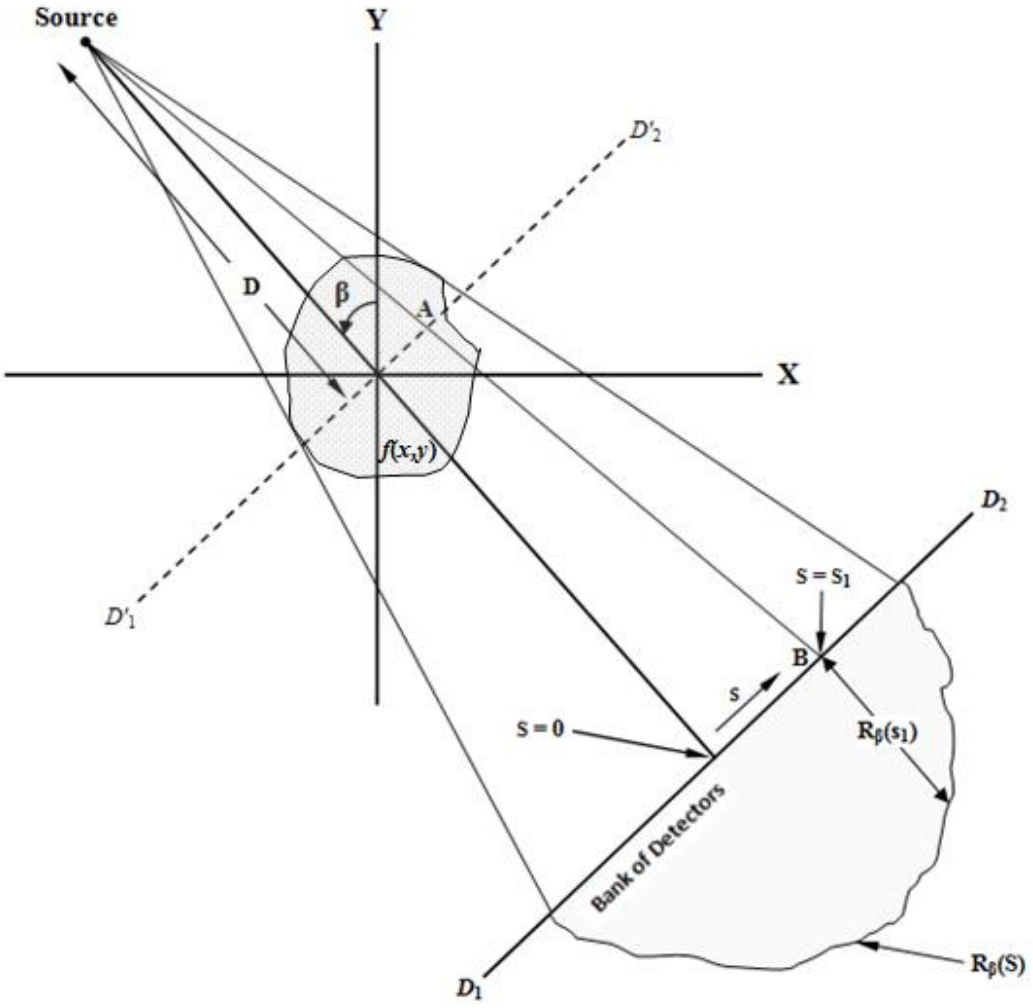

Figure 2.7 Equispaced Fan-beam Projection

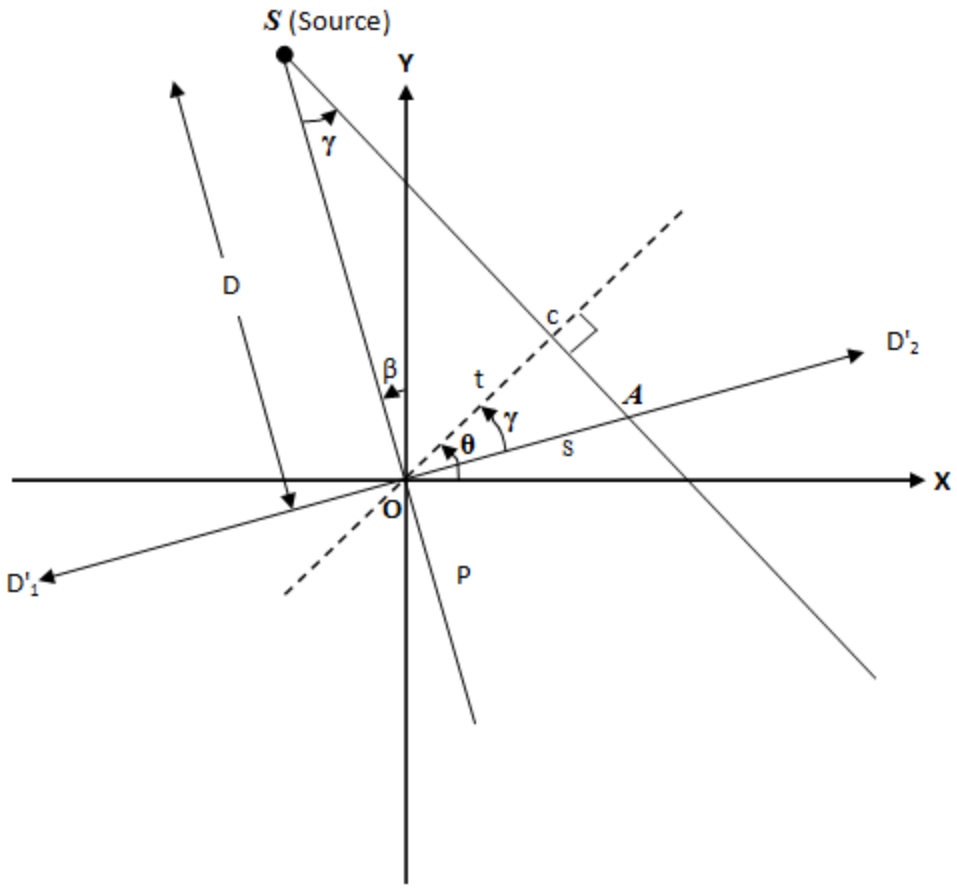

Figure 2.8 Equispaced Fan-beam Projection Showing Different Parameters

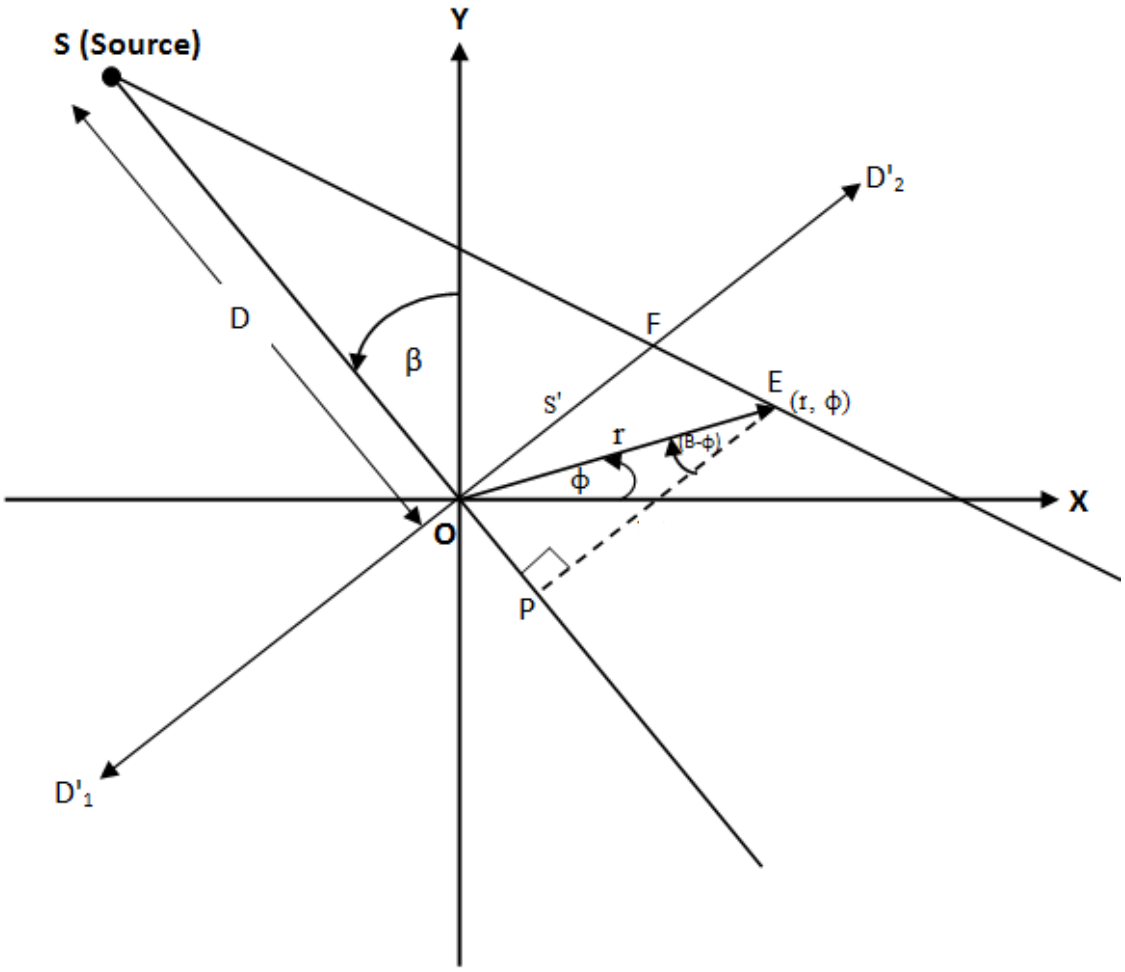

Figure 2.9 Equispaced Fan-beam Projection Showing Parameters For a Pixel at (r, ϕ).

(Variable U (not shown) is the ratio of the distance SP, which is the projection of the source-to-pixel distance SE on the central line, to the source-to-center distance)

2.4 FDK Based Three-dimensional Reconstruction From Cone-beam Projection

In cone-beam projection (unlike fan-beam projection, where a slice of the object is illuminated with a fan-beam of X-rays), the entire object is radiated with a point source and X-ray flux is measured on a detector plate, as shown in Fig. 2.1. The projection data $R_\beta(m,n)$ is now the function of source position β and horizontal and vertical positions m and n on the detector plane. In FDK-based reconstruction, each elevation in the cone-beam projection is considered as created from a tilted fan-beam projection and the final 3D reconstruction is achieved by summing the contribution to the object from all tilted fan-beams [80].

Therefore, the cone-beam reconstruction algorithm is derived by starting with the fan-beam reconstruction algorithm discussed in the previous section. In 3D cone-beam systems, each fan is angled out of the source-detector plane of rotation. In the derivation of the cone-beam algorithm, a change of variables is made to accomodate all angled out fan-beam projections.

Considering Eq. (2.42), (except for different names for some of the variables, as $p = s$, $p' = s'$), $f(r,\phi)$ can be written as

$$f(r,\phi) = \frac{1}{2}\int_0^{2\pi} \frac{1}{U^2} \int_{-\infty}^{\infty} R_\beta(p)\, h(p'-p)\, \frac{D}{\sqrt{D^2+p^2}}\, dp d\beta \tag{2.47}$$

where

$$p' = \frac{D\, r\, cos(\beta-\phi)}{D + r\sin(\beta-\phi)} \qquad \text{and} \qquad U = \frac{D + r\sin(\beta-\phi)}{D} \tag{2.48}$$

Replacing the (r, ϕ) coordinate system by the rotated coordinates $(\boldsymbol{t}, \boldsymbol{s})$. As shown in Fig. 2.10, $(\boldsymbol{t}, \boldsymbol{s})$ is the location of a points rotated by the angular displacement of the source-detector array.

Thus, using the coordinate transformation $(\boldsymbol{t}, \boldsymbol{s})$ can be written as

$$\boldsymbol{t} = x\,cos\beta + y\,sin\beta \qquad \boldsymbol{s} = -x\,sin\beta + y\,cos\beta \tag{2.49}$$

Now using Eq. (2.49) and $x = r\,cos\phi$, $y = r\,sin\phi$, Eq. (2.48) can be written as

$$p' = \frac{D\,\boldsymbol{t}}{D-\boldsymbol{s}} \quad \text{and} \quad U = \frac{D-\boldsymbol{s}}{D} \tag{2.50}$$

Thus, the fan-beam reconstruction of (2.47) can be written as

$$f(\boldsymbol{t}, \boldsymbol{s}) = \frac{1}{2}\int_0^{2\pi} \frac{D^2}{(D-\boldsymbol{s})^2} \int_{-\infty}^{\infty} R_\beta(p)\, h\left(\frac{D\,\boldsymbol{t}}{D-\boldsymbol{s}} - p\right) \frac{D}{\sqrt{D^2+p^2}}\, dp d\beta \tag{2.51}$$

In Fig. 2.10, a new coordinate system $(\widetilde{\boldsymbol{t}}, \widetilde{\boldsymbol{s}})$ is defined to represent the tilted fan-beam. Because of the tilted fan beam, the source distance D and angular differential β, change. The new source distance D', is given by:

$$D'^2 = D^2 + \zeta^2 \tag{2.52}$$

where ζ is the height of tilted fan beam above the center of the plane of rotation.

The change of angular rotation $d\beta'$ becomes,

$$D\,d\beta = D' d\beta' \tag{2.53}$$

Substituting these new variables (D' for D and $d\beta'$ for $d\beta$) and changing the notation of projections data as $R_{\beta'}(p,\zeta)$, (2.51) can be written as

$$f(\tilde{\boldsymbol{t}},\tilde{\boldsymbol{s}}) = \frac{1}{2}\int_0^{2\pi} \frac{D'^2}{(D'-\tilde{\boldsymbol{s}})^2} \int_{-\infty}^{\infty} R_{\beta'}(p,\zeta)\, h\left(\frac{D'\tilde{\boldsymbol{t}}}{D'-\tilde{\boldsymbol{s}}} - p\right) \frac{D'}{\sqrt{D'^2+p^2}}\, dp d\beta' \qquad (2.54)$$

The next step is to return to the original coordinate system of $(\boldsymbol{t},\boldsymbol{s},z)$**.** Note that in the tilted plane a point $(\tilde{s}_1,\tilde{t}_1)$ (as shown in Fig. 2.10), can be represented by a vector $\hat{\boldsymbol{r}}$**.** The relationship between the components of $\hat{\boldsymbol{r}}$ and the variables of $(\tilde{s}_1,\tilde{t}_1)$ are expressed as:

$$\tilde{t}_1 = \mathrm{r_t}\,, \qquad \frac{\tilde{s}_1}{D'} = \frac{\mathrm{r_s}}{D}\,, \qquad \frac{\zeta}{D} = \frac{\mathrm{r}_z}{(D-\mathrm{r}_{\boldsymbol{s}})}$$

From which the generalized coordinate transformation can be written as:

$$\tilde{\boldsymbol{t}} = \boldsymbol{t}, \qquad \frac{\tilde{\boldsymbol{s}}}{\boldsymbol{D'}} = \frac{\boldsymbol{s}}{\boldsymbol{D}}, \qquad \frac{\boldsymbol{\zeta}}{\boldsymbol{D}} = \frac{\boldsymbol{z}}{\boldsymbol{D-S}} \qquad (2.55)$$

Substituting (2.55), (2.53) and (2.52) in (2.54), $f(\boldsymbol{t},\boldsymbol{s})$ can be written as

$$f(\boldsymbol{t},\boldsymbol{s}) = \frac{1}{2}\int_0^{2\pi} \frac{D^2}{(D-\boldsymbol{s})^2} \int_{-\infty}^{\infty} R_{\beta}(p,\zeta)\, h\left(\frac{D\,\boldsymbol{t}}{D-\boldsymbol{s}} - p\right) \frac{D}{\sqrt{D^2+\zeta^2+p^2}}\, dp d\beta \qquad (2.56)$$

One important thing needing to be mentioned is that the cone-beam reconstruction algorithm of Eq. (2.56) is derived by considering an imaginary detector plane at the center of rotation inside the object. In other words, Eq. (2.56) uses the imaginary

projections created on the imaginary detector plate. In practice, the projections are created on the real detector plate placed behind the object, as shown in Fig 2.1. Therefore, for the purpose of practical implementation, the cone-beam reconstruction algorithm needs to be expressed in term of real projections. The following necessary modification can be applied to the cone-beam reconstruction algorithm of Eq. (2.56) to make it suitable for computer implementation.

Let the source to detector distance be *SDD* and source to center of rotation distance be *SAD***.** Using the similar triangle identity, the following necessary relationship is found:

$$p = \frac{m\,SAD}{SDD} \qquad\qquad \zeta = \frac{n\,SAD}{SDD} \tag{2.57}$$

Using (2.57), the cone-beam reconstruction of (2.56) can be broken into the following three simplified steps:

Step1: Find the weighted projections, $\tilde{R}_\beta(m,n)$

$$\tilde{R}_\beta(m,n) = \frac{SDD}{\sqrt{SDD^2+m^2+n^2}} R_\beta(m,n) \tag{2.58}$$

Step 2: Find the filtered projection using the following convolution:

$$Q_\beta(m,n) = \frac{1}{2}\tilde{R}_\beta(m,n) * h(m) \tag{2.59}$$

Step 3: Each filtered projection is back projected over the 3D grid, using:

$$f(\boldsymbol{t},\boldsymbol{s},z)=\int_0^{2\pi}\frac{SAD^2}{(SAD-\boldsymbol{s})^2}Q_\beta\left(\frac{SAD\,\boldsymbol{t}}{SAD-\boldsymbol{s}}\,,\,\frac{SAD\,Z}{SAD-\boldsymbol{s}}\right)d\beta \tag{2.60}$$

Eq. (2.58), (2.59), and (2.60) offer 3D reconstruction of any 3D object from its X-ray projections taken around circular orbit. In the following chapter, the above 3D reconstruction algorithm is applied successfully to a 3D Shepp-Logan Phantom.

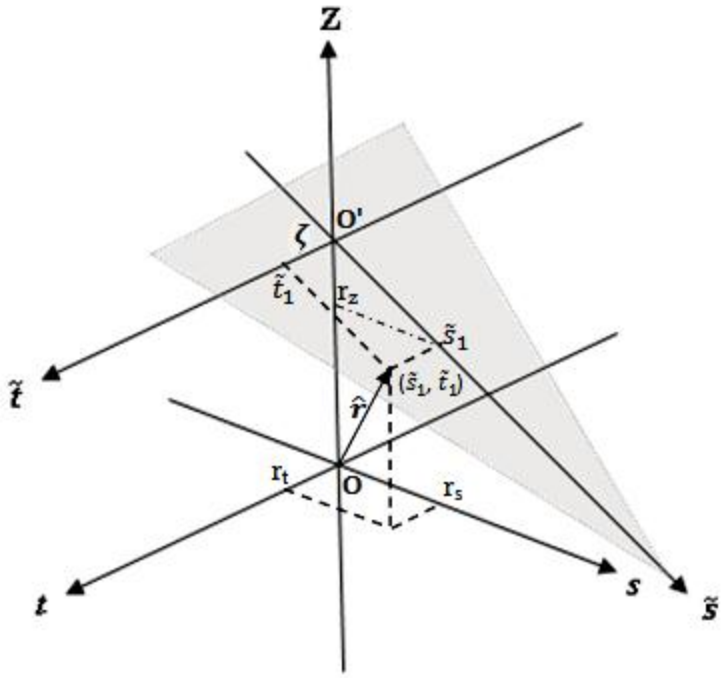

Figure 2.10 Vector $\hat{\boldsymbol{r}}$ in the $(\boldsymbol{t}, \boldsymbol{s}, z)$ Coordinate System Representing the Point $(\tilde{s}_1, \tilde{t}_1)$ in the Tilted Reconstruction Plane.

CHAPTER 3

IMPLEMENTATION OF THE FDK ALGORITHM ON A SYNTHETIC DATA SET

3.1 Introduction

This chapter discusses the implementation of the Feldkemp-Davis-Kress (FDK) based three-dimensional (3D) circular cone-beam reconstruction algorithm on a well known 3D Shepp-Logan mathematical phantom. A brief description of the 3D Shepp-Logan phantom and how closely the phantom can mimic the functionality of a human brain is given in the following section. In order to apply the 3D reconstruction algorithm on the 3D phantom, the X-ray projections $R_\beta(m,n)$ of the 3D phantom must be known. This chapter also discusses the derivation of the X-ray projection equation of the 3D Shepp-Logan phantom. The projection equation derived below is a more general form of equation compared to the well known Zhu *et al.*[82] equation. The proposed projection equation facilitates the creation of projections of one's own desired phantom. Finally, an elaborate description of the implementation steps to reconstruct the 3D Shepp-Logan phantom from its X-ray projections along with a computer simulation is presented.

3.2 Three-dimensional Shepp-Logan Phantom

The two-dimensional Shepp-Logan (2D) model was first proposed by L.A. Shepp and B.F. Logan in 1974 [81]. A 3D version of the Shepp-Logan phantom is now considered to be the typical simulation model used in the 3D-Computer Tomography (CT) imaging reconstruction field. In this dissertation, the 3D Shepp-Logan model of Fig. 3.1 is adopted for simulation purposes. Different slices (axial slices, coronal slices, and sagittal slices) of the 3D Shepp-Logan Phantom are plotted in Fig. 3.2. The model consists of ten superimposed ellipsoids with different attenuation coefficients (CT values). The unit of CT value is called Hu (Hounsfield unit), named after the inventor of the CT system, G.N. Hounsfield. The geometric locations, sizes and CT values of the ellipsoids used in the model are listed in Table 3.1. The CT value of water and air is 0 and -1000Hu respectively, while that of the bone varies from +100 to more than +1000Hu. The CT values of the ellipsoids are chosen in such a way so as to mimic soft tissue, bone and other matters (such as tumors) located in the head.

3.3 Computing Cone-beam X-ray Transform of The 3D Shepp-Logan Phantom

In circular cone-beam CT systems, the source-detector pair is rotated in a circular orbit about the z-axis by angle β, where β varies from 0^o to 360^o with a suitable step size w.r.t. the Y-axis. The ray integrals (projections), $R_\beta(m,n)$, are measured on the detector plate as shown in Figure 2.1. Cone-beam X-ray transform is a collection of ray integrals measured through every point (x,y,z) in an object. The X-ray projection $R_\beta(m,n)$ of the 3D Shepp-Logan Phantom is derived from the following set of equations.

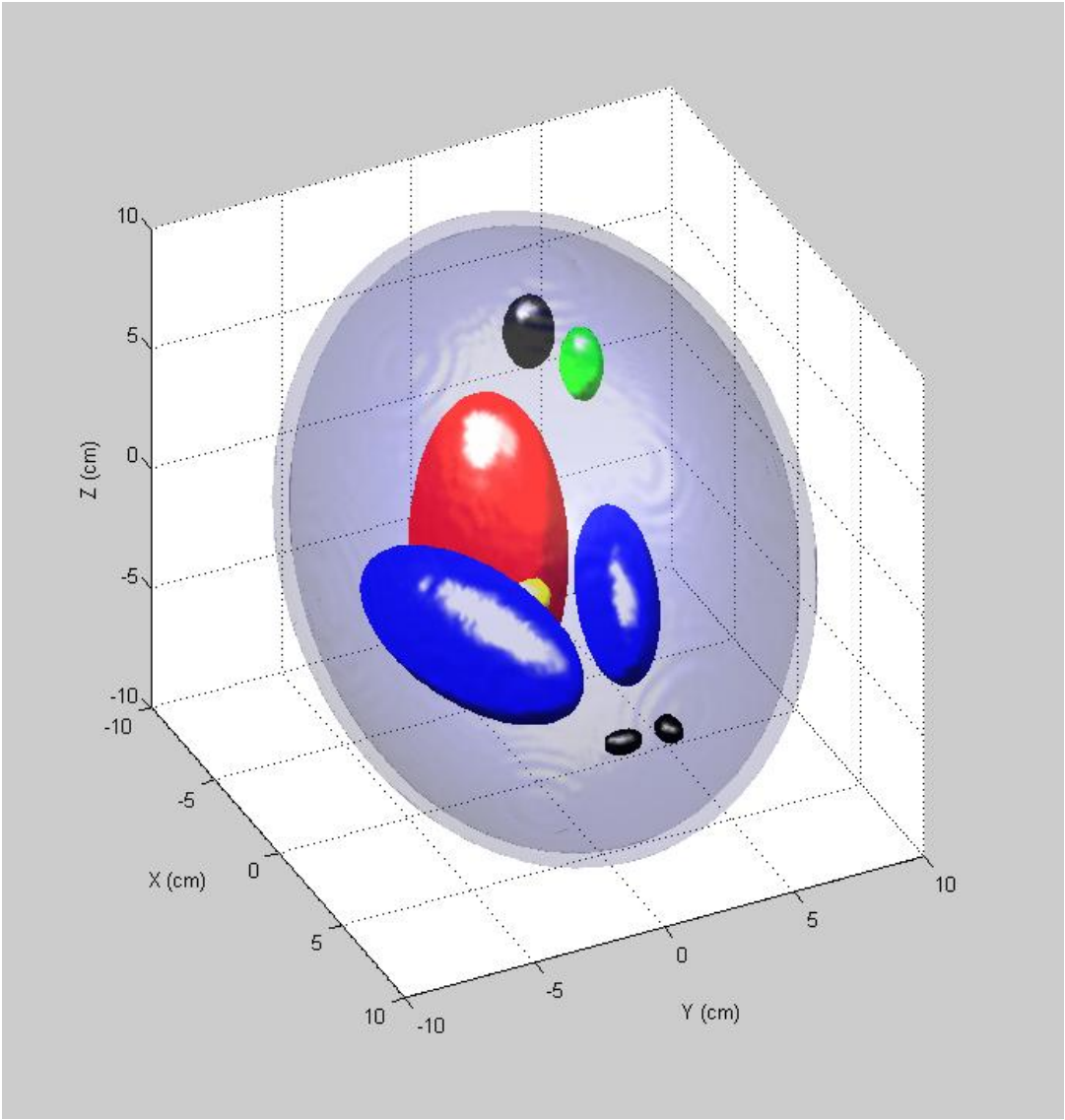

Figure 3.1 Three-dimensional Version of the Shepp-Logan Phantom.

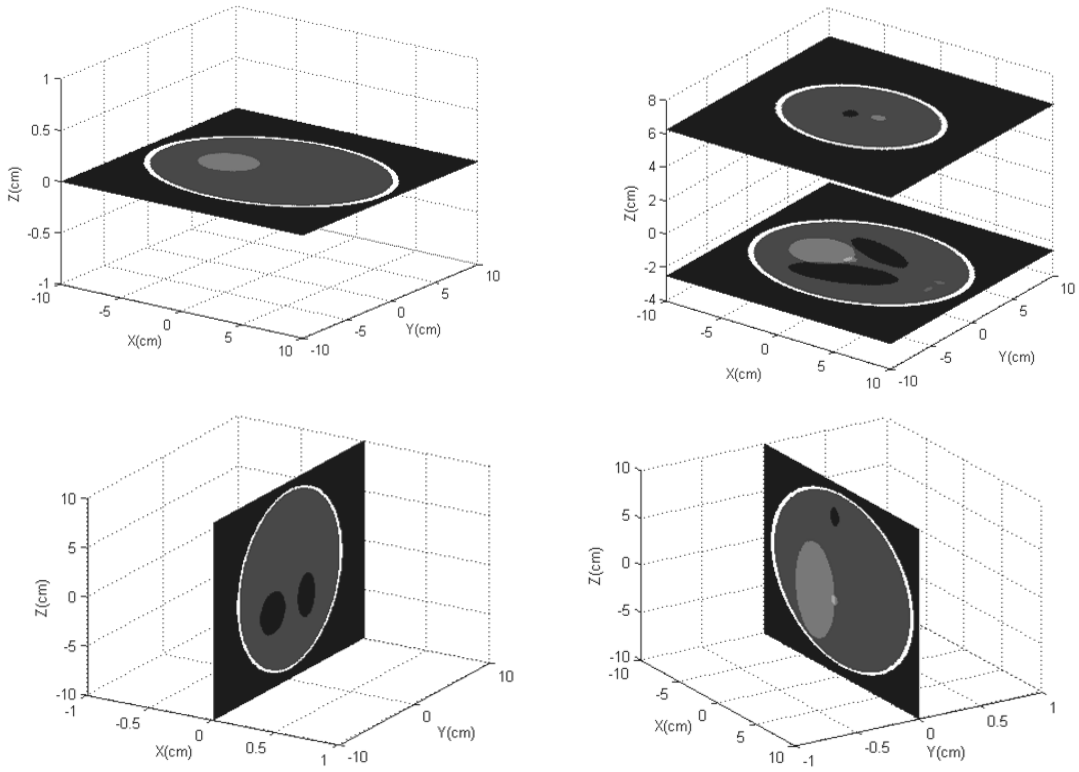

a *b*
c *d*

Figure 3.2 Different slices of the 3D Shepp-Logan Phantom.
(a) Axial Slice at z = 0cm (b) Axial slices at z = -2.5 cm and 6.25cm
(c) Coronal slice at x = 0cm (d) Sagittal slice at y = 0cm.

Table 3.1 Parameters of the 3D Shepp-Logan Phantom

Center Coordinate (cm)			Half axis (cm)			Rotation angle			CT Value
x_o	y_o	z_o	a	b	c	φ	ψ	ξ	ρ
0	0	0	6.90	9.20	9.00	0	0	0	1000
0	0	0	6.62	8.74	8.80	0	0	0	-800
-2.2	0	-2.5	4.10	1.60	2.10	108	0	0	-200
2.2	0	-2.5	3.10	1.10	2.20	72	0	0	-200
0	3.5	-2.5	2.10	2.50	5.00	0	0	0	100
0	1.0	-2.5	0.46	0.46	0.46	0	0	0	100
-0.8	-6.5	-2.5	0.46	0.23	0.20	0	0	0	100
0.6	-6.5	-2.5	0.46	0.23	0.20	90	0	0	100
0.6	-1.05	6.25	0.56	0.40	1.00	90	0	0	100
0	1.0	6.25	0.56	0.56	1.00	0	0	0	100

A ray in a 3D projection (As shown in Fig. 3.3) can be described by the intersection of two planes.

$$\mathbf{t} = x\cos\theta + y\sin\theta$$
$$\mathbf{r} = -(-x\sin\theta + y\cos\theta)\sin\lambda + z\cos\lambda \tag{3.1}$$

where

θ and λ are the two rotations in the (x, y, z) coordinate system.

t and **r** are the normals to the planes.

As shown in Fig. 3.4, the first rotation is by θ degrees about the z-axis to give $(\mathbf{t}, \boldsymbol{s}, z)$ axes, while the second rotation is done about the **t** axis out of the $(\mathbf{t}, \boldsymbol{s})$ plane by angle λ. In matrix form, thess rotations are given by:

$$\begin{bmatrix}\mathbf{t}\\ \tilde{\boldsymbol{s}}\\ \mathbf{r}\end{bmatrix} = \begin{bmatrix}1 & 0 & 0\\ 0 & \cos\lambda & \sin\lambda\\ 0 & -\sin\lambda & \cos\lambda\end{bmatrix}\begin{bmatrix}\cos\theta & \sin\theta & 0\\ -\sin\theta & \cos\theta & 0\\ 0 & 0 & 1\end{bmatrix}\begin{bmatrix}x\\ y\\ z\end{bmatrix} \tag{3.2}$$

Since the X-ray projections of the phantom are created on the detector of the cone-beam CT system, the projection equation must be dependent upon the geometric parameters of the cone-beam CT system. From Fig. 3.3, the following equivalent relationships between the cone beam variables $(p, \beta, \zeta, \gamma, m, n)$ and the ray variables $(\mathbf{t}, \mathbf{r}, \lambda, \theta)$ can be deduced:

$$p = \frac{m\,SAD}{SDD} \qquad \boldsymbol{\zeta} = \frac{n\,SAD}{SDD} \tag{3.3}$$

$$\mathbf{t} = p\cos\gamma = p\frac{SAD}{\sqrt{SAD^2+p^2}} \tag{3.4}$$

$$\theta = \beta + \gamma = \beta + \tan^{-1}(p/SAD) \tag{3.5}$$

$$\mathbf{r} = \boldsymbol{\zeta} \cos\lambda = \boldsymbol{\zeta} \frac{SAD}{\sqrt{SAD^2 + \boldsymbol{\zeta}^2}} \tag{3.6}$$

$$\lambda = \tan^{-1}(\boldsymbol{\zeta}/SAD) \tag{3.7}$$

where

SDD = Source to real detector distance

SAD = Source to imaginary detector distance

m, n denote the coordinate of the detector

The projection value of any ray through an ellipsoid, *E*, is the length of the line segment going through *E* multiplied by the CT number *(ρ)* of that ellipsoid [82]. According to the linearity property of projections (in other words, the linearity property of the Radon transform [83]), the projection value of any ray going through the 3D Shepp-Logan phanton, which consists of ten superimposed ellipsoids, is the summation of projection values of that ray through all the ellipsoids it interacts. Thus, to find a cone-beam X-ray projection of the 3D Shepp-Logan phantom, the projection values of all the rays in a cone beam have to be calculated.

As listed in Table 3.1, the description of an ellipsoid, *E*, can be obtained by rotations φ, ψ and ξ about the *z*, *y* and *x* axis and translations from the origin to the (x_o, y_o, z_o) position. In matrix form this transition is given by:

$$\begin{bmatrix} X \\ Y \\ Z \end{bmatrix} = \begin{bmatrix} R_{11} & R_{12} & R_{13} \\ R_{21} & R_{22} & R_{23} \\ R_{31} & R_{32} & R_{33} \end{bmatrix} \begin{bmatrix} x - x_o \\ y - y_o \\ z - z_0 \end{bmatrix} \tag{3.8}$$

where

$$R_{11} = \cos\psi\cos\varphi - \cos\xi\sin\varphi\sin\psi$$

$$R_{12} = \cos\psi\sin\varphi + \cos\xi\cos\varphi\sin\psi$$

$$R_{13} = \sin\psi\sin\xi$$

$$R_{21} = -\sin\psi\cos\varphi - \cos\xi\sin\varphi\cos\psi$$

$$R_{22} = -\sin\psi\sin\varphi + \cos\xi\cos\varphi\cos\psi$$

$$R_{23} = \cos\psi\sin\xi$$

$$R_{31} = \sin\xi\sin\varphi$$

$$R_{32} = -\sin\xi\cos\varphi$$

$$R_{33} = \cos\xi$$

Using Eqn. (3.8), the general equation of an ellipsoid could be written as:

$$\begin{aligned}(bc)^2\{(x-x_0)R_{11} + (y-y_0)R_{12} + (z-z_0)R_{13}\}^2 \\ + (ac)^2\{(x-x_0)R_{21} + (y-y_0)R_{22} + (z-z_0)R_{23}\}^2 \\ + (ab)^2\{(x-x_0)R_{31} + (y-y_0)R_{32} + (z-z_0)R_{33}\}^2 - (abc)^2 = 0\end{aligned} \tag{3.9}$$

The projection line of Eq. (3.1) could be written as the following parametric form of equations :

$$x = O_x + a_x\tau,\ y = O_y + a_y\tau,\ z = O_z + a_z\tau \tag{3.10}$$

where τ is the parameter.

$(O_x, O_y, O_z) = (0, t\ csc\ \theta\ , t\ cot\ \theta\ tan\ \theta + \boldsymbol{r}\ sec\ \lambda)$ is a point on the line, and

$(a_x, a_y, a_z) = (\sin\theta\cos\lambda\ , -\cos\theta\cos\lambda\ , -\sin\lambda)$ is the direction cosine vector.

Substituting Eq. (3.10) into Eq. (3.9) the following quadratic equation in terms of τ is found :

$$A\tau^2 + 2B\tau + C = 0, \tag{3.11}$$

where

$$A =$$

$$(bc)^2\left\{a_x^2R_{11}^2 + 2a_xa_yR_{11}R_{12} + a_y^2R_{12}^2 + a_z^2R_{13}^2 + 2a_ya_zR_{12}R_{13} + 2a_xa_zR_{11}R_{13}\right\} +$$

$$(ac)^2\left\{a_x^2R_{21}^2 + 2a_xa_yR_{21}R_{22} + a_y^2R_{22}^2 + a_z^2R_{23}^2 + 2a_ya_zR_{22}R_{23} + 2a_xa_zR_{21}R_{23}\right\} +$$

$$(ab)^2\left\{a_x^2R_{31}^2 + 2a_xa_yR_{31}R_{32} + a_y^2R_{32}^2 + a_z^2R_{33}^2 + 2a_ya_zR_{32}R_{33} + 2a_xa_zR_{31}R_{33}\right\}$$

$$B =$$

$$\begin{aligned}(bc)^2\{&-R_{11}^2a_xx_0 + R_{11}R_{12}\left(a_xO_y - a_xy_0 - x_0a_y\right) + R_{12}^2\left(O_ya_y - a_yy_0\right)\\ &+ R_{11}R_{13}(a_xO_z - a_xz_0 - a_zx_0) + R_{12}R_{13}\left(O_ya_z + a_yO_z - a_yz_0 - a_zy_0\right)\\ &+ R_{13}^2(O_za_z - a_zz_0)\} +\\ (ac)^2\{&-R_{21}^2a_xx_0 + R_{21}R_{22}\left(a_xO_y - a_xy_0 - x_0a_y\right) + R_{22}^2\left(O_ya_y - a_yy_0\right)\\ &+ R_{21}R_{23}(a_xO_z - a_xz_0 - a_zx_0) + R_{22}R_{23}\left(O_ya_z + a_yO_z - a_yz_0 - a_zy_0\right)\\ &+ R_{23}^2(O_za_z - a_zz_0)\} +\\ (ab)^2\{&-R_{31}^2a_xx_0 + R_{31}R_{32}\left(a_xO_y - a_xy_0 - x_0a_y\right) + R_{32}^2\left(O_ya_y - a_yy_0\right)\\ &+ R_{31}R_{33}(a_xO_z - a_xz_0 - a_zx_0) + R_{32}R_{33}\left(O_ya_z + a_yO_z - a_yz_0 - a_zy_0\right)\\ &+ R_{33}^2(O_za_z - a_zz_0)\}\end{aligned}$$

$$C =$$

$$(bc)^2\left\{R_{11}^2x_0^2 + 2R_{11}R_{12}(x_0y_0 - x_0O_y) + R_{12}^2(O_y - y_0)^2 + 2R_{11}R_{13}(x_0z_0 - x_0O_z)\right.$$

$$\left. + 2R_{12}R_{13}(O_y - y_0)(O_z - z_0) + R_{13}^2(O_z - z_0)^2\right\} +$$

$$(ac)^2\left\{R_{21}^2x_0^2 + 2R_{21}R_{22}(x_0y_0 - x_0O_y) + R_{22}^2(O_y - y_0)^2 + 2R_{21}R_{23}(x_0z_0 - x_0O_z)\right.$$

$$\left. + 2R_{22}R_{23}(O_y - y_0)(O_z - z_0) + R_{23}^2(O_z - z_0)^2\right\} +$$

$$(ab)^2\left\{R_{31}^2x_0^2 + 2R_{31}R_{32}(x_0y_0 - x_0O_y) + R_{32}^2(O_y - y_0)^2 + 2R_{31}R_{13}(x_0z_0 - x_0O_z)\right.$$

$$\left. + 2R_{32}R_{13}(O_y - y_0)(O_z - z_0) + R_{33}^2(O_z - z_0)^2\right\} - (abc)^2$$

The length of the line segment inside an ellipsoid is the absolute value of the difference of the two roots of this equation (3.11), if the roots exist. Note that *A>0*. Therefore, the projection value of the ray going through an ellipsoid is:

$$R = \begin{cases} 0 & if\ B^2 - AC \leq 0. \\ \frac{2\rho\sqrt{B^2 - AC}}{A} & if\ B^2 - AC > 0 \end{cases} \tag{3.12}$$

According to the linearity property of the radon transform, the projection value of the ray going through the 3D Shepp-Logan phantom consisting of ten superimposed ellipsoids is:

$$R_\beta(m,n) = \sum_{i=1}^{10} R_i$$

where i = 1,2,…….10.

β is the source detector position, and

m, n denote the position of the projection of the ray on the detector.

In order to find the projection value of a Cone-beam of rays going through the 3D Shepp-Logan phantom for a particular value of β, the projection values of all the rays going through the phantom have to be calculated. Using Eq. (3.3-3.7), (3.12), and the cone-beam parameters listed in table 3.2, X-ray projections of the 3D Shepp-Logan phantom are created for every rotation angle β of the step size 1^o. Some of these achieved projections are plotted in Fig. 3.5

3.4 3D Reconstruction Using FDK Algorithm

The FDK algorithm falls into the framework of the well-known Filtered Back Projection (FBP). In practice, the Cone-beam data acquired by the flat panel detector is first rescaled to find the weighted projection. After that, the weighted projections are row-wise filtered with a suitable reconstruction filter and followed by a 3D back projection for volume reconstruction. The necessary geometric parameters, listed in Table 3.2, are carefully chosen in order to keep the cone-beam angle within the acceptable range so that it will minimize the artifact due to a large cone-beam angle. In this dissertation, the OSCaR-02 [78] based implementation steps are adopted for efficient FDK-based 3D reconstruction.

Steps to implement FDK Algorithm:

(1) Input Projection data, $R_\beta(m, n)$

(2) Input *SDD, SAD* and desired reconstruction grid

(3) for all projection angles, β_k, Do

(4) $\tilde{R}_\beta(m,n) = R_\beta(m,n) \times \frac{SDD}{\sqrt{SDD^2+m^2+n^2}}$ % Rescalling stage

where, m, n = [-12.8:0.1:12.8];

(5) for all detector rows m Do

(6) $Q_\beta(m,n) = \tilde{R}_\beta(m,n) * h(m)$ % Filtering stage

where $h(m) = \int_{-W}^{W} |\omega| e^{j\omega m} d\omega$

(7) end for

(8) for all reconstruction voxels (x_p, y_q, z_r) Do

(9) $U \leftarrow SAD + x_p \sin\beta_k - y_q \cos\beta_k$ % Backprojection stage

(10) $p' = (SAD/U)(x_p \cos\beta_k + y_q \sin\beta_k)$

(11) $\zeta = (SAD/U) z_r$

(12) $f(x_p, y_q, z_r) = f(x_p, y_q, z_r) + (SAD^2/U^2) Q_\beta(p', \zeta)$

(13) end for

(14) end for

In the rescaling stage, only a simple multiplication of the projection with a weighting factor is necessary. The filtering operation could easily be done in the frequency domain, where the Fourier transformed weighted projection is multiplied by a ramp filter (as discussed in Eq. (2.18)) that has a maximum frequency of half the sampling frequency. In the back projection stage, the arguments of Q_β, (p', ζ), denote the intersection points of the projection lines on the imaginary detector plate for a particular β. In other words, the arguments represent 2D coordinates of the detector plate corresponding to every (x_p, y_q, z_r) of the reconstruction volume for a particular β. In

OSCaR-02 open source code, the Pinhole Camera Model technique described in [84] has been used to perform the 3D to 2D coordinate conversion effectively. The code also includes the linear indexing mechanism for finding the corresponding intensity values of all 3D mesh-grid points of the reconstruction volume using equivalent 2D mesh-grid points in the weighted and filtered projections matrix. The OSCaR-02 was developed for computing three-dimensional reconstruction from data gathered from cone-beam X-ray CT scanning geometries. In this research, the OSCaR-02 open source code has been modified to interface it with the synthetic data set. The modified OSCaR-02 code works perfectly on the 3D Shepp-Logan mathematical phantom. Several slices of the reconstructed 3D Shepp-Logan volume are shown in Figure 3.6.

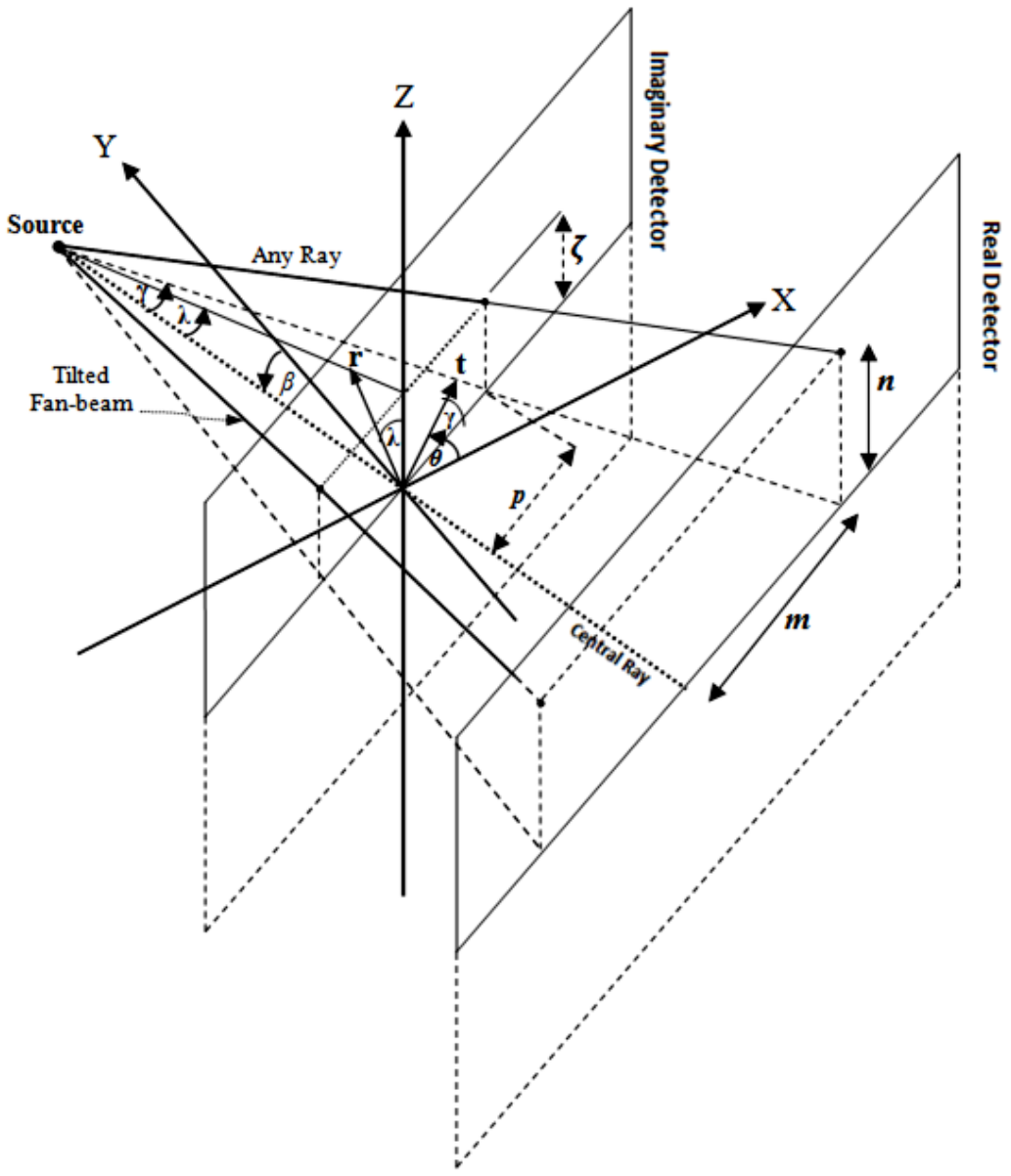

Figure 3.3 Cone-beam CT System Showing Different Parameters on Imaginary and Real Detector Plates.

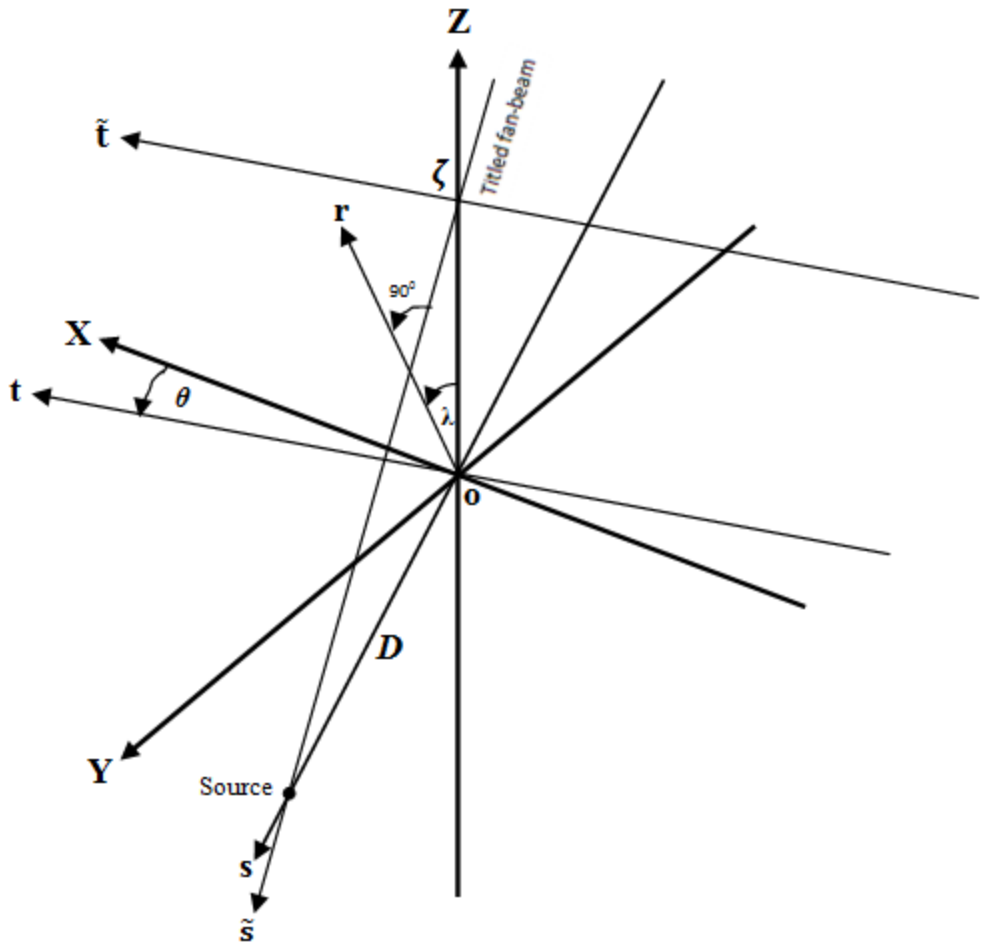

Figure 3.4 The Coordinate System of the Cone-beam CT System Showing (**t, r**) and (θ, λ) of any Ray.

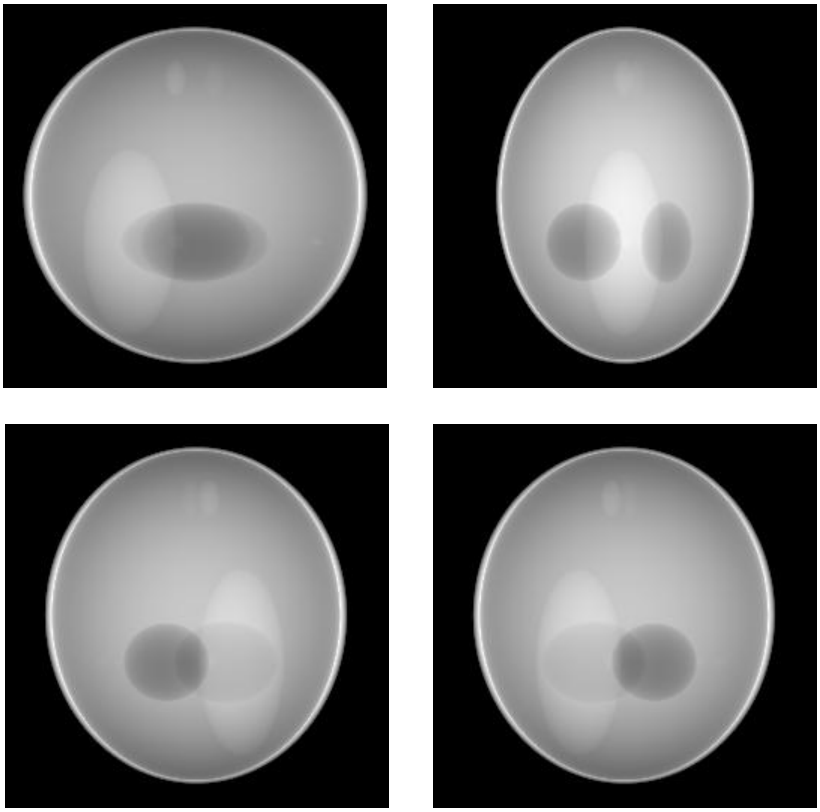

a b
c d

Figure 3.5 Projections at Different Source Positions.
(a-d) $\beta = 0^o, 90^o, 135^o, 315^o$.

Table 3.2 Geometric Parameters of Cone-beam CT System

Description of Parameters	Symbol	Values
Source to detector distance	*SDD*	2000 cm
Source to axis distance	*SAD*	1600 cm
Axis to detector distance	*ADD*	400 cm
No. of rows and column in detectror	N_{row}, N_{col}	256, 256
Pixel lenth in *m* direction	*dm*	0.1cm
Pixel length in *n* direction	*dn*	0.1cm
Reconstruction voxel volume	$0.08\times0.08\times0.08$ cm^3	

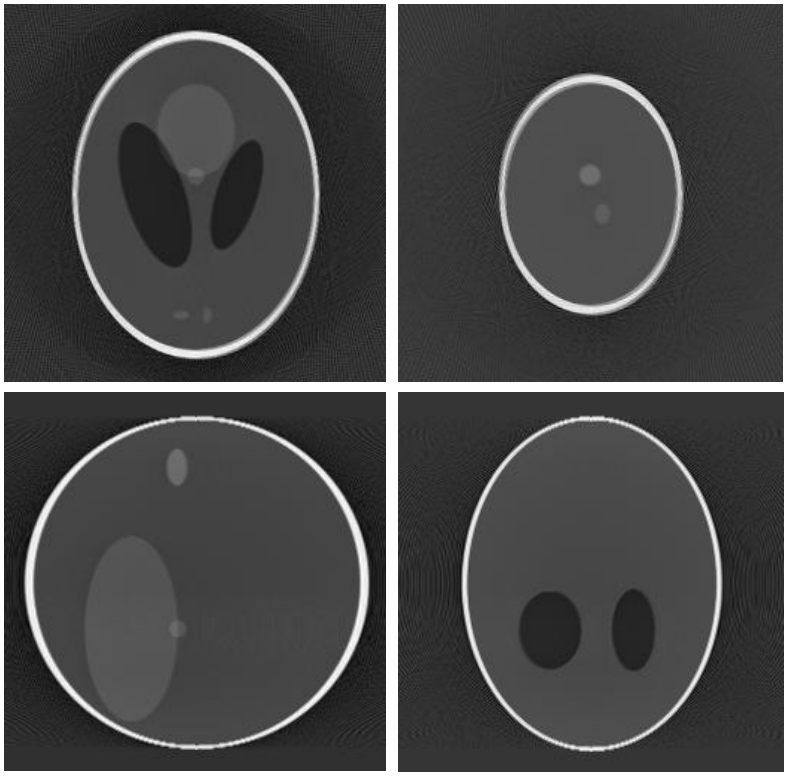

a b
c d

Figure 3.6 Slices of the Reconstructed Volume
(a) & (b) Axial Slices at z = -2.5cm and z = 6.5cm
(c) Sagittal slice (d) Coronal slice

CHAPTER 4

SIMULATING MOTION ARTIFACTS

4.1 Introduction

Head motion during brain computer tomography (CT) studies can degrade the reconstructed images through distortion, loss of resolution, and other artifacts (such as blurring and doubling). In order to simulate motion artifacts, the three-dimensional (3D) Shepp-Logan phantom has to be perturbed with six degrees of freedom of motion parameters to simulate any desired motion during X-ray data acquisition time. Therefore, the projection equation derived in the previous chapter has to be modified in such a way that it would incorporate the three rotational and three translational motion parameters. In this chapter, a detailed derivation of the modified projection equation of Ujjal *et al.*[86] is presented. Next, motion artifacts for three different types of motion are simulated. Then, a correlation-based technique is applied in order to detect the location of motion. A simple projection replacement technique is applied in order to mitigate motion artifacts.

4.2 Modified X-ray Projection of the 3D Shepp-Logan Phantom

According to the previous chapter, it is known that the description of an ellipsoid, (as listed in Table 3.1) can be obtained by rotations, φ, ψ and ξ about the *z, y* and *x* axis

and via translation from the origin to the (x_o, y_o, z_o) position. In matrix form, this transition is given by the following Eq (4.1).

$$\begin{bmatrix} X \\ Y \\ Z \end{bmatrix} = \begin{bmatrix} R_{11} & R_{12} & R_{13} \\ R_{21} & R_{22} & R_{23} \\ R_{31} & R_{32} & R_{33} \end{bmatrix} \begin{bmatrix} x - x_o \\ y - y_o \\ z - z_0 \end{bmatrix} \tag{4.1}$$

where

$$R_{11} = \cos\psi \cos\varphi - \cos\xi \sin\varphi \sin\psi$$

$$R_{12} = \cos\psi \sin\varphi + \cos\xi \cos\varphi \sin\psi$$

$$R_{13} = \sin\psi \sin\xi$$

$$R_{21} = -\sin\psi \cos\varphi - \cos\xi \sin\varphi \cos\psi$$

$$R_{22} = -\sin\psi \sin\varphi + \cos\xi \cos\varphi \cos\psi$$

$$R_{23} = \cos\psi \sin\xi$$

$$R_{31} = \sin\xi \sin\varphi$$

$$R_{32} = -\sin\xi \cos\varphi$$

$$R_{33} = \cos\xi$$

In order to simulate motion, however, the above Eq. (4.1) has to be modified to incorporate rotation and translation parameters of motion. This modification is given by the following Eq. (4.2):

$$\begin{bmatrix} X \\ Y \\ Z \end{bmatrix} = \begin{bmatrix} Q_{11} & Q_{12} & Q_{13} \\ Q_{21} & Q_{22} & Q_{23} \\ Q_{31} & Q_{32} & Q_{33} \end{bmatrix} \begin{bmatrix} x \\ y \\ z \end{bmatrix} - \begin{bmatrix} R_{11} & R_{12} & R_{13} \\ R_{21} & R_{22} & R_{23} \\ R_{31} & R_{32} & R_{33} \end{bmatrix} \begin{bmatrix} x_o + t_x \\ y_o + t_y \\ z_0 + t_z \end{bmatrix} \tag{4.2}$$

where

$$\begin{bmatrix} Q_{11} & Q_{12} & Q_{13} \\ Q_{21} & Q_{22} & Q_{23} \\ Q_{31} & Q_{32} & Q_{33} \end{bmatrix} = \begin{bmatrix} R_{11} & R_{12} & R_{13} \\ R_{21} & R_{22} & R_{23} \\ R_{31} & R_{32} & R_{33} \end{bmatrix} \times \begin{bmatrix} r_{11} & r_{12} & r_{13} \\ r_{21} & r_{22} & r_{23} \\ r_{31} & r_{32} & r_{33} \end{bmatrix} \quad (4.3)$$

where

$\begin{bmatrix} R_{11} & R_{12} & R_{13} \\ R_{21} & R_{22} & R_{23} \\ R_{31} & R_{32} & R_{33} \end{bmatrix}$ matrix is the rotation about the local origin of each individual ellipsoid in Table 4.1, And

$\begin{bmatrix} r_{11} & r_{12} & r_{13} \\ r_{21} & r_{22} & r_{23} \\ r_{31} & r_{32} & r_{33} \end{bmatrix}$ matrix is the rotation about the origin of the phantom,

where

$$r_{11} = \cos\alpha \cos\vartheta$$

$$r_{12} = \cos\alpha \sin\vartheta \sin\delta - \cos\delta \sin\alpha$$

$$r_{13} = \cos\alpha \sin\vartheta \cos\delta - \sin\alpha \sin\delta$$

$$r_{21} = \sin\alpha \cos\vartheta$$

$$r_{22} = \sin\alpha \sin\vartheta \sin\delta + \cos\alpha \cos\delta$$

$$r_{23} = \sin\alpha \sin\vartheta \cos\delta - \cos\alpha \sin\delta$$

$$r_{31} = -\sin\vartheta$$

$$r_{32} = \sin\delta \cos\vartheta$$

$$r_{33} = \cos\vartheta \cos\delta$$

where

$$\alpha - rotation\ about\ z\ (yaw)$$

$$\vartheta - rotation\ about\ y\ (pitch)$$

$$\delta - rotation\ about\ x\ (roll)$$

$$t_x, t_y, t_z \; are \; the \; translation \; about \; origin \tag{4.4}$$

Substituting Eq.(4.2) in the general equation of an ellipsoid, the following equation of (4.5) is found:

$$x^2 D_{xx} + y^2 D_{yy} + z^2 D_{zz} + 2xyD_{xy} + 2xzD_{xz} + 2yzD_{yz} -$$
$$2xD_x - 2yD_y - 2zD_z + K_c = 0 \tag{4.5}$$

where

$$D_{xx} = (bc)^2 Q_{11}^2 + (ac)^2 Q_{21}^2 + (ab)^2 Q_{31}^2$$

$$D_{yy} = (bc)^2 Q_{12}^2 + (ac)^2 Q_{22}^2 + (ab)^2 Q_{32}^2$$

$$D_{xx} = (bc)^2 Q_{13}^2 + (ac)^2 Q_{23}^2 + (ab)^2 Q_{33}^2$$

$$D_{xy} = (bc)^2 Q_{11} Q_{12} + (ac)^2 Q_{21} Q_{22} + (ab)^2 Q_{31} Q_{32}$$

$$D_{xz} = (bc)^2 Q_{11} Q_{13} + (ac)^2 Q_{21} Q_{23} + (ab)^2 Q_{31} Q_{33}$$

$$D_{yz} = (bc)^2 Q_{12} Q_{13} + (ac)^2 Q_{22} Q_{23} + (ab)^2 Q_{32} Q_{33}$$

$$D_x = (bc)^2 Q_{11} C_x + (ac)^2 Q_{21} C_y + (ab)^2 Q_{31} C_z$$

$$D_y = (bc)^2 Q_{12} C_x + (ac)^2 Q_{22} C_y + (ab)^2 Q_{32} C_z$$

$$D_x = (bc)^2 Q_{13} C_x + (ac)^2 Q_{23} C_y + (ab)^2 Q_{33} C_z$$

$$K_c = (bc)^2 C_x^2 + (ac)^2 C_y^2 + (ab)^2 C_z^2$$

where

$$C_x = R_{11}(x_o + t_x) + R_{12}(y_o + t_y) + R_{13}(z_0 + t_z)$$

$$C_y = R_{21}(x_o + t_x) + R_{22}(y_o + t_y) + R_{23}(z_0 + t_z)$$

$$C_z = R_{31}(x_o + t_x) + R_{32}(y_o + t_y) + R_{33}(z_0 + t_z)$$

The parametric form of projection equations from the previous chapter are rewritten below:

$$x = O_x + a_x\tau, \qquad y = O_y + a_y\tau, \qquad z = O_z + a_z\tau \tag{4.6}$$

where

τ is the parameter.

$(O_x, O_y, O_z) = (0, t\ csc\ \theta\ , t\ cot\ \theta\ tan\ \theta + \boldsymbol{r}\ sec\ \lambda)$ is a point on the line, and

$(a_x, a_y, a_z) = (\sin\theta\cos\lambda\ , -\cos\theta\cos\lambda\ , -\sin\lambda)$ is the direction cosine vector.

Substituting Eqn. (4.6) into Eq. (4.5), the following quadratic equation in terms of τ is found :

$$A\tau^2 + 2B\tau + C = 0, \tag{4.7}$$

where,

$$A = a_x^2 D_{xx} + a_y^2 D_{yy} + a_z^2 D_{zz} + 2a_x a_y D_{xy} + 2a_x a_z D_{xz} + 2a_y a_z D_{yz}$$

$$B = O_y a_y D_{yy} + O_z a_z D_{zz} + a_x O_y D_{xy} + a_x O_z D_{xz} +$$

$$(O_y a_z + a_y O_z) D_{yz} - a_x D_x - a_y D_y - a_z D_z$$

$$C = O_y^2 D_{yy} + O_z^2 D_{zz} + 2O_y O_z D_{yz} - 2O_y D_y - 2O_z D_z - K_c$$

As described in the previous chapter, Using Eqn. (3.3-3.7), (3.12) and the Cone-beam parameters listed Table 3.2, X-ray projections of the 3D Shepp-Logan phantom can be created for every rotation angle β of step size 1^o by the following Eq.

$$R_\beta(m,n) = \begin{cases} 0 & if\ B^2 - AC \le 0. \\ \frac{2\rho\sqrt{B^2 - AC}}{A} & if\ B^2 - AC > 0 \end{cases} \tag{4.8}$$

4.3 Simulating Motion Artifacts

Using six degrees of freedom of head motion (three translational (t_x, t_y, t_z) and three rotational (*roll, pitch, yaw*) parameters of Eq. (4.3) and Eq. (4.4) respectively), several gradual motions are simulated during the X-ray data acuisition process. Three different types of motions (translational, rotational, and rotational and translational combined) applied to the 3D Shepp-Logan phantom in three independent scans are listed in Tables 4.1, 4.2 and 4.3. Table 4.1 shows the translational motion of 0.2cm, 0.4cm and 0.8cm given to the phantom at different instances of the source detector positions during data acquisition time. Table 4.2 shows the values of the rotational motion parameters and the corresponding source detector positions of the applied motion. Table 4.3 shows the values of the combined rotational and translational motion parameters and the corresponding locations of the source detector position. Some images of motion-corrupted projections (as well as the axial, coronal and sagittal slices of the reconstructed volume of these motion-corrupted cases) are plotted in Figures 4.1, 4.2 and 4.3. From the slices of the reconstructed volume, it is clearly evident that head motion during X-ray data acquisition time creates conspicuous artifacts such as doubling, blurring, ghosting, and loss of resolution. In this dissertation it is assumed that the possible head motions that could occur during X-ray data acquisition time are: 1) Abrupt or large variation of motion, 2) A brief gradual variation of motion. In the following section a correlation based technique is proposed to detect and mitigate motion artifacts that occur because of large and abrupt variation of motion. In the following chapter a maker-based technique is proposed to mitigate motion artifacts that occur because of small and gradual variation of motion. At the time of simulation of motion, it has been assumed that the patient remains

Table 4.1 Translational Motion Given to the Phantom During Scanning of Projections at 200^o, 220^o, and 240^o

Step	*Roll*	*Pitch*	*Yaw*	t_x (cm)	t_y (cm)	t_z(cm)
200	0°	0°	0°	0.2	0	0
220	0°	0°	0°	0.2	0.4	0
240	0°	0°	0°	0.2	0.4	0.8

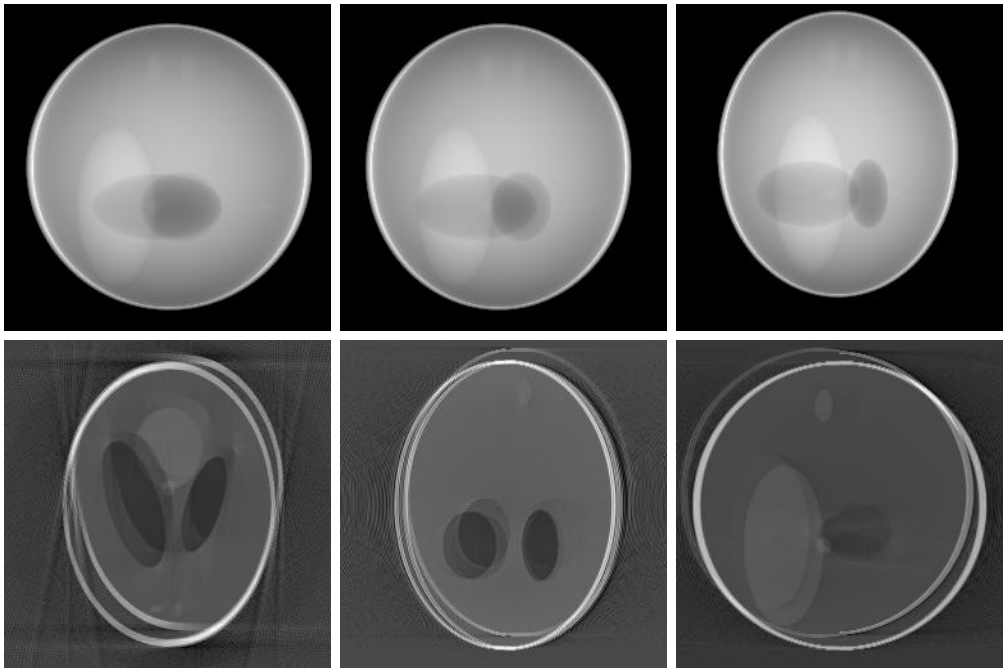

$a \quad b \quad c$
$d \quad e \quad f$ Figure 4.1 (a-c) Translation Motion Corrupted Projection at 200^o, 220^o and 240^o Source Position. (d-f) Axial, Coronal and Sagittal Slices of the Translational Motion-Corrupted Reconstructed Volume.

Table 4.2 Rotational Motion Given to the Phantom During Scanning of Projections at 260°, 270°, And 280°

Step	*Roll*	*Pitch*	*Yaw*	t_x (cm)	t_y (cm)	t_z(cm)
260	15°	0°	0°	0	0	0
270	15°	30°	0°	0	0	0
280	15°	30°	25°	0	0	0

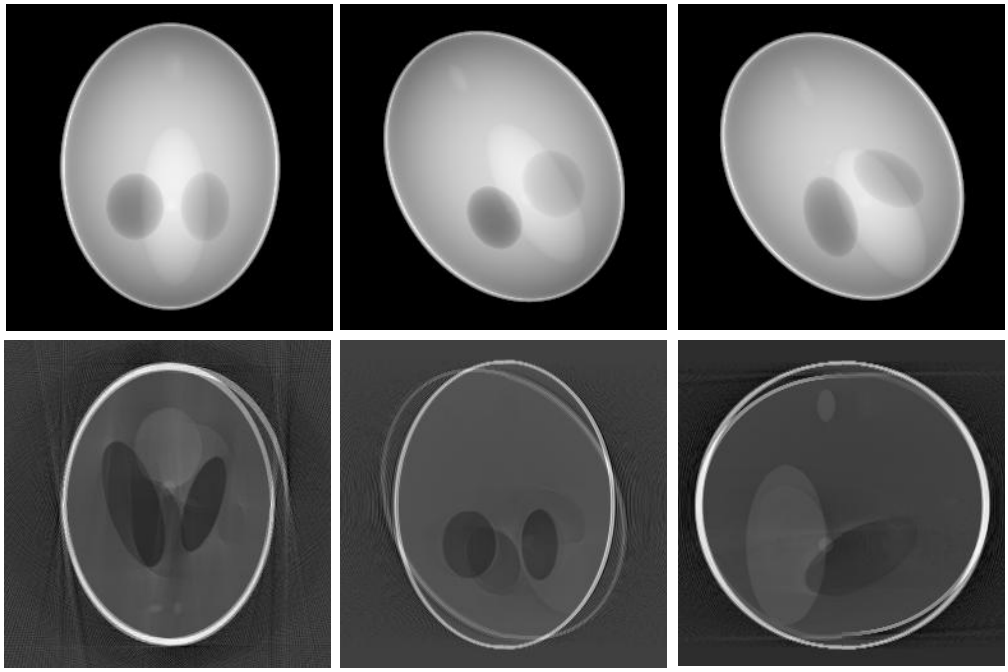

a b c
d e f Figure 4.2 (a-c) Rotational Motion Corrupted Projection at 260°, 270° and 280° Source Position. (d-f) Axial, Coronal And Sagittal Slices of The Rotational Motion Corrupted Reconstructed Volume.

Table 4.3 Combined Rotational and Translational Motion Given to the Phantom During Scanning of Projections at 160°, 180°, and 200°

Step	*Roll*	*Pitch*	*Yaw*	t_x (cm)	t_y (cm)	t_z(cm)
160	15°	0°	0°	1.0	0	0
180	15°	20°	0°	1.0	2.0	0
200	15°	20°	25°	1.0	2.0	1.5

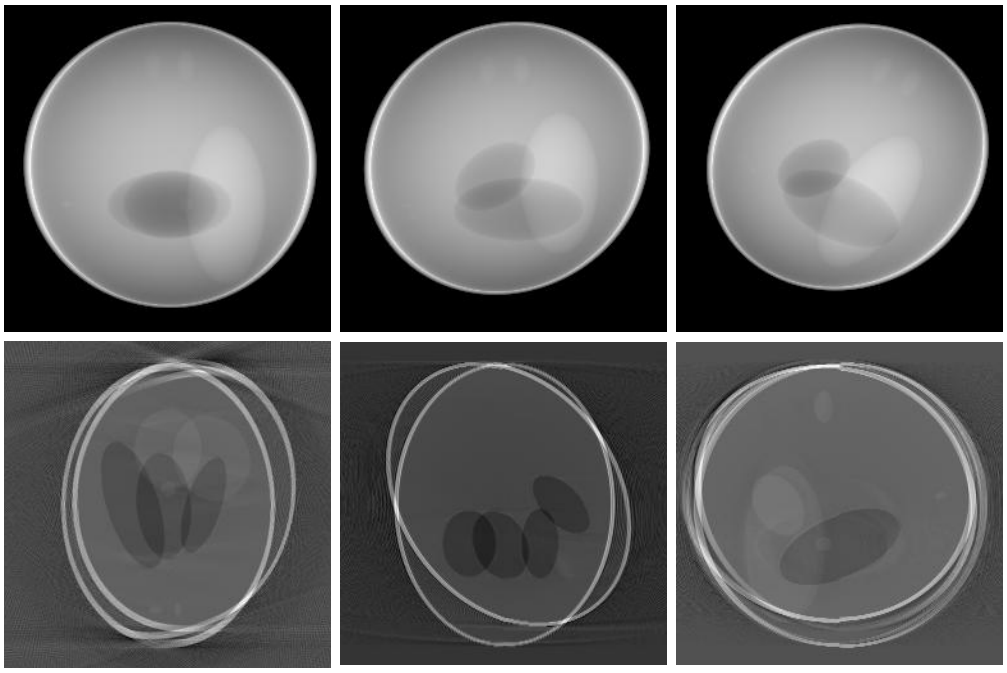

a b c
d e f Figure 4.3 (a-c) Combined Motion Corrupted Projection at 160°, 180° and 200° Source Position. (d-f) Axial, Coronal And Sagittal Slices of The Translational And Rotational Motion Corrupted Reconstructed Volume.

stationary during acquisition of individual projections and only moves between the projections. The above assumption imposes no restriction on the type and timing of the motions which can be corrected by the proposed motion compensation technique discussed in the next section. That said, a simple modification to the software would allow this assumption to be eliminated.

In this research, a Graphic Processor Unit (GPU) (NVDIA TESLA C2050) has been used to simulate X-ray projections of the 3D Shepp-Logan Phantom. Necessary code to create 360 X-ray projections of the Phantom are attached to the appendix. With a Dell T7500 machine, it takes only 63.29 seconds to create 360 X-ray projections of the Phantom.

4.4 A Simple Technique to Detect Motion and Mitigate Motion Artifacts

The idea behind this simple motion detection originated from the fact that the correlation-coefficients between adjacent projections, which are taken at a step size of 1^{o} apart, are very high. If the object under investigation suffers from any kind of motion, then the value of the correlation-coefficients of some of the adjacent projections will drop depending upon the amount and position of the motion. Using the following Equation (4.9), the correlation-coefficients for a motion free case, as well as translational, rotational and combined motion-corrupted cases are calculated. Figures (4.4), (4.5), (4.6), and (4.7) (the plots of correlation-coefficients (*Cc*) for these four different cases) validate the assumption given above.

$$Cc = \frac{\sum_m \sum_n (A_{mn} - \bar{A})\,(B_{mn} - \bar{B})}{\sqrt{[\sum_m \sum_n (A_{mn} - \bar{A})^2][\sum_m \sum_n (B_{mn} - \bar{B})^2]}} \tag{4.9}$$

where

m, n are the pixel positions.

$A_{mn} = R_{\beta}(m,n)$ and $B_{mn} = R_{\beta+1}(m,n)$

$\bar{A}$ and $\bar{B}$ are the mean of A_{mn} and $B_{mn,}$ respectively.

In Fig. 4.4 (the motion-free ideal case), it is clearly evident that the correlations between the adjacent projections are very high and almost close to unity. In Fig. 4.5, however (a translation motion-corrupted case), the correlations between the adjacent projections drop to the locations where motion-corruption occurred during data acquisition time. Similarly, in Figs. 4.6 and 4.7, it is clear how the correlation between adjacent projections drops to those pairs where motions occurred. It could also be observed that there is a direct relationship between the prevalence of motion artifacts and the amount of drop of correlation, as well as the duration of occurrence of motion. From Figs. 4.3 and 4.7, it can be observed that the predominance of motion artifacts is a direct consequence of the amount of the drop in correlations and the duration of occurrences of motions.

4.5 Steps to Mitigate Motion Artifacts

Correlation between adjacent projections indicates the location of the source detector pair β_m where motion occurs. Knowing the values of β_m, the following simple steps taken from Ujjal *et al.* [86] can be applied during the reconstruction process to mitigate motion artifacts (Test case: Rotational Motion)

1) Locate Motion-Corrupted Projections from the correlations between adjacent pairs as shown in Fig. 4.6 (Motion corruption occurs at $\beta = 260^o$, 270^o, and 280^o source-detector position)
2) Find the maximum number of consecutive projections that remain stable during the scanning process.
   (From $\beta = 1^o$ to 259^o projections remain stable and not affected by motion)
3) Find 180^o apart (counterpart) projections of the remaining projections
   (Remaining projections: $\beta = 260^o$ to 360^o, Counterpart: $\beta = 80^o$ to 180^o)
4) Flip left to right the information content of the counterpart projections
5) Replace remaining projections by their counterpart projections.
6) Apply the steps mentioned in section 3.4 to the aligned projections to reconstruct the 3D volume.

The same process can be applied to other motion-corrupted cases.

Fig. 4.8 shows the plots of axial, coronal and sagittal slices of the reconstructed volume of the rotational motion-corrupted case, motion compensated case and motion free case side by side. Fig. 4.9 shows the similar plots for the translational motion-corrupted case. It is quite obvious that greater numbers of consecutive stable projections will produce a better reconstruction. For the above two motion-corrupted cases, the translational motion-corrupted case has 200 consecutive stable projections, whereas the rotational motion-corrupted case has 260 consecutive stable projections. Although the quality of the motion-compensated slices look similar for both motion-corrupted cases, the differences in the quality of the reconstructed images can be observed in Fig. 4.10 and

Fig. 4.11. The one pixel-wide intensity profile of the reconstructed axial slices of the rotational and translational motion-corrupted cases are compared with that of the motion-free ideal case in Fig. 4.10 and Fig. 4.11. From these figures it can be observed that the above motion compensation technique resulted in a rotational motion compensated intensity profile close to that of the ideal case. Therefore, it can be inferred that the proposed technique produces better reconstruction and less blurring for the rotational motion-corrupted case than for the translational motion-corrupted case.

That said, this simple method for mitigating artifacts does not work if motions occur near β = 180 positions. In other words, when motions occur near β = 180 and in both half circles of the scanning positions, the maximum number of consecutive stable projections would be less than 180, which is a minimum requirement for a meaningful reconstruction. In that case, the counterpart projections of the projections near $\beta = 180^{o}$ do not exist in the maximum consecutive stable projections. Thus, the maximum number of consecutive stable projections used in the reconstruction process would be the only usable projections. For a combined motion-corrupted case where only 159 consecutive stable projections are available, the above reconstruction process produces some artifacts (such as a broken skull and ghost artifacts) in the reconstructed images (as shown in Fig. 4.12). If it were possible to know the parameters of motions, then the reconstruction voxels corresponding to the remaining projections could be repositioned in such a way that the remaining projections would have become usable during the reconstruction process. In the next chapter, an innovative marker-based motion detection technique is proposed to estimate parameters of motions.

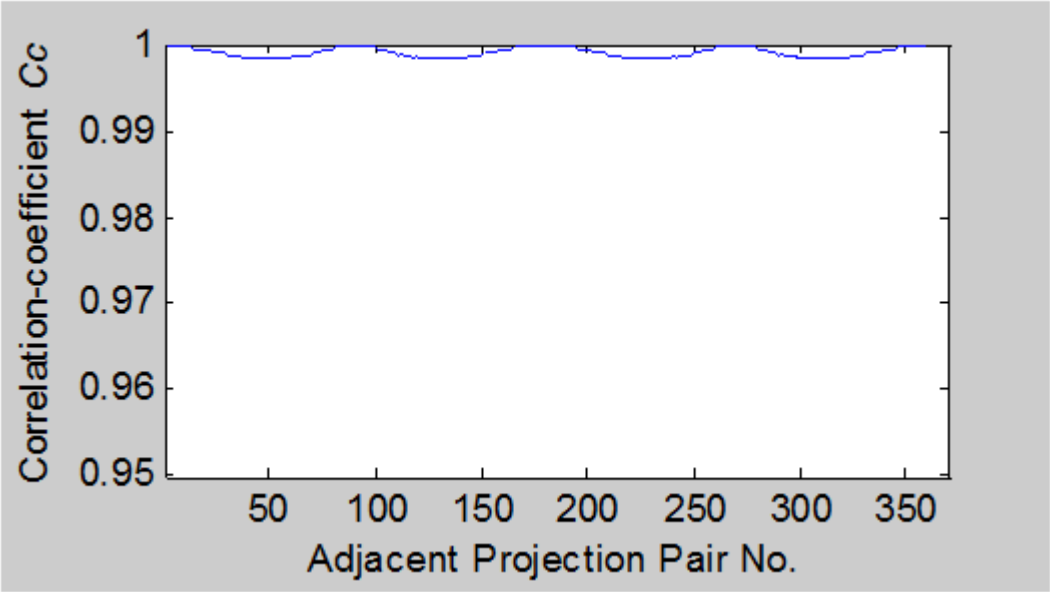

Figure 4.4 Correlation-coefficient for Motion Free Ideal Case

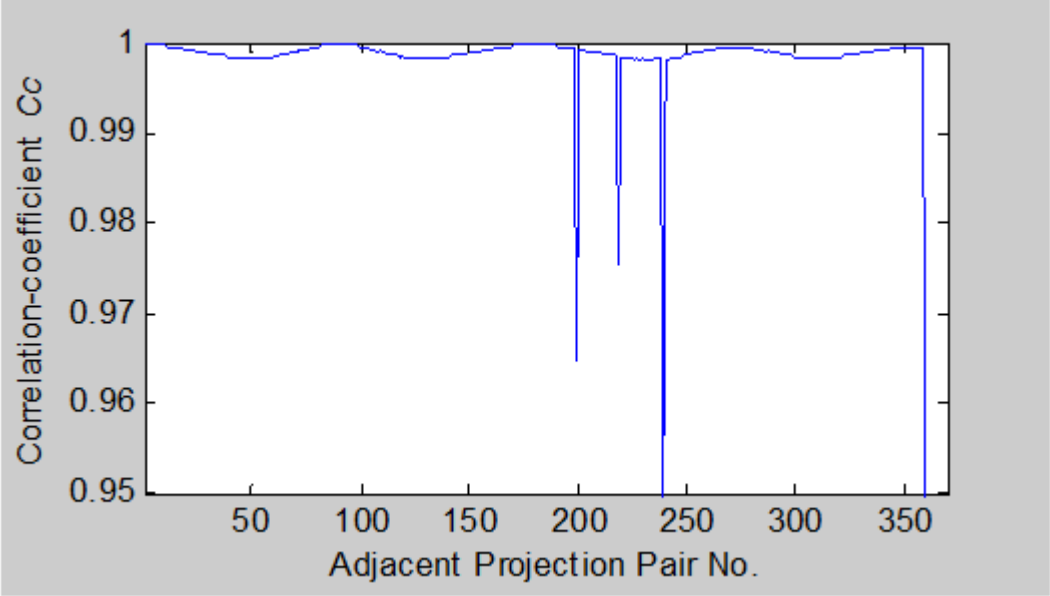

Figure 4.5 Correlation-Coefficient for Translational Motion Case

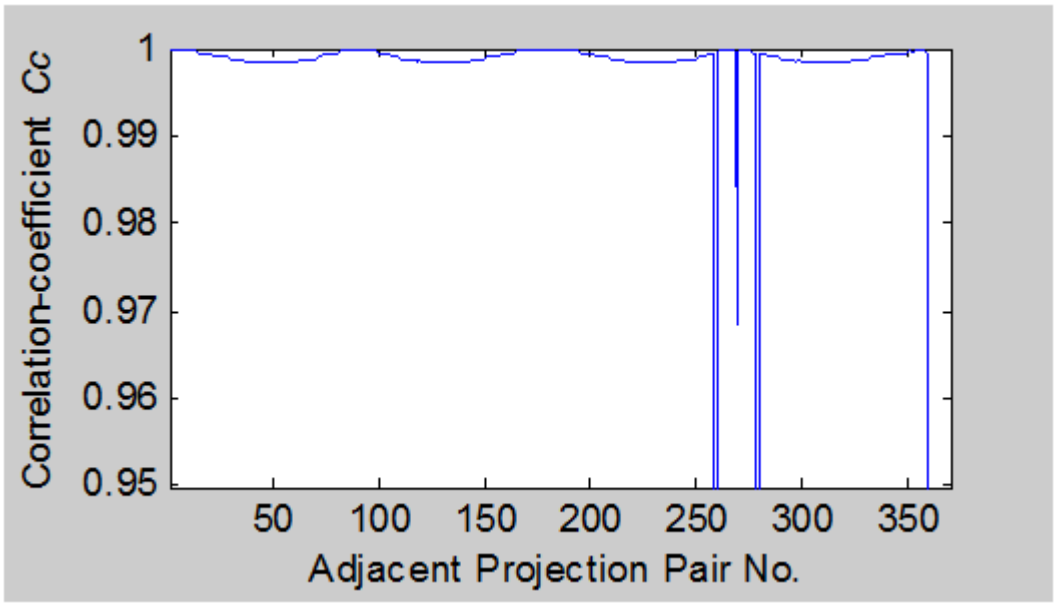

Figure 4.6 Correlation-Coefficient for Rotational Motion Case.

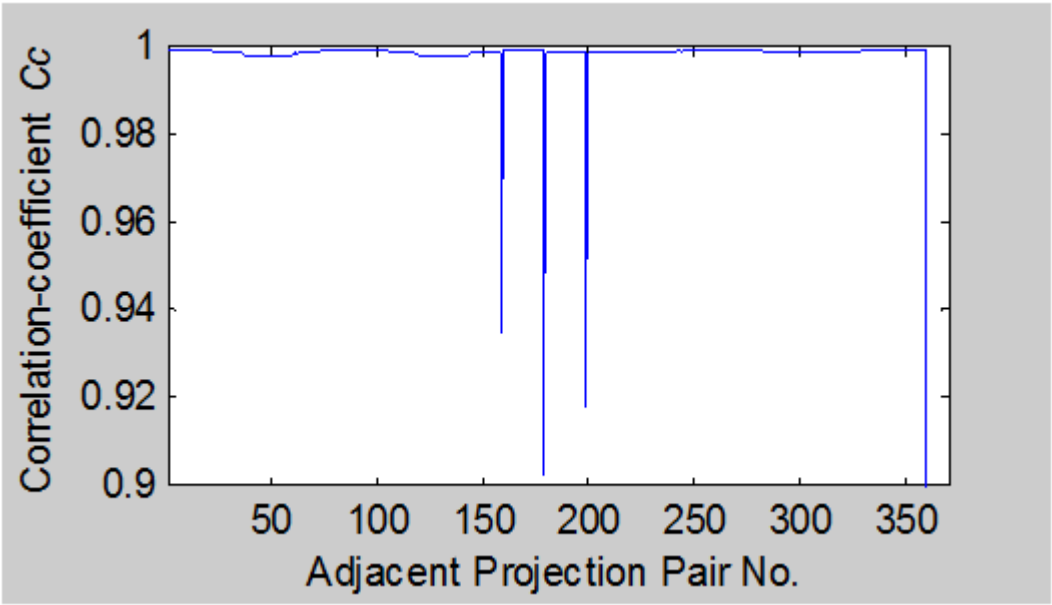

Figure 4.7 Correlation-Coefficient for Combined Rotational and Translational Motion Corrupted Case.

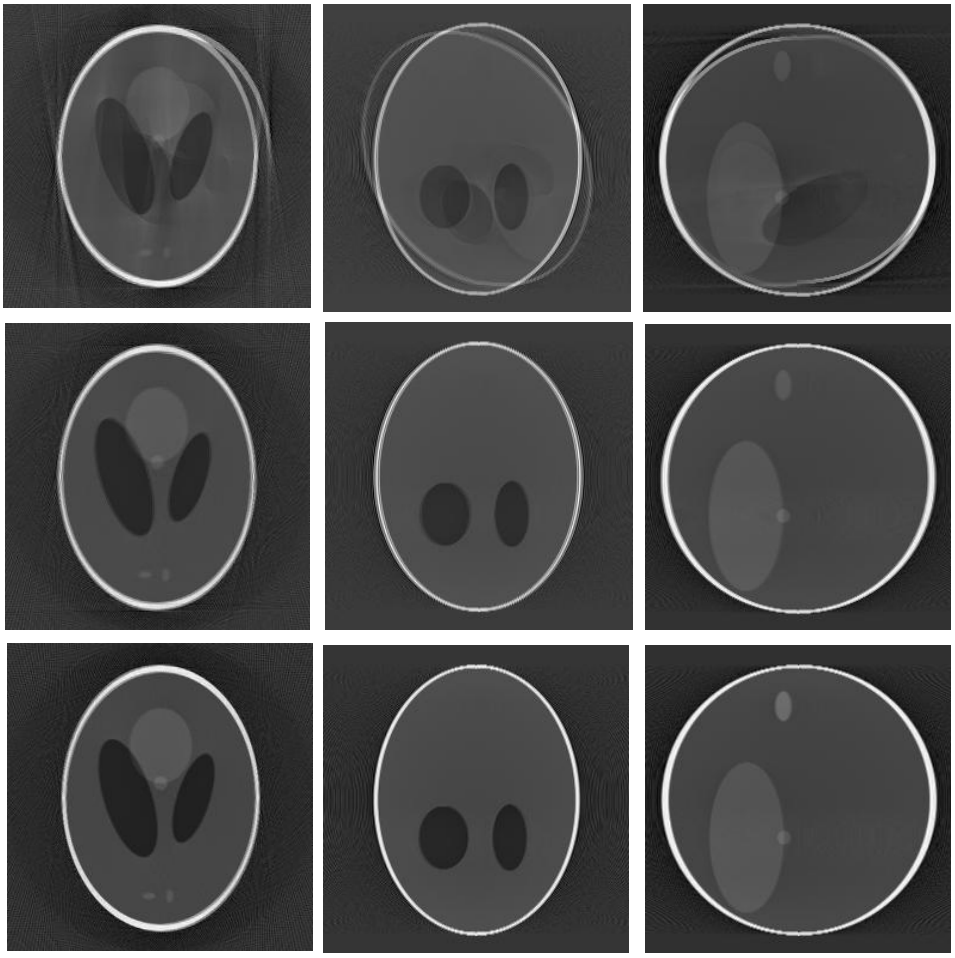

a b c
d e f
g h i

Figure 4.8 (a-c) Axial, Coronal and Sagittal Slices of Rotational Motion Corrupted Case. (d-f) Similar Slices after Motion Compensation. (g-h) Similar Slices of Motion Free Case

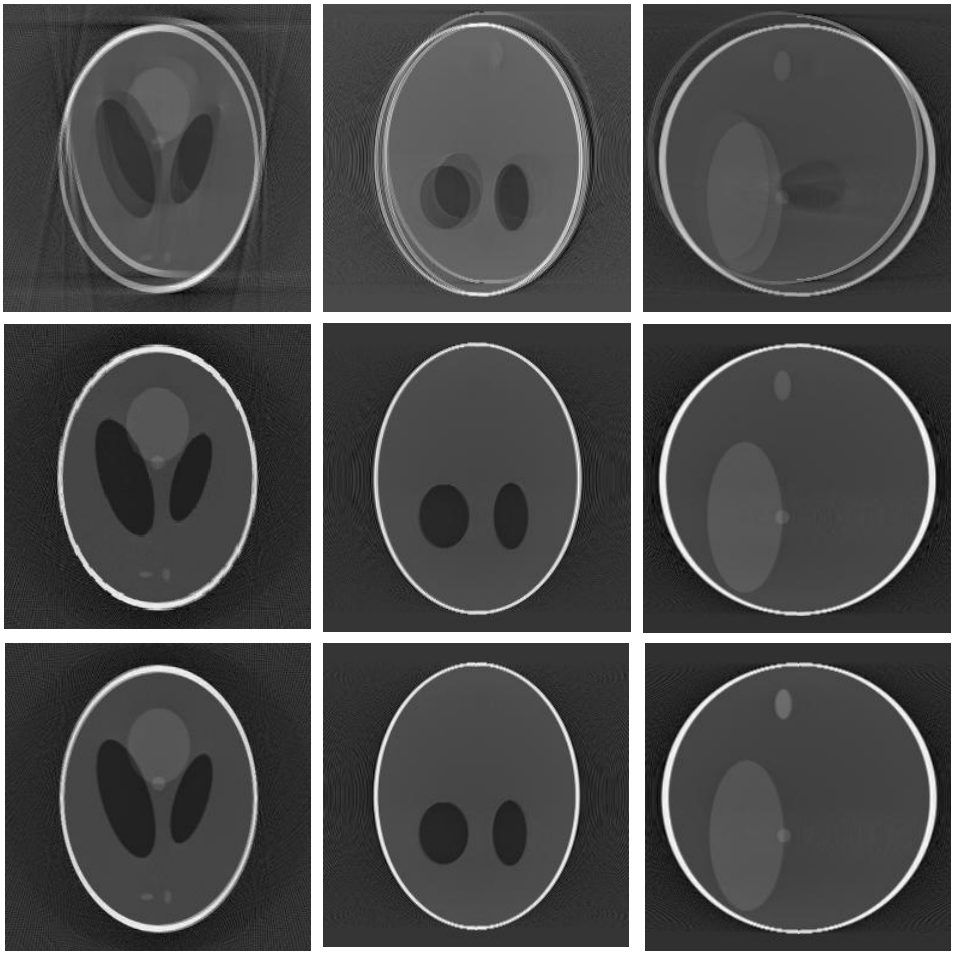

a b c
d e f
g h i

Figure 4.9 (a-c) Axial, Coronal and Sagittal Slices of Translational Motion Corrupted Case. (d-f) Similar Slices after Motion Compensation. (g-i) Similar Slices of Motion Free Case

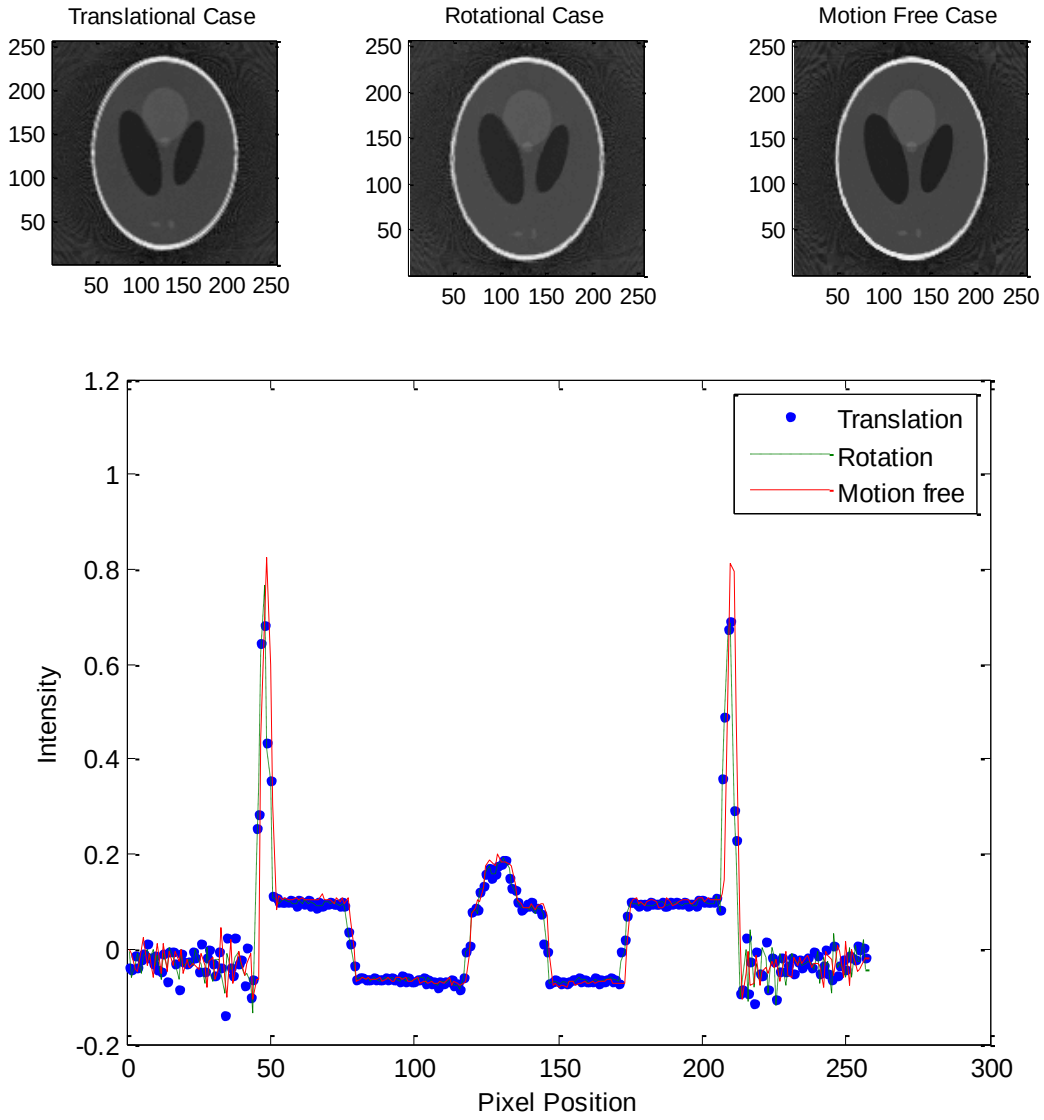

Figure 4.10 Plot of the One Pixel Wide Reconstruction Line at Y=129th Position

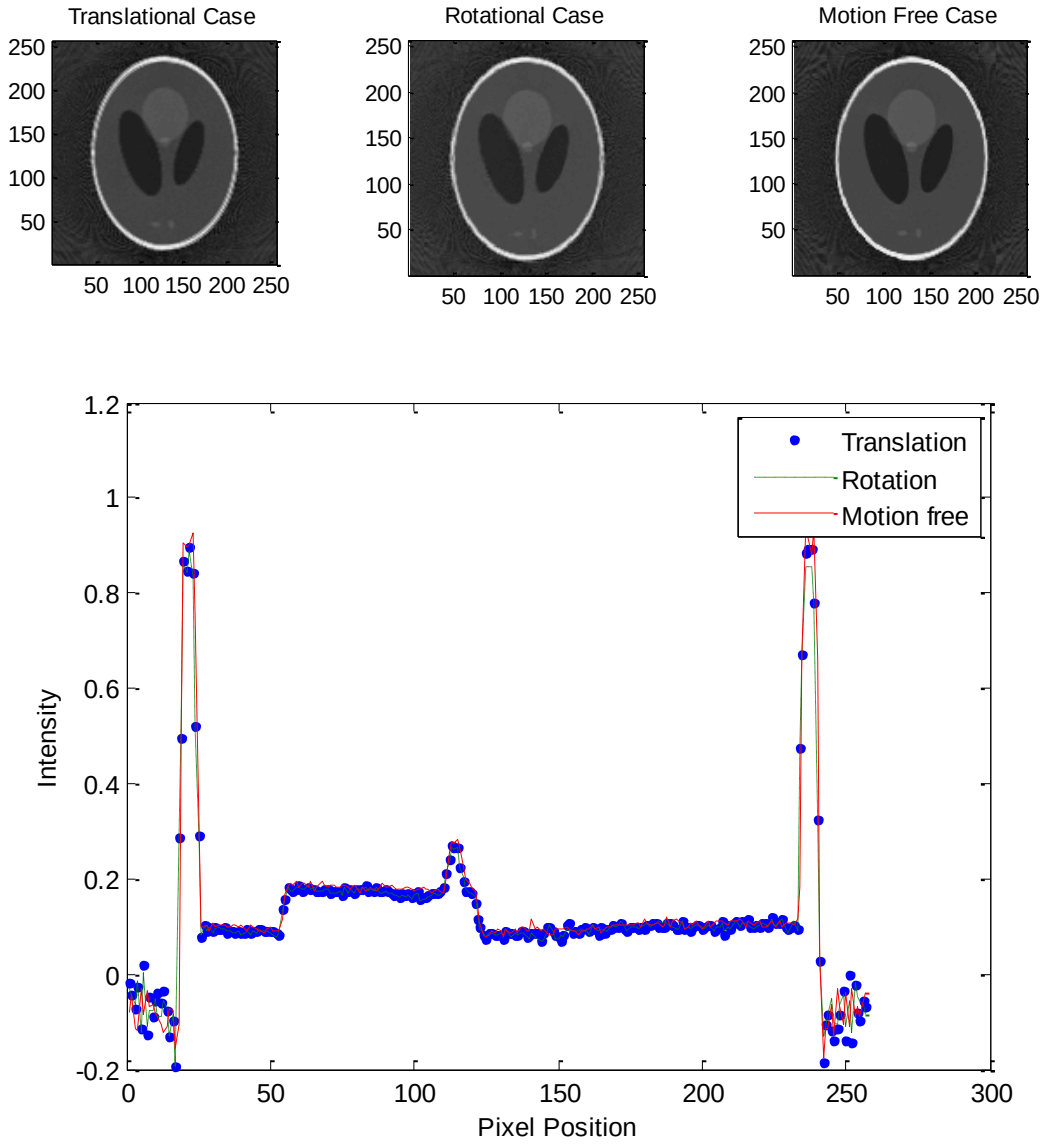

Figure 4.11 Plot of the One Pixel Wide Reconstruction Line at X=118th Position

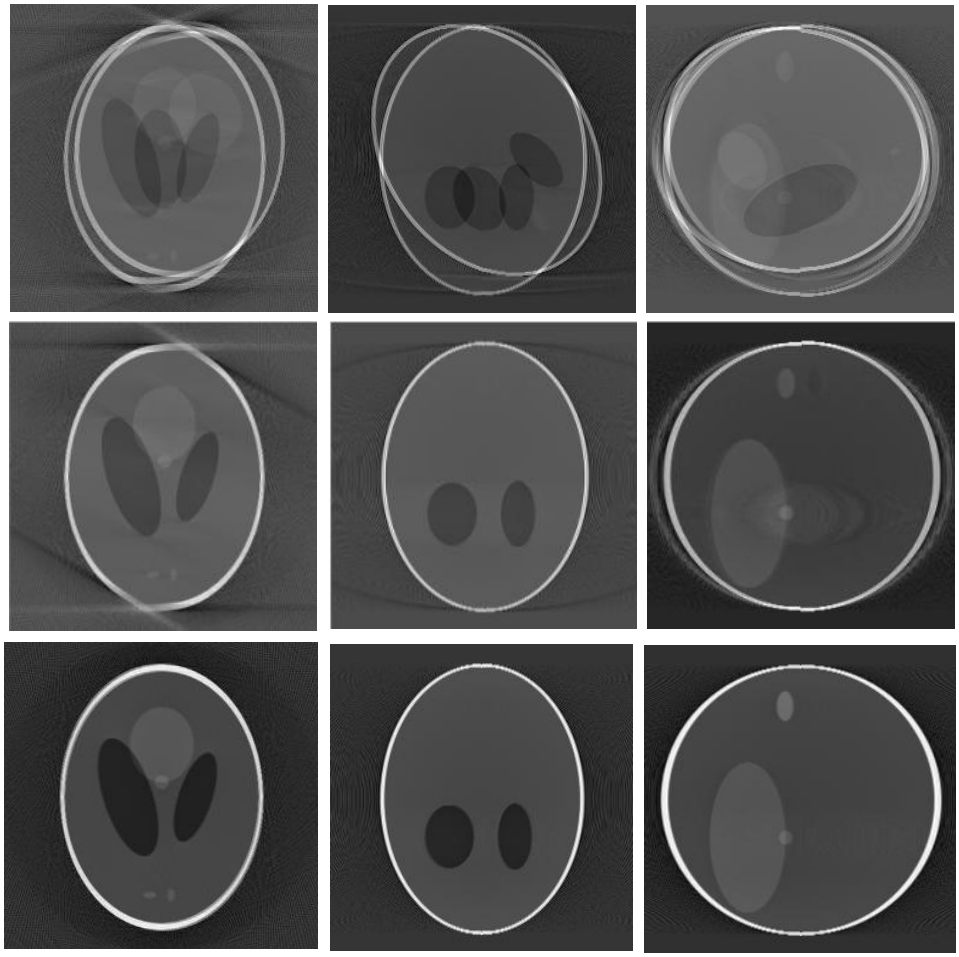

a b c
d e f
g h i

Figure 4.12 (a-c) Axial, Coronal and Sagittal Slices of Combined Motion Corrupted Case. (d-f) Similar Slices after Motion Compensation with Limited No. of Projections. (g-i) Similar Slices of Motion Free Case

CHAPTER 5

MARKER-BASED HEAD MOTION MEASUREMENT SYSTEM

5.1 Introduction

The idea behind the Marker-Based Motion Detector (MBMD) system is to detect head motion during computer tomography (CT) scans without using any external motion tracking sensors. The proposed system, which is implemented in Circular cone-beam CT assembly (as shown in Fig. 5.1), uses four markers to detect rotational and translational parameters (six degrees of freedom) of motion. In this proposed system, the markers are placed on a head surface in such a way that their three-dimensional (3D) positions (coordinates) will always be linearly independent and their projections on the X-ray detector plate will never cross each other in the case of any practical head motion. The number of markers and their linear independence are the two necessary conditions for finding the motion parameters. The coordinates of the markers on head and their corresponding projections on the detector plate are known for a motion-free ideal case. In case of any head motion during the CT scan, the markers and their corresponding projections will shift from their ideal positions. However, the relative distances between the markers will always remain constant because they are on the solid body. The new positions of the markers' projections are known from the detector plate but the new

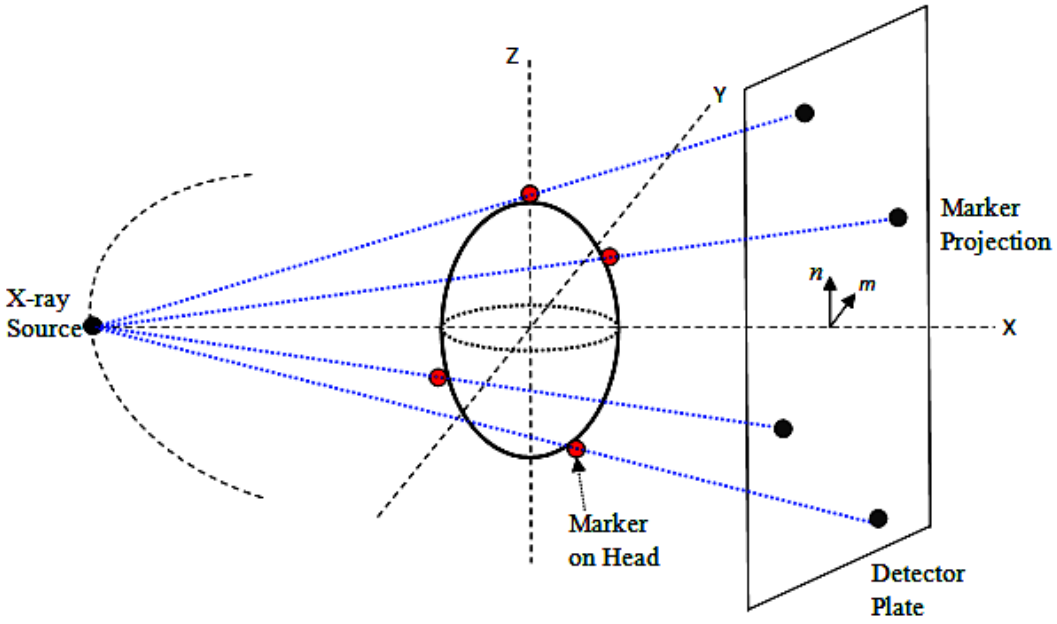

Figure 5.1 Cone-Beam CT Assembly with Markers

positions of the markers are not known. In this proposed MBMD system, the new positions of the shifted markers are estimated from an iterative numerical optimization technique that minimizes the differences between the known relative distances among the marker positions and the corresponding relative distances among the estimated marker positions. Once the new positions of the shifted markers are known, the motion parameters can easily be calculated from the estimated shifted marker positions and their corresponding ideal marker positions.

5.2 Illustration of the MBMD System

In order to make the calculation easier, the source, detector and markers coordinates are represented in the same coordinate system, as shown in Fig. 5.2, where the source is considered as the origin of the coordinate system. The proposed MBMD system is illustrated step by step in the following section:

1) As shown in Fig. 5.2, The MBMD system has four points ($x_i y_i z_i$, $where\ i = 1,2,3,4$), called markers, in a 3D coordinate system. The markers are placed on a rigid body. Coordinates of the initial marker positions are known.

2) From one point in space (0,0,0), (which is called the X-ray source), four lines as defined by Eq. (5.1) are drawn through these four markers. These lines will intersect a plane, which is called the X-ray detector. The coordinates of these four intersection points ($\bar{x}_i\ \bar{y}_i \bar{z}_i$, $where\ i = 1,2,3,4$), as shown in Fig. 5.4, are called the marker projections on the detector plate.

$$\frac{x}{y} = \frac{\bar{x}_i}{\bar{y}_i}, \qquad \frac{y}{z} = \frac{\bar{y}_i}{\bar{z}_i} \tag{5. 1}$$

3) Now the four points (markers) are shifted because of motion. The coordinates of the shifted markers $(x'_i y'_i z'_i)$, are not known anymore. The only known is that the relative distances (Eq. 5.2 and 5.3) between the markers, as shown in Fig. 5.3, are fixed because of the solid body.

$$\sqrt{(x_i - x_j)^2 + (y_i - y_j)^2 + (z_i - z_j)^2} = d_{ij} \tag{5. 2}$$

$$\sqrt{(x'_i - x'_j)^2 + (y'_i - y'_j)^2 + (z'_i - z'_j)^2} = d_{ij} \tag{5. 3}$$

$$for \; \forall \; j > i$$

Where

$$i = 1, 2, 3 \; and \; j = 2, 3, 4$$

4) If four lines Eq. (5.4) are drawn from the source through these four shifted markers, they will intersect the same plane, (the X-ray detector) in four new points ($\bar{x}_i' \bar{y}_i' \bar{z}_i' \; where \; i = 1,2,3,4$). The coordinates of these four intersection points, as shown in Fig. 5.4, are known from the detector plate

$$\frac{x}{y} = \frac{\bar{x}'_i}{\bar{y}'_i}, \qquad \frac{y}{z} = \frac{\bar{y}'_i}{\bar{z}'_i} \tag{5. 4}$$

5) Now the goal is to find the coordinates of the shifted markers $(x'_i y'_i z'_i \; where \; i =$ *1,2,3,4* from the information described in steps 1, 2, 3, and 4.

In other words, the problem boils down to calculating (4×3) =12 coordinates of the four shifted markers from six relative distances (Euclidean distances) between the markers and four straight lines (linear in x, y and z) equations (i.e. calculating marker positions from six nonlinear and four linear equations). This system of equations is solved numerically by the following iterative optimization technique.

5.3 Numerical Iterative Optimization

The first step in our numerical optimization technique is to find the shifted markers' approximate positions ($x_i'' \, y_i'' \, z_i'', \quad where \;\; i = 1,2,3,4$). As shown in Fig. 5.5, the approximate position of the shifted marker 1 can be found by drawing a line parallel to the line between the projections $(\bar{x}_1 \, \bar{y}_1 \bar{z}_1)$ and $(\bar{x}_1{}' \, \bar{y}_1{}' \bar{z}_1{}')$ from its ideal marker position to the shifted line. The intersection point $(x_1'' \, y_1'' \, z_1'')$ is the approximate position of the shifted marker 1. The generalized formula for finding the approximate positions of the shifted markers is given by (5.5)

$$z_i'' = \frac{K_{i2} \pm \sqrt{K_{i2}^2 - 4K_{i1}K_{i3}}}{2K_{i3}} \quad \begin{cases} + \, if \; z_i \; is \; positive \\ - \, if \; z_i \; is \; negative \end{cases}$$

$$y_i'' = z_i'' \frac{\bar{x}'_i}{\bar{z}'_i} \qquad ; \qquad x_i'' = z_i'' \frac{\bar{y}'_i}{\bar{z}'_i} \tag{5. 5}$$

where

$$i = 1,2,3,4$$

$$K_{i1} = (x_i^2 + y_i^2 + z_i^2) - d_{isp}^2$$

$$K_{i2} = \left(2x_i \frac{\bar{x}'_i}{\bar{z}'_i} + 2y_i \frac{\bar{y}'_i}{\bar{z}'_i} + 2z_i \right)$$

$$K_{i3} = \left(\frac{\bar{x}'^2_i}{\bar{z}'^2_i} + \frac{\bar{y}'^2_i}{\bar{z}'^2_i} + 1 \right)$$

$$d_{isp} = \frac{d_{is}}{K}$$

$$d_{is} = \sqrt{(\bar{x}_i - \bar{x}'_i)^2 + (\bar{y}_i - \bar{y}'_i)^2 + (\bar{z}_i - \bar{z}'_i)^2}$$

$$K = \frac{SDD}{x_i}$$

SDD *is the distance between the source and the detector*

After finding the approximate marker positions, $(x_i'' \; y_i'' \; z_i'')$, the relative distances d_{ij}'' between them Eq. (5.6) need to be calculated.

$$d_{ij}'' = \sqrt{\left(x_i'' - x_j''\right)^2 + \left(y_i'' - y_j''\right)^2 + \left(z_i'' - z_j''\right)^2} \tag{5.6}$$

$for \; \forall \; j > i$

where

$i = 1, 2, 3 \; and \; j = 2, 3, 4$

If these relatives distances d_{ij}'' are close to the d_{ij} (the relative distances between the ideal marker positions), then the approximation is good. Otherwise, the positions of the approximate markers positions have to be varied along their corresponding shifted lines so that their relative distances become very close to the ideal distances d_{ij}. Once the relative distances are within the error limit,

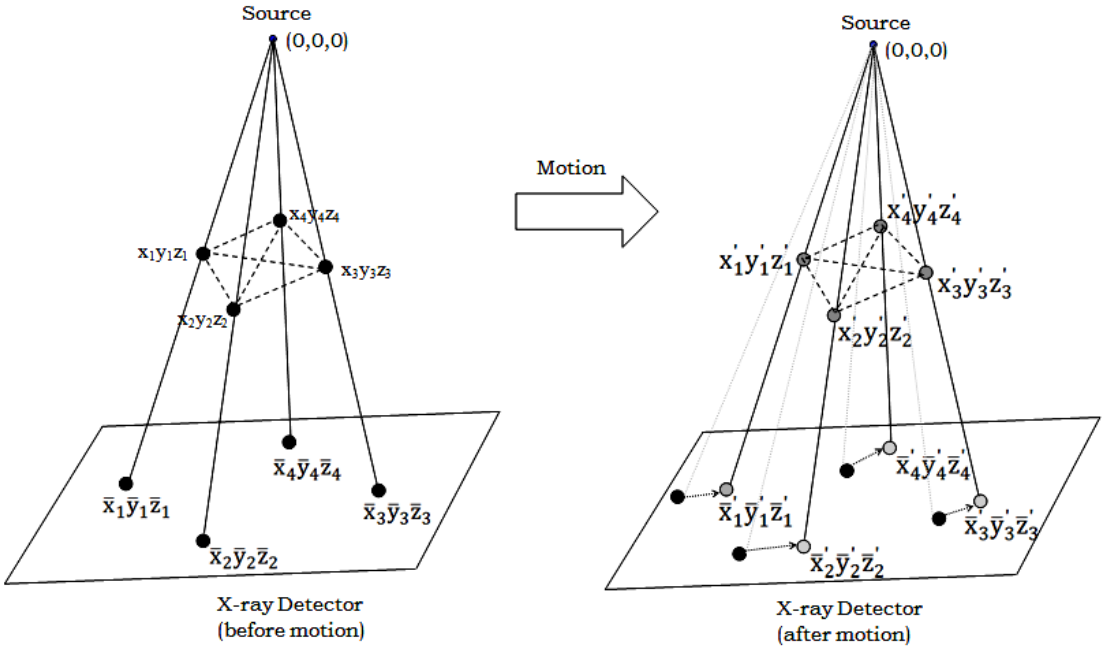

Figure 5.2 Source, Detector and Markers Showing Motion

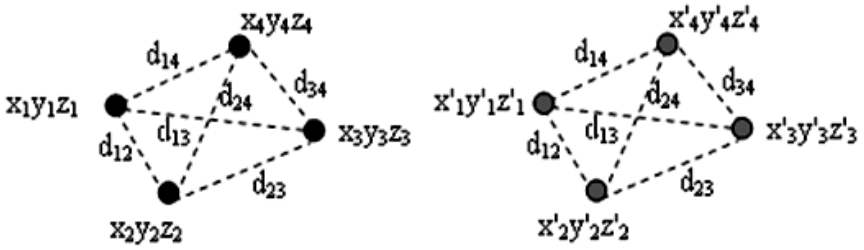

Figure 5.3 Relative Distances between Markers
(Left-Before Motion, Right-After Motion)

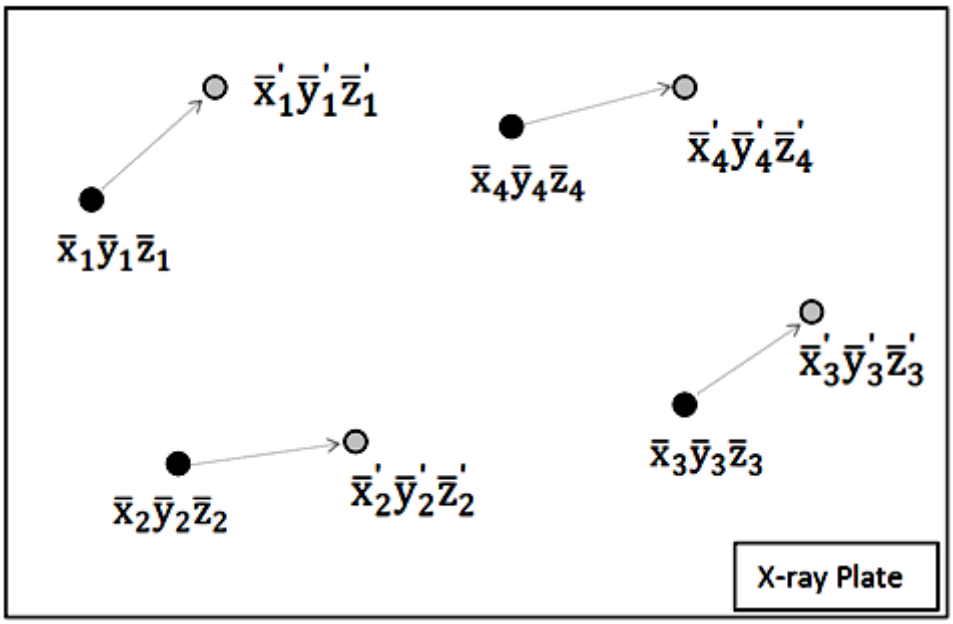

Figure 5.2 Markers Projections Before and After Motion

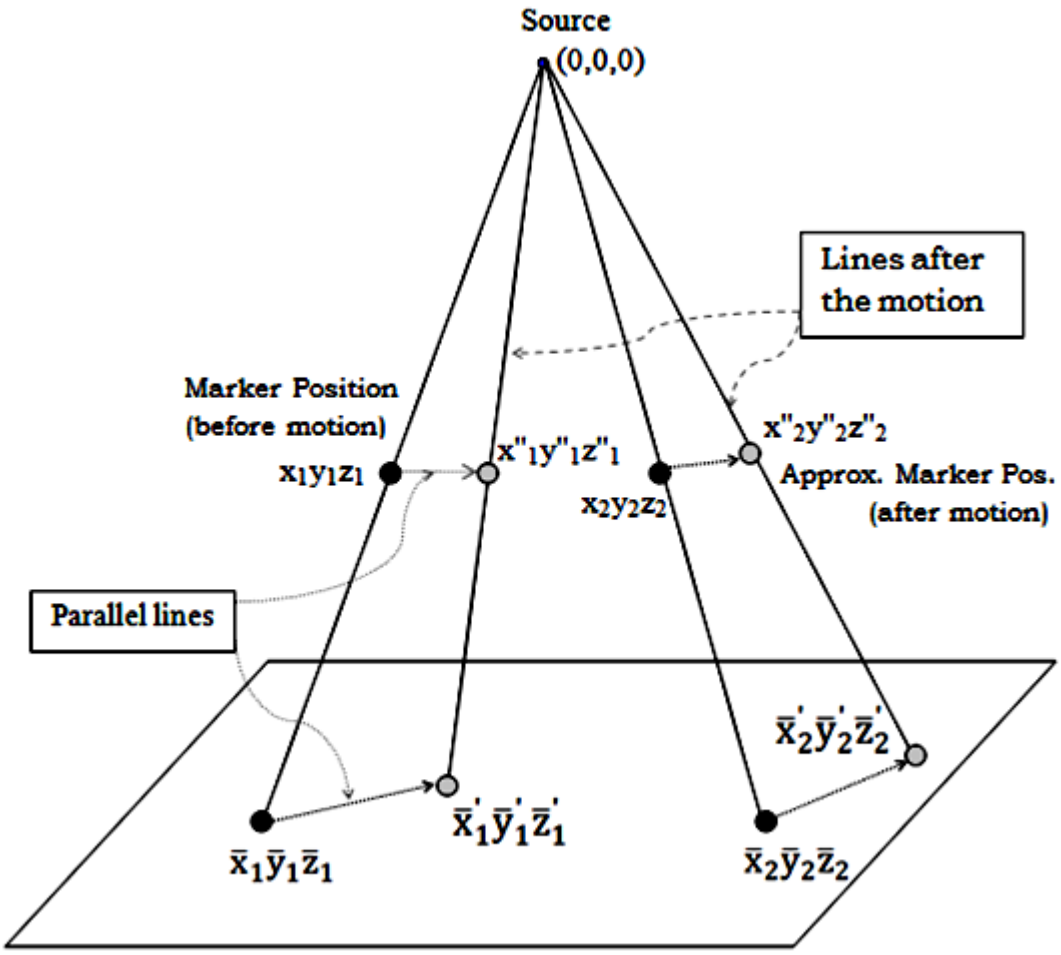

Figure 5.3 Approximate Coordinates of Two Markers After Motion

in other words, when

$$\sum_{ij} abs\left(d''_{ij} - d_{ij}\right) \leq Error$$

It can be claimed that

$$x''_i \approx x'_i,\ y''_i \approx y'_i,\ z''_i \approx z'_i \quad where\ i = 1,2,3,4 \tag{5.7}$$

After finding the shifted marker positions$\left(x'_i y'_i z'_i\right)$, the motion parameters can easily be extracted from the following equation (5.8) [85]:

$$\begin{bmatrix} x_1 & x_2 & x_3 & x_4 \\ y_1 & y_2 & y_3 & y_4 \\ z_1 & z_2 & z_3 & z_4 \\ 1 & 1 & 1 & 1 \end{bmatrix} = \begin{bmatrix} r_{11} & r_{12} & r_{13} & t_{xe} \\ r_{21} & r_{22} & r_{23} & t_{ye} \\ r_{31} & r_{32} & r_{33} & t_{ze} \\ 0 & 0 & 0 & 1 \end{bmatrix} \times \begin{bmatrix} x'_1 & x'_2 & x'_3 & x'_4 \\ y'_1 & y'_2 & y'_3 & y'_4 \\ z'_1 & z'_2 & z'_3 & z'_4 \\ 1 & 1 & 1 & 1 \end{bmatrix} \tag{5.8}$$

where

$$r_{11} = \cos\alpha_e \cos\vartheta_e\ ; \qquad r_{21} = \sin\alpha_e \cos\vartheta_e$$

$$r_{32} = \sin\delta_e \cos\vartheta_e\ ; \qquad r_{33} = \cos\vartheta_e \cos\delta_e$$

$$r_{12} = \cos\alpha_e \sin\vartheta_e \sin\delta_e - \cos\delta_e \sin\alpha_e$$

$$r_{13} = \cos\alpha_e \sin\vartheta_e \cos\delta_e - \sin\alpha_e \sin\delta_e$$

$$r_{22} = \sin\alpha_e \sin\vartheta_e \sin\delta_e + \cos\alpha_e \cos\delta_e$$

$$r_{23} = \sin\alpha_e \sin\vartheta_e \cos\delta_e - \cos\alpha_e \sin\delta_e$$

$$r_{31} = -\sin\vartheta_e$$

Estimated six degrees of freedom of motion are:

$\alpha_e - rotation\ about\ z\ (yaw)$

$\vartheta_e - rotation\ about\ y\ (pitch)$

$\delta_e - rotation\ about\ x\ (roll)$ *and*

$t_{xe}, t_{ye}, t_{ze}\ are\ the\ translation\ parameters$

Since the marker coordinates are linearly independent for any form of practical motion, the solution of (5.8) will always exist.

Iteration steps: Since any head is of a finite size, the maximum possible segment of a shifted line where a marker can take position after motion is also finite. Instead of choosing the maximum possible length, some approximated line segment, L, of the shifted line around $(x_i'' \; y_i'' \; z_i'')$ is chosen for the iteration. Segment L could be chosen based on the initial knowledge of the amount of head movement, which can be guessed either from the distance between the ideal and shifted marker projections. After choosing L, L is divided into N equal parts for our iteration. Obviously, large values of N will produce better accuracy. The iteration is performed in several stages. In the first stage, (using L) attempt to find the closest possible coarse solution (i.e. coordinate of the shifted marker position). After getting the closest possible coarse marker positions, a smaller length (half of the previous length) (L/2) is chosen around the estimated coarse marker position and divided again by N equal parts for the next iteration. The process is repeated until the desired error margin is reached. If the process does not converge, then the length (L) and the number of iterations need to be increased. In the following chapter, this algorithm is tested with a range of simulated motion. Simulation results demonstrate a significant improvement in terms of accuracy, linearity and range compared to the existing external sensor-based method.

Another important issue that needs to be discussed is the assumption that the initial marker positions (i.e. the coordinates of ideal motion-free makers) are known. This assumption can be justified because the initial position of a marker can easily be calculated from the distance between the source and the marker (which can be measured physically from the system) and the projection coordinate of that corresponding marker. Using the simple geometry of Fig. 5.2, it can be written as

$$\frac{x_i}{y_i} = \frac{\bar{x}_i}{\bar{y}_i}, \qquad \frac{y_i}{z_i} = \frac{\bar{y}_i}{\bar{z}_i} \tag{5.9}$$

$$\sqrt{(x_i)^2 + (y_i)^2 + (z_i)^2} = d_i \tag{5.10}$$

where

$i = 1,2,3,4$

$x_i y_i z_i$ = Markers' coordinates

$\bar{x}_i\ \bar{y}_i \bar{z}_i$ = Markers' projection coordinates

d_i = Measured Distance between the source (0,0,0) and markers

Using Eqn. (5.9) and (5.10), the initial coordinates of the ideal motion-free markers can easily be found.

CHAPTER 6

RESULTS AND EVALUATION

6.1 Introduction

In this chapter, the modified three-dimensional (3D) Shepp-Logan model of Fig. 6.1 has been designed for simulations. The model consists of four markers and ten superimposed ellipsoids with different attenuation coefficients (CT values). In practical situations, the markers need to be placed on a head surface in such a way that their positions will always be linearly independent and their projections on the X-ray detector plate will never cross each other in the case of any practical head motion. Some of the X-ray projections of the modified 3D Shepp-Logan Phantom are plotted in Fig. 6.2. The geometric locations, sizes and CT values of the ellipsoids used in the model are listed in Table 6.1. As discussed before, CT values of water and air are 0 and -1000Hu respectively, while that of the bone varies from +100 to more than +1000Hu. In our simulation, the CT values of the ellipsoids are chosen to simulate high contrast markers, soft tissue, bone and other matters (such as tumors in the brain).

In order to apply the Marker Based Motion Detection (MBMD) system on the 3D Shepp-Logan phantom, the coordinates of the marker projections on the detector plate have to be known for every X-ray projection of the phantom. The coordinates of the marker projections on a detector plate can easily be found by following the simple image

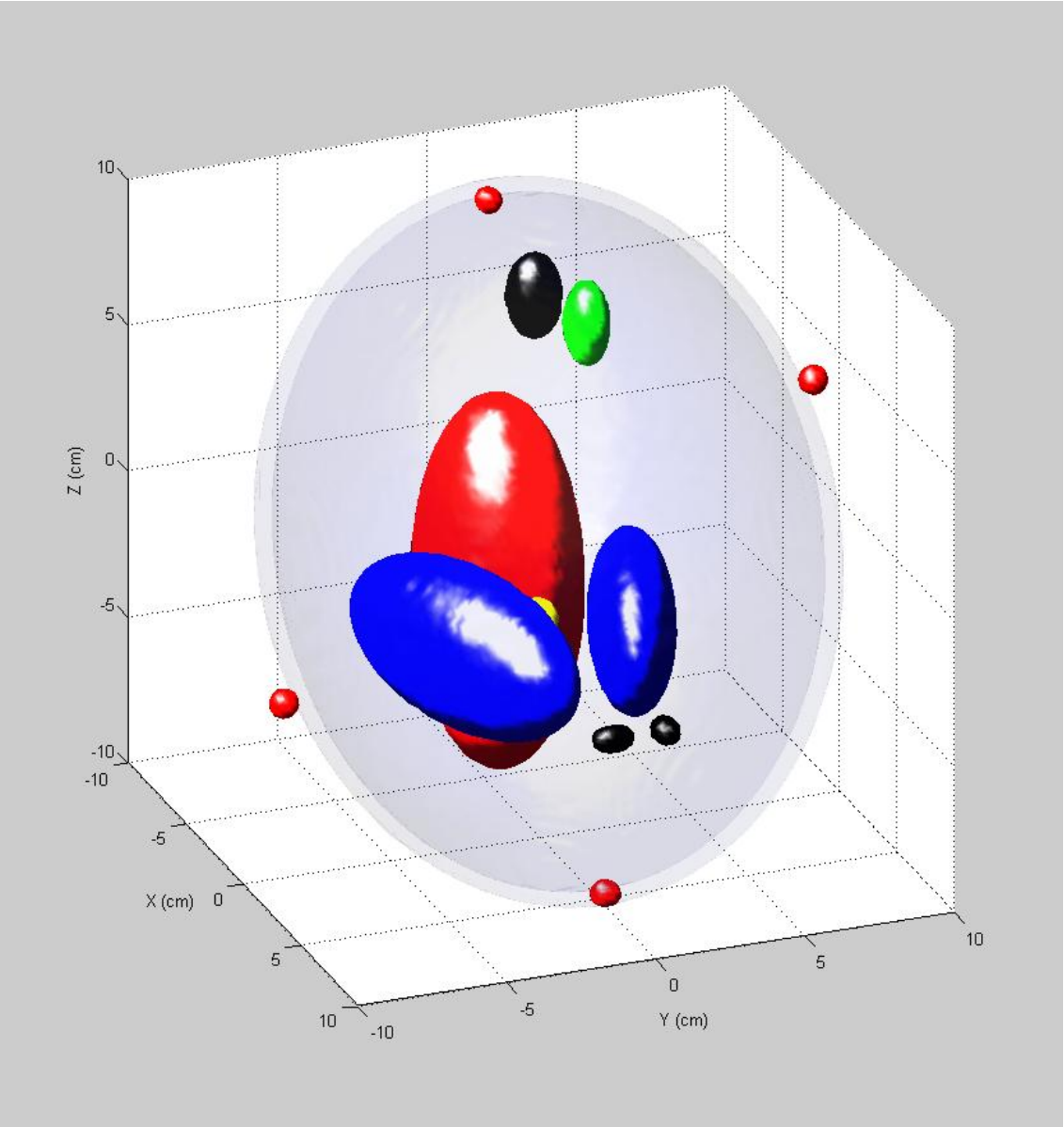

Figure 6.1 A 3D Version of the Shepp-Logan Phantom with Markers

Table 6.1 Parameters of the Modified 3D Shepp-Logan Phantom

	Center Coordinate (cm)			Half axis (cm)			Rotation angle (°)			CT Value
	x_o	y_o	z_o	a	b	c	φ	ψ	ξ	ρ
Markers	0	0	9.25	0.25	0.25	0.25	0	0	0	5000
	7.25	0	3.25	0.25	0.25	0.25	0	0	0	5000
	0	-7.25	-3.25	0.25	0.25	0.25	0	0	0	5000
	-0.75	0.75	-9.25	0.25	0.25	0.25	0	0	0	5000
Ellipsoids	0	0	0	6.90	9.20	9.00	0	0	0	1000
	0	0	0	6.62	8.74	8.80	0	0	0	-800
	-2.2	0	-2.5	4.10	1.60	2.10	108	0	0	-200
	2.2	0	-2.5	3.10	1.10	2.20	72	0	0	-200
	0	3.5	-2.5	2.10	2.50	5.00	0	0	0	100
	0	1.0	-2.5	0.46	0.46	0.46	0	0	0	100
	-0.8	-6.5	-2.5	0.46	0.23	0.20	0	0	0	100
	0.6	-6.5	-2.5	0.46	0.23	0.20	90	0	0	100
	0.6	-1.05	6.25	0.56	0.40	1.00	90	0	0	100
	0	1.0	6.25	0.56	0.56	1.00	0	0	0	100

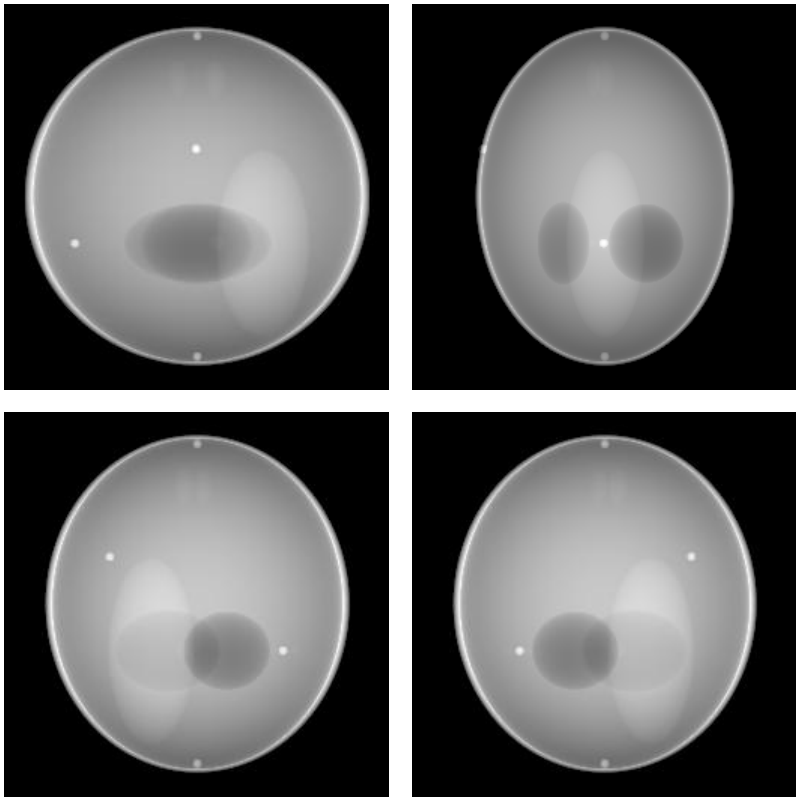

a b
c d

Figure 6.2 X-Ray Projections of the Phantom at Different Source Positions. (a-d) $\beta = 0^o, 90^o, 135^o, 315^o$

processing steps as shown in Fig. 6.3. The first step for finding center coordinates of maker projections is to segment the marker projection using some suitable edge filter. In Fig. 6.3(b), a matlab "edge" function with "sobel" filter is used to segment the marker projections. Then segmented marker projections are dilated with suitable dilation function. In Fig. 6.3(c), a matlab "imdilate" function is used for filling the segmented marker projections. Then the segmented dilated marker projections are filled with a matlab "imfill" function as shown in Fig. 6.4 (d). Then a matlab "imclearborder" function is used to remove the lighter structure from the edges of segmented dilated filled marker projections as shown in Fig. 9.4(e). In the final step, as shown in Fig.6.3 (f), a matlab "imerode' function is used to convert the clear bordered marker projection in to a square size marker projection. The center of the squared marker projections are the coordinates of marker projections. Once the coordinates of marker projections are known, the numerical optimization steps of the MBMD system can be applied to estimate the coordinates of markers after motion. After finding the location of motion (i.e. the source detector positions where motion occured during the CT scan) and the parameters of head motions (six degrees of freedom of head motion), a modified FDK algorithm and MBMD-FDK algorithm is applied to mitigate motion artifacts during the reconstruction process.

6.2 Simulation of Motion Parameters Estimation

The performance of the proposed MBMD system is tested in two stages. In the first stage, the linearity and accuracy of the MBMD system is tested with six known sets of motion (three rotational and three translational). In the second stage, the performance of the

MBMD system is tested with all three motion-corrupted cases mentioned in Chapter 4. As mentioned in Chapter 5, in order to estimate the motion parameters efficiently, some approximated line segment (L) of the shifted line around$(x_i'' \; y_i'' \; z_i'')$ (as shown in Fig. 5.3) is chosen for the iteration. Segment L could be chosen based on the distance between the ideal and shifted marker projections. After choosing L, divide L into N equal parts. Obviously, large values of N will produce better accuracy (for the 1st stage of verification, N=150 and L=2.5cm and for the 2nd stage of verification, N=80 and L= 2cm, 3.5cm and 5cm for Translational, Rotational and combined motion-corrupted cases respectively). The iteration is performed in several stages. In the first stage (using L), attempt to find the closest possible coarse solution (i.e coordinate of the shifted marker position). After getting the closest possible coarse marker position, a smaller length is chosen (half of the previous length) (L/2) around the estimated coarse marker position and divided again by N equal parts for the next iteration. The process is repeated until it reaches the desired *error* margin (*error* Margin=0.0005cm). If the process does not converge, then the L and the number of iterations need to be increased.

In the first stage of verification, each of the six parameters of motion are tested separately to validate the accuracy and linearity of the MBMD system. At the time of testing translational motion parameters, the 3D Shepp-Logan Phantom is perturbed with a range of axial, lateral, and vertical motion parameters individually in three separate scans. Similarly, for testing rotational motion parameters, the Phantom is perturbed with a range of roll, pitch, and yaw motion parameters individually in three separate scans. For a translational motion case, the range of motion is -6mm to 6mm, and for a rotational motion case, the range of motion is -5^o to 5^o. Simulation results of estimated marker -

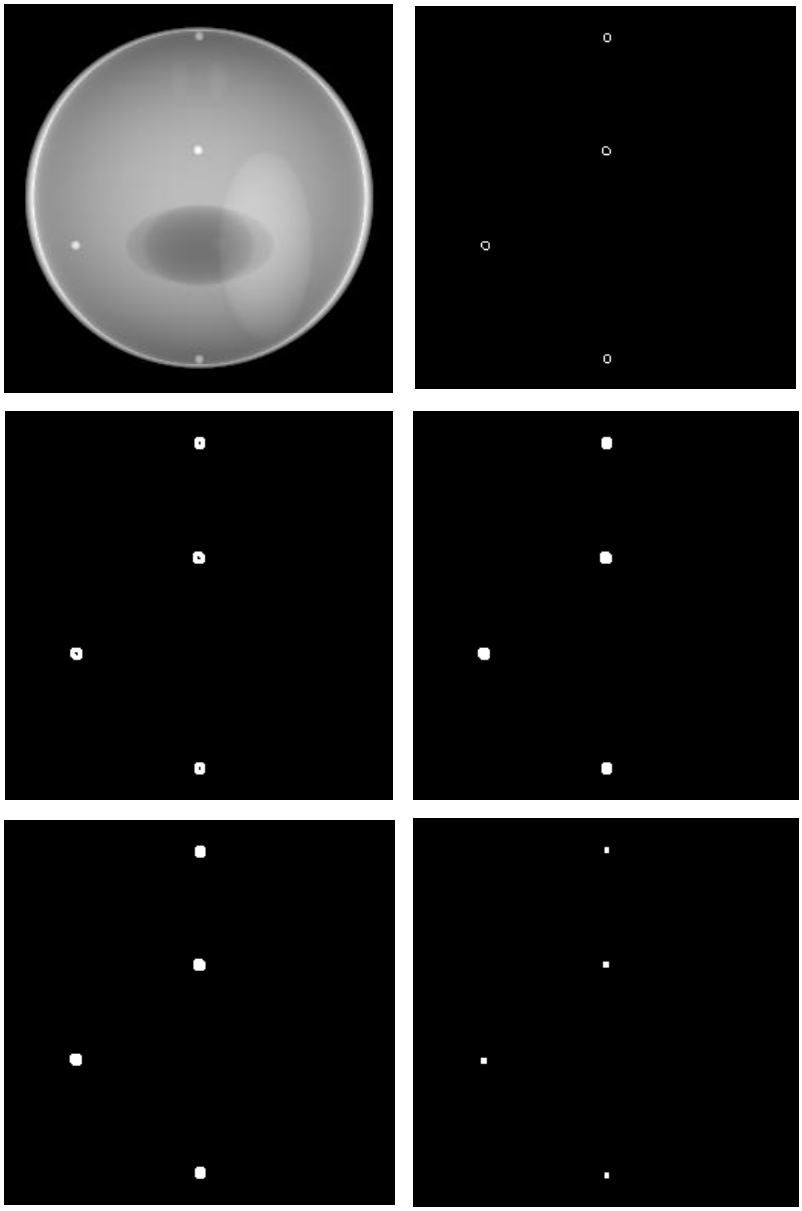

a b
c d Figure 6.3 Finding Coordinates of Marker Projections
e f

(a) X-Ray Projection of the Phantom with Markers. (b) Binary Gradient Mask of Markers Projection (c) Dilated Gradient Mask. (d) Binary Image with Filled Holes. (e) Cleared Border Image. (f) Eroded Segmented Image

coordinates and the corresponding motion parameters are listed in the following tables (6.2-6.19). The results of the simulation outcome are also plotted in Figs. (6.4-6.9). The best fit line and line of identity are also plotted for verification. For clarity, a portion of every plot is also zoomed in under the main plot. The slopes and the square correlation coefficient (R^2) of the best fit lines through the data points are listed in table 6.20. A comparison of the results with the well known Goldstain *et al.* [66] optical sensor method is also given in table 6.20. The results demonstrate that the system is linear, with most slopes being within 1% of unity. The rms deviations of the MBMD data from the best-fit straight lines are less then 0.01^o for all rotation angles ($\pm 5^o$) and less than 0.02mm for the translations (±6mm). The rms deviation from the actual input is less than 0.02^o and 0.03cm for rotation and translation, respectively. The simulation results of square correlation coefficients (R^2) of the best fit lines through the data points demonstrate that the MBMD estimated data represent the real data values much better than the Goldstein method.

In the second stage of verification, the performance of our proposed marker-based estimator is tested with all the motion-corrupted cases, as shown in Figs. 6.10, 6.11, 6.12, and mentioned in Chapter 4. Simulation results of estimated markers coordinates and the corresponding motion parameters are listed in tables 6.22, 6.23, 6.25, 6.26, 6.28, 6.29. Estimated translation motion parameters are within 1.5% of the actual values and estimated rotational parameters are within 0.1% of the actual values. After finding the desired motion parameters, the following modified FDK algorithm, MBMD-FDK, is applied to mitigate motion artifacts.

6.3 MBMD-FDK Algorithm

The idea behind the MBMD-FDK algorithm is to mitigate motion artifacts by correcting the position of every reconstruction voxel in the back-projection stage according to the motion information acquired in the previous section.

The first step in MBMD-FDK algorithm is to find the location of motion. The location of motion can be detected either by continuously estimating the marker coordinates (in case of small or gradual motion) or by calculating the correlation between the adjacent projections (in case of large and abrupt variation of motion). The next step in MBMD-FDK algorithm is to find the estimated motion parameters corresponding to the location of motions. After finding the location of motions (β_m) and the estimated motion parameters, the following transformation matrix $[T]$ (which consists of the rotational parameters of motion) can be used to do the necessary coordinate transformation on the reconstruction grid so that the contribution of every projection will be placed to corresponding grid location of the reconstructed volume.

$$[T] = \begin{bmatrix} T_{11} & T_{12} & T_{13} \\ T_{21} & T_{22} & T_{23} \\ T_{31} & T_{32} & T_{33} \end{bmatrix} \tag{6.1}$$

where

$$T_{11} = \cos\Theta \cos\Omega$$

$$T_{12} = -\cos\Theta \sin\Omega$$

$$T_{13} = \sin\Theta$$

$$T_{21} = \sin\Omega \cos\Psi + \sin\Psi \sin\Theta \cos\Omega$$

$$T_{22} = \cos\Psi \cos\Omega - \sin\Psi \sin\Theta \sin\Omega$$

$$T_{23} = -\sin\Psi\cos\Theta$$

$$T_{31} = \sin\Psi\sin\Omega - \cos\Psi\sin\Theta\cos\Omega$$

$$T_{32} = \sin\Psi\cos\Theta + \sin\Omega\sin\Theta\cos\Psi$$

$$T_{33} = \cos\Psi\cos\Theta$$

In case of motion

$$\Theta = -\vartheta_e;\ \ \Psi = -\delta_e;\ \ \Omega = -\alpha_e;$$

Otherwise

$$\Theta = 0;\ \ \Psi = 0;\ \ \Omega = 0;$$

In this research, the following implementation steps are adopted for efficient implementation of the modified FDK algorithm. Modification of the FDK algorithm starts at step (9). In step (9), each projection is examined to find if there is motion. In case of motion, the rotational parameters of matrix $[T]$ are replaced with the estimated parameters (rotational) of motion followed by the necessary coordinate transformation in step (10). The whole idea is to correct the position of reconstruction grid so that during backprojection the contribution of every projection will be placed in its corresponding position.

Steps to implementing the modified MBMD-FDK Algorithm:

(1) Input Projection data $R_\beta(m,n)$

(2) Input SDD, SAD and desired reconstruction grid (x,y,z)

(3) for all projection angles β_k, do

(4) $\tilde{R}_\beta(m,n) = R_\beta(m,n)\times\frac{SDD}{\sqrt{SDD^2+m^2+n^2}}$ % rescaling

where m, n = [-12.8:0.1:12.8];

(5) for all detector rows m do

(6) $Q_\beta(m,n) = \tilde{R}_\beta(m,n) * h(m)$ % filtering

where $h(m) = \int_{-W}^{W} |\omega| e^{j\omega m} d\omega$

(7) end for

(8) for all reconstruction voxels (x_p, y_q, z_r) do

(9) if $\beta_k = \beta_m$, then

$$\Theta = -\vartheta_e;\ \Psi = -\delta_e;\ \Omega = -\alpha_e;$$

$$T_x = -t_{xe};\ T_y = -t_{ye};\ T_z = -t_{ze};$$

Else

$$\Theta = 0;\ \Psi = 0;\ \Omega = 0;$$

$$T_x = 0;\ T_y = 0;\ T_z = 0;$$

End

(10)
$$\begin{bmatrix} x_p \\ y_q \\ z_r \end{bmatrix} = \begin{bmatrix} T_{11} & T_{12} & T_{13} \\ T_{21} & T_{22} & T_{23} \\ T_{31} & T_{32} & T_{33} \end{bmatrix} \begin{bmatrix} x_p - T_x \\ y_q - T_y \\ z_r - T_z \end{bmatrix}$$

(11) for all reconstruction voxels (x_p, y_q, z_r) do

(12) $U \leftarrow SAD + x_p \sin\beta_k - y_q \cos\beta_k$ % Backprojection stage

(13) $p' = (SAD/U)(x_p \cos\beta_k + y_q \sin\beta_k)$

(14) $\zeta = (SAD/U) z_r$

(15) $f(x_p, y_q, z_r) = f(x_p, y_q, z_r) + (SAD^2/U^2)\, Q_\beta(p', \zeta)$

(16) end for

(17) end for

Table 6.2 Estimated Marker Coordinates (Axial Motion Case)

Actual Marker Position (cm) (before motion)			Axial Motion (mm)	Actual Marker position (cm) (after motion)			Estimated marker Position (cm) (after motion)		
x_i	y_i	z_i	t_x	X_I	Y_I	Z_I	x_i'	y_i'	z_i'
0	0	9.25	-6	**-0.6**	0	9.25	**-0.59808**	0.00000	9.25001
7.25	0	3.25		**6.65**	0	3.25	**6.65190**	0.00000	3.25000
0	-7.25	-3.25		**-0.6**	-7.25	-3.25	**-0.59809**	-7.25001	-3.25000
-0.75	0.75	-9.25		**-1.35**	0.75	-9.25	**-1.34808**	0.75000	-9.25001
			-5	**-0.5**	0	9.25	**-0.49559**	0.00000	9.25003
				6.75	0	3.25	**6.75446**	0.00000	3.25001
				-0.5	-7.25	-3.25	**-0.49556**	-7.25002	-3.25001
				-1.25	0.75	-9.25	**-1.24555**	0.75000	-9.25003
			-4	**-0.4**	0	9.25	**-0.39872**	0.00000	9.25001
				6.85	0	3.25	**6.85126**	0.00000	3.25000
				-0.4	-7.25	-3.25	**-0.39874**	-7.25001	-3.25000
				-1.15	0.75	-9.25	**-1.14873**	0.75000	-9.25001
			-3	**-0.3**	0	9.25	**-0.29874**	0.00000	9.25001
				6.95	0	3.25	**6.95126**	0.00000	3.25000
				-0.3	-7.25	-3.25	**-0.29874**	-7.25001	-3.25000
				-1.05	0.75	-9.25	**-1.04872**	0.75000	-9.25001
			-2	**-0.2**	0	9.25	**-0.20127**	0.00000	9.24999
				7.05	0	3.25	**7.04873**	0.00000	3.25000
				-0.2	-7.25	-3.25	**-0.20125**	-7.24999	-3.25000
				-0.95	0.75	-9.25	**-0.95125**	0.75000	-9.24999
			-1	**-0.1**	0	9.25	**-0.09874**	0.00000	9.25001
				7.15	0	3.25	**7.15129**	0.00000	3.25000
				-0.1	-7.25	-3.25	**-0.09871**	-7.25001	-3.25000
				-0.85	0.75	-9.25	**-0.84871**	0.75000	-9.25001

Table 6.3 Estimated Marker Coordinates (Axial Motion Case)

Actual Marker Position (cm) (before motion)			Axial Motion (mm)	Actual Marker position (cm) (after motion)			Estimated marker Position (cm) (after motion)		
x_i	y_i	z_i	t_x	X_I	Y_I	Z_I	x_i'	y_i'	z_i'
0	0	9.25	6	**0.6**	0	9.25	**0.59150**	0.00000	9.24995
				7.85	0	3.25	**7.84148**	0.00000	3.24998
				0.6	-7.25	-3.25	**0.59147**	-7.24996	-3.24998
				-0.15	0.75	-9.25	**-0.15850**	0.75000	-9.24995
			5	**0.5**	0	9.25	**0.50700**	0.00000	9.25004
				7.75	0	3.25	**7.75696**	0.00000	3.25001
				0.5	-7.25	-3.25	**0.50701**	-7.25003	-3.25001
				-0.25	0.75	-9.25	**-0.24300**	0.75000	-9.25004
7.25	0	3.25	4	**0.4**	0	9.25	**0.39875**	0.00000	9.24999
				7.65	0	3.25	**7.64874**	0.00000	3.25000
				0.4	-7.25	-3.25	**0.39874**	-7.24999	-3.25000
				-0.35	0.75	-9.25	**-0.35122**	0.75000	-9.24999
0	-7.25	-3.25	3	**0.3**	0	9.25	**0.29877**	0.00000	9.24999
				7.55	0	3.25	**7.54876**	0.00000	3.25000
				0.3	-7.25	-3.25	**0.29874**	-7.24999	-3.25000
				-0.45	0.75	-9.25	**-0.45126**	0.75000	-9.24999
-0.75	0.75	-9.25	2	**0.2**	0	9.25	**0.20130**	0.00000	9.25001
				7.45	0	3.25	**7.45127**	0.00000	3.25000
				0.2	-7.25	-3.25	**0.20129**	-7.25001	-3.25000
				-0.55	0.75	-9.25	**-0.54870**	0.75000	-9.25001
			1	**0.1**	0	9.25	**0.09876**	0.00000	9.24999
				7.35	0	3.25	**7.34873**	0.00000	3.25000
				0.1	-7.25	-3.25	**0.09874**	-7.24999	-3.25000
				-0.65	0.75	-9.25	**-0.65124**	0.75000	-9.24999

Table 6.4 Estimated Motion Parameters (Axial Motion Case)

Given Axial Motion (mm)	Axial t_{xe}(cm)	Lateral t_{ye} (cm)	Vertical t_{ze} (cm)	Pitch ϑ_e°	Roll δ_e°	Yaw α_e°
-6	**-0.59808381**	2.58862E-09	-3.7874E-09	-4.63507E-07	-1.32697E-08	-2.23768E-07
-5	**-0.49556849**	1.50581E-09	-8.8952E-08	8.75995E-07	-7.71905E-09	-5.19083E-07
-4	**-0.39872641**	4.1617E-09	-1.0906E-09	-2.60193E-07	-2.13336E-08	-3.18017E-07
-3	**-0.29873347**	4.35316E-09	-6.0536E-08	3.60055E-07	-2.23151E-08	-6.04267E-07
-2	**-0.20126088**	-4.75574E-10	-5.8733E-08	4.87029E-07	2.43788E-09	-2.38755E-07
-1	**-0.09872502**	-3.14205E-11	-6.1072E-08	6.25583E-07	1.61067E-10	-2.77856E-07
6	**0.591496241**	5.09661E-09	1.46226E-08	2.5541E-07	-2.61262E-08	-2.9039E-07
5	**0.506999841**	-2.87606E-10	-1.594E-08	-1.01974E-06	1.47432E-09	-9.36362E-08
4	**0.398761345**	7.42697E-09	-8.2663E-08	3.27032E-07	-3.8072E-08	-9.39034E-07
3	**0.298754976**	4.49109E-10	6.25522E-08	-3.75788E-07	-2.30221E-09	2.63477E-07
2	**0.20129369**	5.43885E-10	-4.8217E-09	-5.23533E-07	-2.78805E-09	-8.18749E-08
1	**0.09875782**	4.86614E-09	1.7771E-09	-3.27031E-07	-2.49447E-08	-3.57548E-07

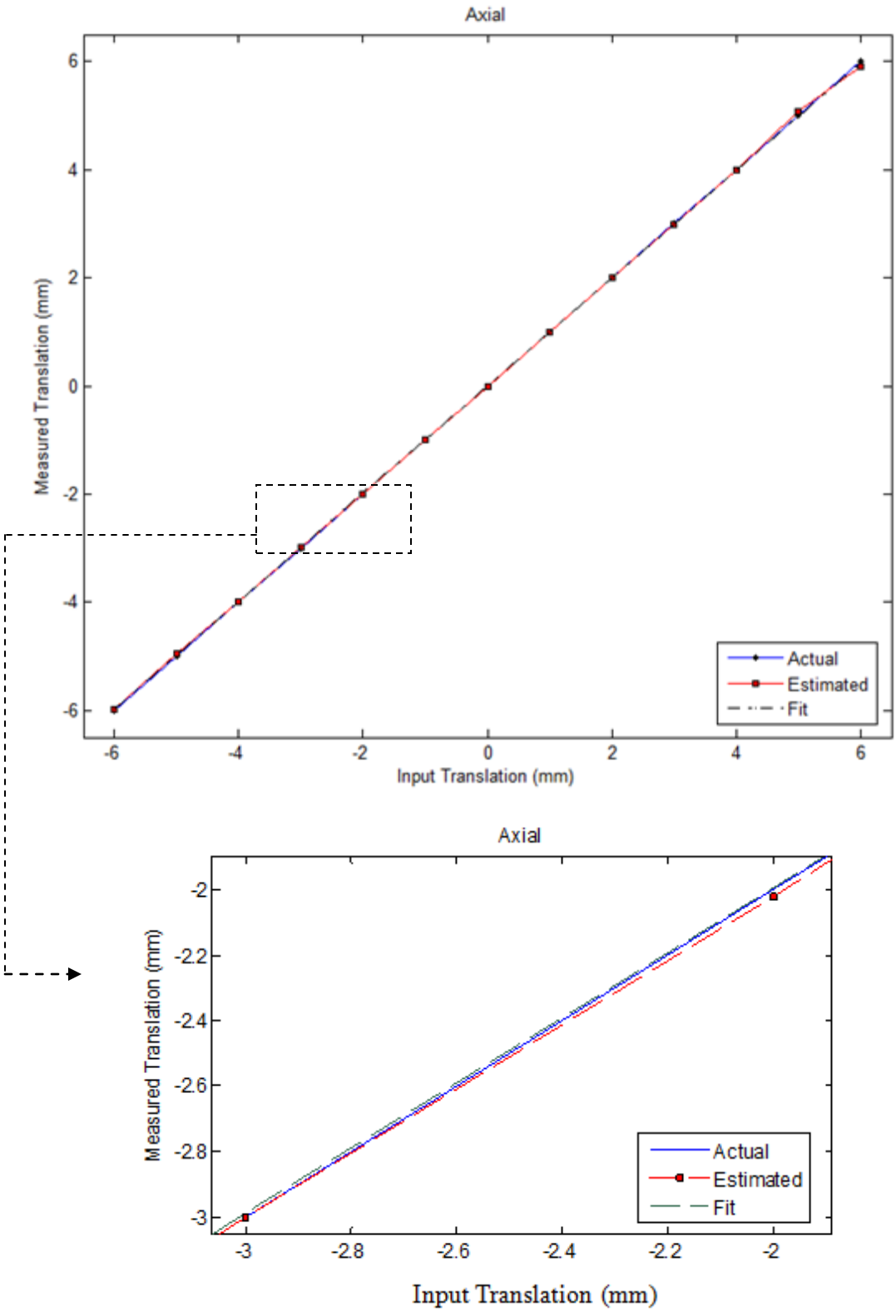

Figure 6.4 Linearity and Accuracy of the MBMD System (Axial Parameter)

Table 6.5 Estimated Marker Coordinates (Lateral Motion Case)

Actual Marker Position (cm) (before motion)			Lateral Motion (mm)	Actual Marker position (cm) (after motion)			Estimated marker Position (cm) (after motion)		
x_i	y_i	z_i	t_y	X_I	Y_I	Z_I	x_i'	y_i'	z_i'
0	0	9.25	-6	0	**-0.6**	9.25	0.00664527	**-0.6000025**	9.2500384
7.25	0	3.25		7.25	**-0.6**	3.25	7.25664500	**-0.6000025**	3.2500134
0	-7.25	-3.25		0	**-7.85**	-3.25	0.00664562	**-7.8500326**	-3.2500135
-0.75	0.75	-9.25		-0.75	**0.15**	-9.25	-0.74324281	**0.1500006**	-9.2500391
			-5	0	**-0.5**	9.25	0.00569641	**-0.5000018**	9.2500329
				7.25	**-0.5**	3.25	7.25569544	**-0.5000018**	3.2500115
				0	**-7.75**	-3.25	0.00569644	**-7.7500276**	-3.2500116
				-0.75	**0.25**	-9.25	-0.74414737	**0.2500009**	-9.2500339
			-4	0	**-0.4**	9.25	0.00474783	**-0.4000012**	9.2500274
				7.25	**-0.4**	3.25	7.25474467	**-0.4000012**	3.2500096
				0	**-7.65**	-3.25	0.00474681	**-7.6500227**	-3.2500096
				-0.75	**0.35**	-9.25	-0.74507812	**0.3500011**	-9.2500285
			-3	0	**-0.3**	9.25	0.00379654	**-0.3000007**	9.2500219
				7.25	**-0.3**	3.25	7.25379143	**-0.3000007**	3.2500077
				0	**-7.55**	-3.25	0.00379749	**-7.5500179**	-3.2500077
				-0.75	**0.45**	-9.25	-0.74603666	**0.4500011**	-9.2500229
			-2	0	**-0.2**	9.25	0.00284568	**-0.2000004**	9.2500165
				7.25	**-0.2**	3.25	7.25284556	**-0.2000004**	3.2500058
				0	**-7.45**	-3.25	0.00284841	**-7.4500133**	-3.2500058
				-0.75	**0.55**	-9.25	-0.74702334	**0.5500010**	-9.2500172
			-1	0	**-0.1**	9.25	0.00125957	**-0.1000001**	9.2500073
				7.25	**-0.1**	3.25	7.25125960	**-0.1000001**	3.2500025
				0	**-7.35**	-3.25	0.00126638	**-7.3500058**	-3.2500026
				-0.75	**0.65**	-9.25	-0.74865440	**0.6500005**	-9.2500078

Table 6.6 Estimated Marker Coordinates (Lateral Motion Case)

Actual Marker Position (cm) (before motion)			Lateral Motion (mm)	Actual Marker position (cm) (after motion)			Estimated marker Position (cm) (after motion)		
x_i	y_i	z_i	t_y	X_I	Y_I	Z_I	x_i'	y_i'	z_i'
			6	0	**0.6**	9.25	-0.00664587	**0.5999975**	9.2499616
				7.25	**0.6**	3.25	7.24335386	**0.5999975**	3.2499866
				0	**-6.65**	-3.25	-0.00608858	**-6.6499747**	-3.2499876
				-0.75	**1.35**	-9.25	-0.75664634	**1.3499944**	-9.2499616
			5	0	**0.5**	9.25	-0.00569599	**0.4999982**	9.2499671
				7.25	**0.5**	3.25	7.24430304	**0.4999982**	3.2499885
				0	**-6.75**	-3.25	-0.00527493	**-6.7499777**	-3.2499893
				-0.75	**1.25**	-9.25	-0.75569633	**1.2499955**	-9.2499671
			4	0	**0.4**	9.25	-0.00474584	**0.3999988**	9.2499726
				7.25	**0.4**	3.25	7.24525100	**0.3999988**	3.2499904
0	0	9.25		0	**-6.85**	-3.25	-0.00448628	**-6.8499808**	-3.2499909
7.25	**0**	**3.25**		-0.75	**1.15**	-9.25	-0.75474779	**1.1499966**	-9.2499725
0	-7.25	-3.25	3	0	**0.3**	9.25	-0.00379840	**0.2999993**	9.2499780
-0.75	0.75	-9.25		7.25	**0.3**	3.25	7.24619649	**0.2999993**	3.2499923
				0	**-6.95**	-3.25	-0.00372285	**-6.9499838**	-3.2499924
				-0.75	**1.05**	-9.25	-0.75379747	**1.0499975**	-9.2499780
			2	0	**0.2**	9.25	-0.00474925	**0.1999994**	9.2499725
				7.25	**0.2**	3.25	7.24525062	**0.1999994**	3.2499904
				0	**-7.05**	-3.25	-0.00488280	**-7.0499785**	-3.2499901
				-0.75	**0.95**	-9.25	-0.75474824	**0.9499972**	-9.2499725
			1	0	**0.1**	9.25	0.00315831	**0.1000002**	9.2500183
				7.25	**0.1**	3.25	7.25315834	**0.1000002**	3.2500064
				0	**-7.15**	-3.25	0.00279218	**-7.1500125**	-3.2500057
				-0.75	**0.85**	-9.25	-0.74684341	**0.8500017**	-9.2500183

Table 6.7 Estimated Motion Parameters (Lateral Motion Case)

Given Lateral Motion (mm)	Axial t_{xe}(cm)	Lateral t_{ye} (cm)	Vertical t_{ze} (cm)	Pitch $\vartheta_e°$	Roll $\delta_e°$	Yaw $\alpha_e°$
-6	0.00669598	**-0.60000249**	-3.04397E-07	1.07486E-06	6.22655E-08	-3.24516E-06
-5	0.00576715	**-0.50000177**	-4.18952E-07	1.71963E-06	6.1829E-09	-4.47379E-06
-4	0.00482650	**-0.40000117**	-4.64223E-07	1.9854E-06	-4.3721E-08	-4.974E-06
-3	0.00387192	**-0.30000069**	-4.44041E-07	1.91972E-06	-7.7192E-08	-4.7268E-06
-2	0.00290515	**-0.20000034**	-3.48249E-07	1.57706E-06	-9.0221E-08	-3.67536E-06
-1	0.00129887	**-0.10000006**	-2.28192E-07	1.07899E-06	-7.1551E-08	-2.32773E-06
6	-0.00661998	**0.59999740**	-4.08315E-08	6.86196E-07	6.4897E-07	8.51E-06
5	-0.00567645	**0.49999814**	-2.98539E-08	5.4997E-07	4.91516E-07	6.44043E-06
4	-0.00473471	**0.39999876**	-1.20386E-08	3.54856E-07	3.08976E-07	4.03812E-06
3	-0.00379468	**0.29999927**	-3.82349E-09	2.13036E-07	9.74686E-08	1.17204E-06
2	-0.00475506	**0.19999943**	1.79282E-08	2.49929E-07	-1.1933E-07	-1.95237E-06
1	0.00314037	**0.10000027**	3.4115E-08	-4.03127E-07	-3.9966E-07	-5.51292E-06

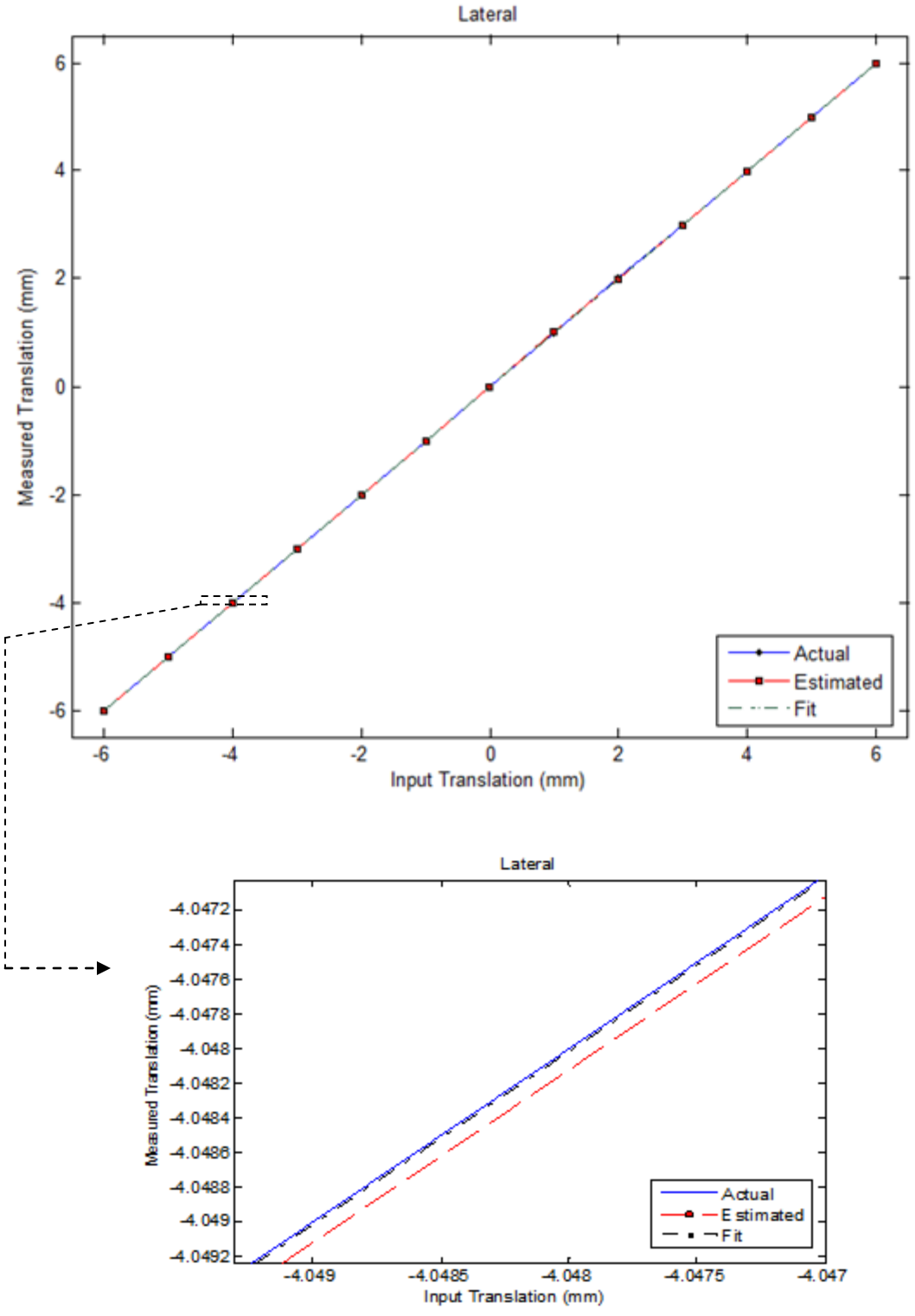

Figure 6.5 Linearity and Accuracy of the MBMD System (Lateral Parameter)

Table 6.8 Estimated Marker Coordinates (Vertical Motion Case)

Actual Marker Position (cm) (before motion)			Vertical Motion (mm)	Actual Marker position (cm) (after motion)			Estimated marker Position (cm) (after motion)		
x_i	y_i	z_i	t_z	X_I	Y_I	Z_I	x_i'	y_i'	z_i'
0	0	9.25	-6	0	0	**8.65**	0.0087025	0	**8.650047048**
				7.25	0	**2.65**	7.2586242	0	**2.650014219**
				0	-7.25	**-3.85**	0.0066457	-7.2500301	**-3.85001599**
				-0.75	0.75	**-9.85**	-0.741139	0.75000416	**-9.85005457**
			-5	0	0	**8.75**	0.0035699	0	**8.750019523**
				7.25	0	**2.75**	7.2536099	0	**2.750006177**
				0	-7.25	**-3.75**	0.0018987	-7.2500086	**-3.75000445**
				-0.75	0.75	**-9.75**	-0.746203	0.75000178	**-9.75002315**
7.25	0	3.25	-4	0	0	**8.85**	0.0060072	0	**8.850033227**
				7.25	0	**2.85**	7.2561655	0	**2.850010933**
				0	-7.25	**-3.65**	0.0047469	-7.2500215	**-3.65001083**
				-0.75	0.75	**-9.65**	-0.743671	0.75000297	**-9.65003819**
0	-7.25	-3.25	-3	0	0	**8.95**	0.0046221	0	**8.950025855**
				7.25	0	**2.95**	7.2548982	0	**2.95000899**
				0	-7.25	**-3.55**	0.0037976	-7.2500172	**-3.55000843**
				-0.75	0.75	**-9.55**	-0.744937	0.75000237	**-9.55003024**
-0.75	0.75	-9.25	-2	0	0	**9.05**	-0.000586	0	**9.049996688**
				7.25	0	**3.05**	7.2498093	0	**3.049999638**
				0	-7.25	**-3.45**	-0.00095	-7.2499957	**-3.44999795**
				-0.75	0.75	**-9.45**	-0.75	0.75	**-9.4500000**
			-1	0	0	**9.15**	-0.000755	0	**9.149995684**
				7.25	0	**3.15**	7.249758	0	**3.149999526**
				0	-7.25	**-3.35**	-0.000634	-7.2499971	**-3.34999867**
				-0.75	0.75	**-9.35**	-0.750001	0.75	**-9.3500000**

Table 6.9 Estimated Marker Coordinates (Vertical Motion Case)

Actual Marker Position (cm) (before motion)			Vertical Motion (mm)	Actual Marker position (cm) (after motion)			Estimated marker Position (cm) (after motion)		
x_i	y_i	z_i	t_z	X_I	Y_I	Z_I	x_i'	y_i'	z_i'
0	0	9.25	6	0	0	**9.85**	0.0066456	0	**9.8500409**
7.25	0	3.25		7.25	0	**3.85**	7.2566454	0	**3.8500159**
0	-7.25	-3.25		0	-7.25	**-2.65**	0.0086328	-7.2500391	**-2.6500143**
-0.75	0.75	-9.25		-0.75	0.75	**-8.65**	-0.74351	0.75000304	**-8.6500351**
			5	0	0	**9.75**	-0.013291	0	**9.7499190**
				7.25	0	**3.75**	7.236709	0	**3.7499690**
				0	-7.25	**-2.75**	-0.011573	-7.2499476	**-2.7499801**
				-0.75	0.75	**-8.75**	-0.763516	0.74999366	**-8.7499260**
			4	0	0	**9.65**	-0.011076	0	**9.6499332**
				7.25	0	**3.65**	7.2389236	0	**3.6499748**
				0	-7.25	**-2.85**	-0.009651	-7.2499563	**-2.8499828**
				-0.75	0.75	**-8.85**	-0.761396	0.74999466	**-8.8499369**
			3	0	0	**9.55**	-0.008861	0	**9.5499471**
				7.25	0	**3.55**	7.2411391	0	**3.5499804**
				0	-7.25	**-2.95**	-0.007755	-7.2499649	**-2.9499857**
				-0.75	0.75	**-8.95**	-0.7593	0.74999564	**-8.9499480**
			2	0	0	**9.45**	-0.002848	0	**9.4499832**
				7.25	0	**3.45**	7.2471521	0	**3.4499939**
				0	-7.25	**-3.05**	-0.002085	-7.2499906	**-3.0499960**
				-0.75	0.75	**-9.05**	-0.752483	0.74999884	**-9.0499859**
			1	0	0	**9.35**	-0.000634	0	**9.3499963**
				7.25	0	**3.35**	7.2493672	0	**3.3499987**
				0	-7.25	**-3.15**	-0.000241	-7.2499989	**-3.1499995**
				-0.75	0.75	**-9.15**	-0.750754	0.74999965	**-9.1499957**

Table 6.10 Estimated Motion Parameters (Vertical Motion Case)

Given Vertical Motion (mm)	Axial t_{xe}(cm)	Lateral t_{ye} (cm)	Vertical t_{ze} (cm)	Pitch $\vartheta_e°$	Roll $\delta_e°$	Yaw $\alpha_e°$
-6	0.008674149	4.71383E-07	**-0.600003494**	-3.5308E-07	-2.4164E-06	-4.15726E-05
-5	0.003596574	4.03674E-07	**-0.500001563**	2.61698E-06	-2.06931E-06	-3.57355E-05
-4	0.006101358	3.36671E-07	**-0.400002244**	5.64098E-06	-1.72584E-06	-3.06449E-05
-3	0.004796282	2.69339E-07	**-0.300001959**	9.29949E-06	-1.38068E-06	-2.61185E-05
-2	-0.00031863	2.01818E-07	**-0.200001423**	1.36294E-05	-1.03455E-06	-2.21824E-05
-1	-0.00038334	1.34553E-07	**-0.100001914**	1.80481E-05	-6.89745E-07	-1.89498E-05
6	0.006668354	-4.54436E-07	**0.600002707**	-1.6765E-06	2.32952E-06	2.83105E-05
5	-0.0133126	-4.14161E-07	**0.499996288**	-1.1474E-06	2.12307E-06	2.80568E-05
4	-0.01115406	-3.71701E-07	**0.399997933**	-2.707E-06	1.90541E-06	2.75493E-05
3	-0.00900823	-3.2917E-07	**0.299999372**	-4.596E-06	1.68739E-06	2.71518E-05
2	-0.00264712	-8.49088E-08	**0.199998645**	5.34402E-06	4.35258E-07	8.3335E-07
1	-0.0006696	-1.08884E-07	**0.100000237**	-1.3594E-06	5.5816E-07	9.05445E-06

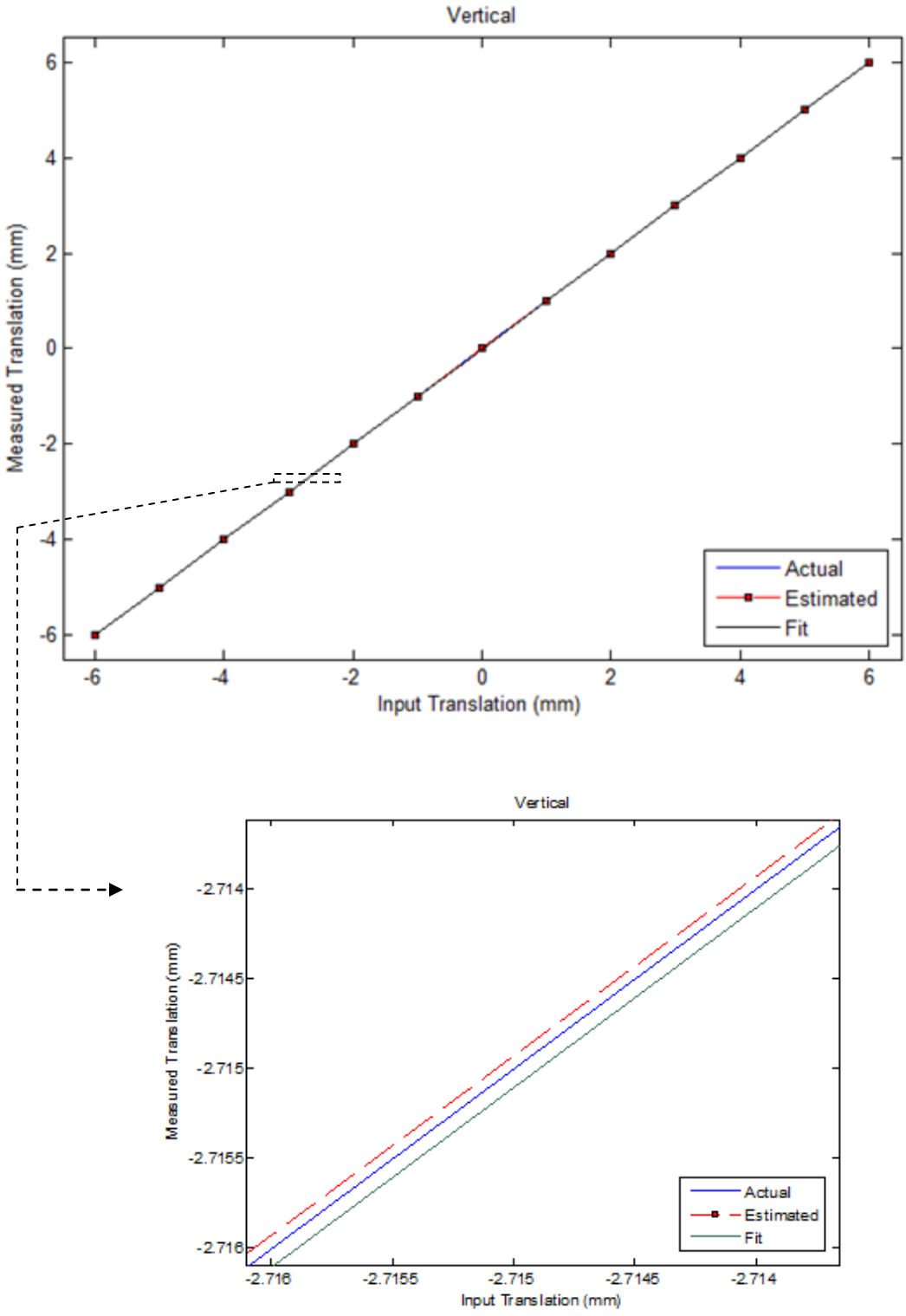

Figure 6.6 Linearity and Accuracy of the MBMD System (Vertical Parameter)

Table 6.11 Estimated Marker Coordinates (Roll Motion Case)

Actual Marker Position (cm) (before motion)			Roll Motion (deg)	Actual Marker position (cm) (after motion)			Estimated marker Position (cm) (after motion)		
x_i	y_i	z_i	$\delta_e°$	X_I	Y_I	Z_I	x_i'	y_i'	z_i'
			5	0	3.980335	8.349816	-0.11392	3.980052	8.349222
				7.25	1.398496	2.933719	7.136071	1.398397	2.933511
				0	-7.94295	0.186003	-0.11392	-7.94238	0.18599
				-0.75	-3.30332	-8.67255	-0.86392	-3.30309	-8.67193
			4	0	4.125453	8.279078	-0.11393	4.12516	8.278489
				7.25	1.449484	2.908865	7.13608	1.449381	2.908659
				0	-7.93849	0.324598	-0.11393	-7.93793	0.324575
				-0.75	-3.45418	-8.61357	-0.86392	-3.45393	-8.61296
0	4.6929	7.9711	3	0	4.269315	8.205818	-0.11393	4.269011	8.205234
7.2500	1.6489	2.8007		7.25	1.50003	2.883125	7.136067	1.499923	2.882921
0	-7.8965	0.8776		0	-7.93162	0.463095	-0.11392	-7.93105	0.463062
-0.7500	-4.0466	-8.3516		-0.75	-3.60398	-8.55198	-0.86392	-3.60372	-8.55137
			2	0	4.411876	8.130058	-0.11392	4.411562	8.12948
				7.25	1.550119	2.856507	7.136072	1.550009	2.856305
				0	-7.92233	0.60145	-0.11392	-7.92176	0.601407
				-0.75	-3.75268	-8.48778	-0.86392	-3.75241	-8.48717
			1	0	4.553093	8.051822	-0.11393	4.552769	8.051249
				7.25	1.599735	2.829019	7.136075	1.599622	2.828818
				0	-7.91062	0.739622	-0.1139	-7.91006	0.739569
				-0.75	-3.90024	-8.42099	-0.86393	-3.89996	-8.42039

Table 6.12 Estimated Marker Coordinate (Roll Motion Case)

Actual Marker Position (cm) (before motion)			Roll Motion (deg)	Actual Marker position (cm) (after motion)			Estimated marker Position (cm) (after motion)		
x_i	y_i	z_i	$\delta_e°$	X_I	Y_I	Z_I	x_i'	y_i'	z_i'
0	**4.6929**	**7.9711**	-1	0	4.831324	7.888017	-0.11391	4.83098	7.887455
7.2500	1.6489	2.8007		7.25	1.697492	2.771465	7.136075	1.697372	2.771269
0	-7.8965	0.8776		0	-7.87999	1.015248	-0.11393	-7.87943	1.015176
-0.7500	-4.0466	-8.3516		-0.75	-4.19176	-8.27975	-0.86393	-4.19146	-8.27916
			-2	0	4.968253	7.802497	-0.11392	4.967899	7.801942
				7.25	1.745602	2.741418	7.136091	1.745479	2.741224
				0	-7.86107	1.152618	-0.11395	-7.86051	1.152536
				-0.75	-4.33562	-8.20533	-0.86391	-4.33531	-8.20474
			-3	0	5.103669	7.714601	-0.11392	5.103305	7.714051
				7.25	1.793181	2.710535	7.136067	1.793054	2.710343
				0	-7.83976	1.289637	-0.11392	-7.8392	1.289546
				-0.75	-4.47816	-8.12841	-0.86392	-4.47784	-8.12783
			-4	0	5.23753	7.624355	-0.11392	5.237157	7.623812
				7.25	1.840213	2.678827	7.13606	1.840083	2.678637
				0	-7.81606	1.426264	-0.11393	-7.8155	1.426162
				-0.75	-4.61934	-8.04902	-0.86392	-4.61901	-8.04845
			-5	0	5.369795	7.531786	-0.11392	5.369413	7.53125
				7.25	1.886685	2.646303	7.136051	1.886551	2.646115
				0	-7.78998	1.562455	-0.11393	-7.78942	1.562344
				-0.75	-4.75911	-7.96717	-0.86392	-4.75877	-7.96661

Table 6.13 Estimated Motion Parameters (Roll Motion Case)

Given Roll Motion (deg)	Axial t_{xe}(cm)	Lateral t_{ye} (cm)	Vertical t_{ze} (cm)	Pitch ϑ_e°	Roll δ_e°	Yaw α_e°
5	-0.113923475	7.2089E-08	1.771E-07	-6.4488E-06	**4.999644164**	3.137E-06
4	-0.113923502	6.864E-08	1.601E-07	-6.6546E-06	**3.999715694**	3.373E-06
3	-0.113922969	7.0952E-08	1.59E-07	-6.3901E-06	**2.999787158**	3.385E-06
2	-0.113922041	7.9016E-08	1.678E-07	-6.3088E-06	**1.999858563**	3.485E-06
1	-0.113930432	7.631E-08	1.714E-07	-6.4019E-06	**0.999929726**	3.726E-06
-1	-0.11392306	1.1526E-07	2.108E-07	-5.7883E-06	**-0.999927445**	3.616E-06
-2	-0.113918851	8.4008E-08	1.388E-07	-6.4413E-06	**-1.999856576**	4.124E-06
-3	-0.113922115	8.6815E-08	1.494E-07	-5.9988E-06	**-2.999785288**	4.03E-06
-4	-0.113923232	9.2453E-08	1.527E-07	-5.8057E-06	**-3.999713789**	4.052E-06
-5	-0.113925127	1.0258E-07	1.629E-07	-5.5398E-06	**-4.999642071**	4.019E-06

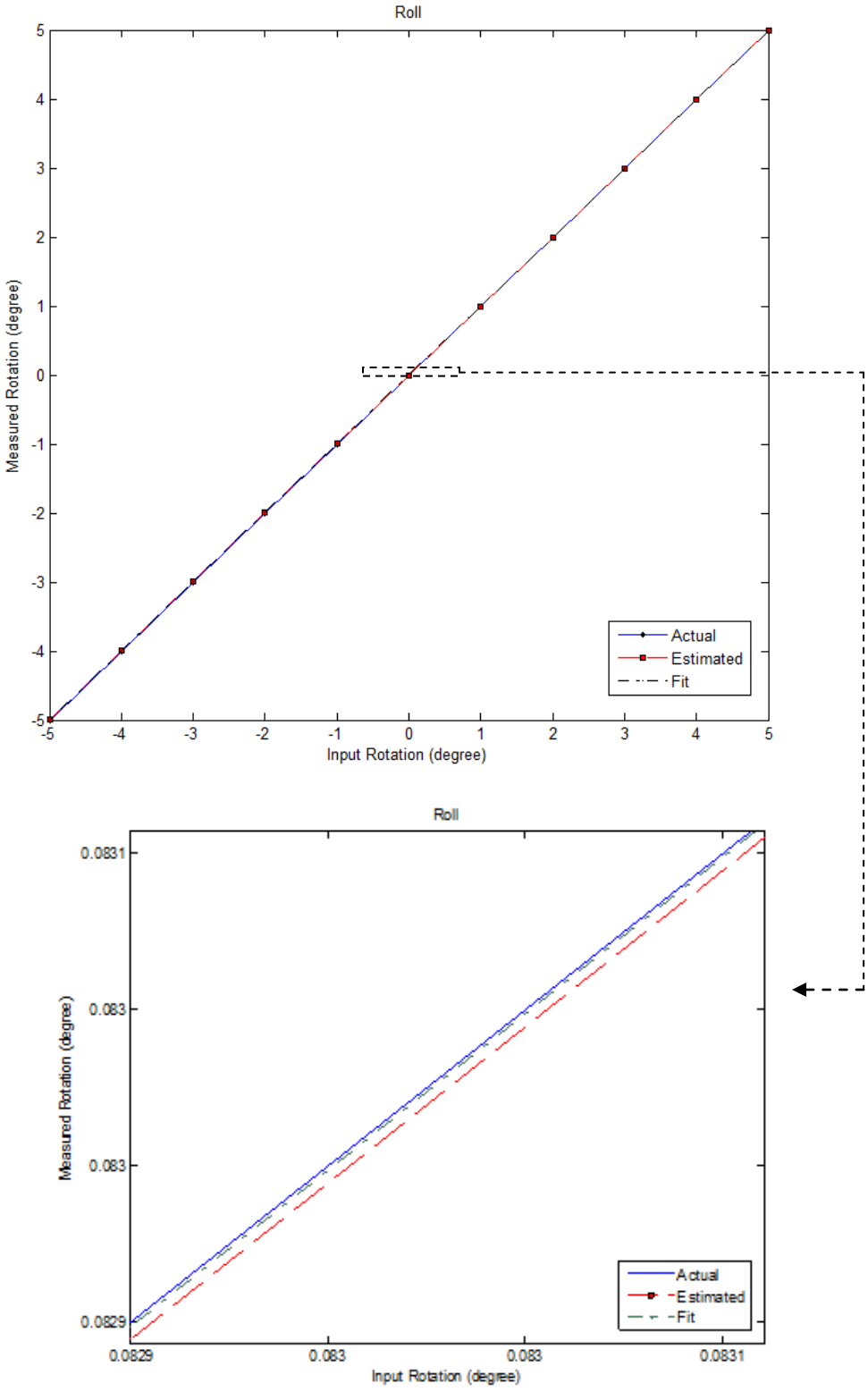

Figure 6.7 Linearity and Accuracy of the MBMD System (Roll Parameter)

Table 6.14 Estimated Marker Coordinates (Pitch Motion Case)

Actual Marker Position (cm) (before motion)			Pitch Motion (deg)	Actual Marker position (cm) (after motion)			Estimated marker Position (cm) (after motion)		
x_i	y_i	z_i	$\vartheta_e°$	X_I	Y_I	Z_I	x_i'	y_i'	z_i'
-4.6929	0	7.9711	5	-3.98034	0	8.349816	-4.06128	0	8.34939276
4.5988	0	6.4789		5.145954	0	6.053441	5.06403	0	6.05313251
1.6489	-7.2500	-2.8007		1.398496	-7.25	-2.93372	1.318484	-7.2496	-2.9335726
4.0466	.7500	-8.3516		3.303323	0.75	-8.67255	3.222564	0.74996	-8.6721093
			4	-4.12545	0	8.279078	-4.22077	0	8.27858359
				5.039523	0	6.142329	4.946939	0	6.14197448
				1.449484	-7.25	-2.90887	1.356458	-7.2496	-2.9086963
				3.454177	0.75	-8.61357	3.360539	0.74996	-8.6130713
			3	-4.26931	0	8.205818	-4.34735	0	8.20541674
				4.931558	0	6.229345	4.852626	0	6.22903873
				1.50003	-7.25	-2.88313	1.419751	-7.2496	-2.8829807
				3.603978	0.75	-8.55198	3.525096	0.74996	-8.551558
			2	-4.41188	0	8.130058	-4.4309	0	8.12996151
				4.822089	0	6.314464	4.803878	0	6.31439223
				1.550119	-7.25	-2.85651	1.53114	-7.2499	-2.8564732
				3.752682	0.75	-8.48778	3.732692	0.74999	-8.4876723
			1	-4.55309	0	8.051822	-4.61064	0	8.05153189
				4.711152	0	6.397659	4.65133	0	6.39742072
				1.599735	-7.25	-2.82902	1.541262	-7.2497	-2.8289154
				3.900243	0.75	-8.42099	3.844083	0.74997	-8.4206972

Table 6.15 Estimated Marker Coordinate (Pitch Motion Case)

Actual Marker Position (cm) (before motion)			Pitch Motion (deg)	Actual Marker position (cm) (after motion)			Estimated marker Position (cm) (after motion)		
x_i	y_i	z_i	δ_e°	X_I	Y_I	Z_I	x_i'	y_i'	z_i'
-4.6929	0	7.9711	-1	-4.83132	0	7.888017	-4.92628	0	7.88754715
4.5988	0	6.4789		4.485007	0	6.558179	4.38992	0	6.55779013
1.6489	-7.2500	-2.8007		1.697492	-7.25	-2.77147	1.604651	-7.2496	-2.7713047
4.0466	.7500	-8.3516		4.191755	0.75	-8.27975	4.097999	0.74996	-8.2792618
			-2	-4.96825	0	7.802497	-5.04698	0	7.80211198
				4.369868	0	6.635454	4.293717	0	6.63513917
				1.745602	-7.25	-2.74142	1.66806	-7.2496	-2.7412852
				4.335618	0.75	-8.20533	4.256988	0.74996	-8.2049263
			-3	-5.10367	0	7.714601	-5.21578	0	7.71405851
				4.253398	0	6.710708	4.141818	0	6.71024147
				1.793181	-7.25	-2.71054	1.680822	-7.2495	-2.7103453
				4.478161	0.75	-8.12841	4.370419	0.74995	-8.1278659
			-4	-5.23753	0	7.624355	-5.35419	0	7.62379677
				4.135632	0	6.783918	4.017767	0	6.78341973
				1.840213	-7.25	-2.67883	1.723964	-7.2495	-2.6786329
				4.619339	0.75	-8.04902	4.50411	0.74995	-8.0484411
			-5	-5.3698	0	7.531786	-5.47488	0	7.53128945
				4.016607	0	6.855062	3.91397	0	6.85462306
				1.886685	-7.25	-2.6463	1.782297	-7.2495	-2.6461307
				4.75911	0.75	-7.96717	4.656797	0.74995	-7.9666666

Table 6.16 Estimated Motion Parameters (Pitch Motion Case)

Given Pitch Motion (deg)	Axial t_{xe}(cm)	Lateral t_{ye} (cm)	Vertical t_{ze} (cm)	Pitch $\vartheta_e°$	Roll $\delta_e°$	Yaw $\alpha_e°$
5	-0.08086169	-1.382E-07	-1.5499E-06	**4.999757176**	8.70847E-07	1.7683E-07
4	-0.09432088	-1.051E-07	-4.8268E-06	**3.999668822**	-1.38948E-05	1.343E-07
3	-0.07856771	3.1839E-07	1.19272E-06	**2.999866406**	-1.51447E-05	-4.06468E-07
2	-0.01942051	-2.088E-07	2.24834E-06	**1.999954318**	2.56401E-05	2.66348E-07
1	-0.05707001	5.0805E-07	-4.3403E-06	**1.000011001**	-5.61349E-05	-6.47809E-07
-1	-0.09432154	-1.633E-07	-4.1936E-06	**-0.999957721**	-1.04913E-05	2.08197E-07
-2	-0.07850798	-2.037E-07	-8.2751E-07	**-1.999987967**	1.17034E-05	2.59892E-07
-3	-0.11011687	1.0178E-06	-1.1355E-05	**-2.999837262**	-0.000118302	-1.29944E-06
-4	-0.11604843	2.5882E-07	-5.0668E-06	**-3.999698384**	-4.19462E-05	-3.30772E-07
-5	-0.10368088	4.7907E-07	-7.2115E-06	**-4.999768471**	-6.19245E-05	-6.13096E-07

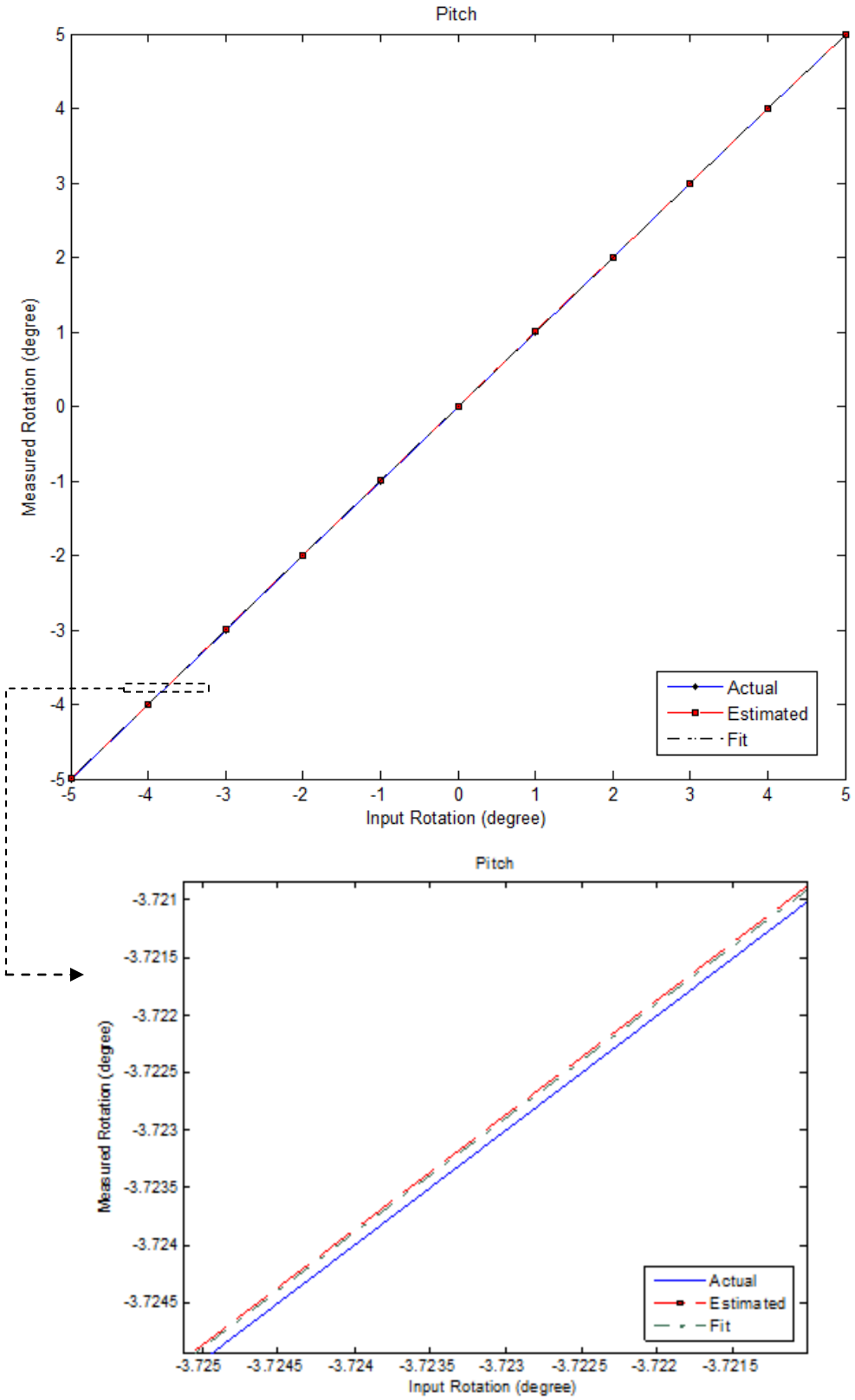

Figure 6.8 Linearity and Accuracy of the MBMD System (Pitch Parameter)

Table 6.17 Estimated Marker Coordinate (Yaw Motion Case)

Actual Marker Position (cm) (before motion)			Yaw Motion (deg)	Actual Marker position (cm) (after motion)			Estimated marker Position (cm) (after motion)		
x_i	y_i	z_i	$\alpha_e°$	X_I	Y_I	Z_I	x_i'	y_i'	z_i'
0	0	9.2500	5	0	0	9.25	-0.1060606	0	9.2493868
6.2476	-3.6782	3.2500		6.544451	-3.119722	3.25	6.4366875	-3.119513	3.249782
-3.6782	-6.2476	-3.2500		-3.11972	-6.544451	-3.25	-3.2287421	-6.5440038	-3.2497781
-0.2658	1.0268	-9.2500		-0.35428	0.999742	-9.25	-0.4627566	0.9996742	-9.2493727
			4	0	0	9.25	-0.059596	0	9.24965546
				6.489007	-3.233464	3.25	6.4282269	-3.2333412	3.24987704
				-3.23346	-6.489007	-3.25	-3.293389	-6.4887636	-3.249878
				-0.33678	1.0057728	-9.25	-0.396093	1.0057355	-9.249657
			3	0	0	9.25	-0.0151515	0	9.24991241
				6.431587	-3.34622	3.25	6.4156976	-3.3461867	3.24996785
				-3.34622	-6.431587	-3.25	-3.360055	-6.4315314	-3.2499718
				-0.31918	1.0114973	-9.25	-0.3364774	1.0114863	-9.2499
			2	0	0	9.25	-0.0818182	0	9.24952699
				6.372208	-3.457957	3.25	6.2920301	-3.4577843	3.24983778
				-3.45796	-6.372208	-3.25	-3.5378337	-6.3718892	-3.2498374
				-0.30147	1.0169136	-9.25	-0.3829675	1.0168618	-9.2495288
			1	0	0	9.25	-0.1121212	0	9.2493518
				6.310888	-3.568641	3.25	6.2006584	-3.5683957	3.24977698
				-3.56864	-6.310888	-3.25	-3.6792477	-6.3104505	-3.2497748
				-0.28368	1.0220202	-9.25	-0.3940812	1.0219496	-9.2493616

Table 6.18 Estimated Marker Coordinates (Yaw Motion Case)

Actual Marker Position (cm) (before motion)			Yaw Motion (deg)	Actual Marker position (cm) (after motion)			Estimated marker Position (cm) (after motion)		
x_i	y_i	z_i	$\alpha_e°$	X_I	Y_I	Z_I	x_i'	y_i'	z_i'
0	0	9.2500	-1	0	0	9.25	-0.1	0	9.24942188
6.2476	-3.6782	3.2500		6.1825	-3.786713	3.25	6.0809781	-3.7864741	3.24979458
-3.6782	-6.2476	-3.2500		-3.78671	-6.1825	-3.25	-3.8888466	-6.182104	-3.249792
-0.2658	1.0268	-9.2500		-0.24784	1.0312979	-9.25	-0.3506516	1.0312316	-9.2494055
			-2	0	0	9.25	0.0919192	0	9.25053141
				6.115471	-3.894036	3.25	6.2082511	-3.8942612	3.25018774
				-3.89404	-6.115471	-3.25	-3.8014742	-6.1158254	-3.2501885
				-0.2298	1.0354662	-9.25	-0.1374998	1.035526	-9.2505337
			-3	0	0	9.25	-0.0050505	0	9.2499708
				6.046579	-4.000173	3.25	6.0405739	-4.0001579	3.24998785
				-4.00017	-6.046579	-3.25	-4.0050083	-6.0465607	-3.2499902
				-0.2117	1.0393192	-9.25	-0.2153021	1.0393168	-9.2499792
			-4	0	0	9.25	-0.0393939	0	9.24977225
				5.975845	-4.105091	3.25	5.9355236	-4.1049879	3.2499184
				-4.10509	-5.975845	-3.25	-4.1438943	-5.9757001	-3.249921
				-0.19353	1.0428555	-9.25	-0.2334856	1.0428294	-9.249769
			-5	0	0	9.25	-0.0656566	0	9.24962042
				5.903292	-4.208759	3.25	5.8385544	-4.2085889	3.24986899
				-4.20876	-5.903292	-3.25	-4.2767187	-5.9030402	-3.2498616
				-0.1753	1.0460742	-9.25	-0.2405187	1.0460315	-9.2496229

Table 6.19 Estimated Motion Parameters (Yaw Motion Case)

Given Yaw Motion (deg)	Axial t_{xe}(cm)	Lateral t_{ye} (cm)	Vertical t_{ze} (cm)	Pitch $\vartheta_e°$	Roll $\delta_e°$	Yaw $\alpha_e°$
5	-0.1073729	3.349E-08	6.568E-06	3.674E-05	4.39322E-05	**4.999632368**
4	-0.0595385	2.518E-07	-7.56E-07	1.742E-05	-7.5135E-06	**3.999856623**
3	-0.0160986	-7.933E-07	5.454E-06	-6.614E-06	8.7684E-05	**3.000001165**
2	-0.081503	-4.394E-07	-7.93E-07	-4.07E-05	-8.4726E-07	**1.999896659**
1	-0.1111818	1.511E-08	-4.36E-06	-3.812E-05	-5.2825E-05	**0.999914649**
-1	-0.1014453	-2.701E-07	7.526E-06	2.746E-05	6.51809E-05	**-0.999956344**
-2	0.09216395	-9.69E-08	-1.08E-06	-1.302E-05	-4.8282E-06	**-2.000110147**
-3	-0.0044301	4.986E-07	-3.89E-06	1.514E-05	-3.5565E-05	**-2.999971054**
-4	-0.0396659	-1.608E-07	1.373E-06	5.39E-06	2.9329E-05	**-3.999880524**
-5	-0.0655246	4.132E-07	-7.73E-07	4.983E-06	-5.289E-05	**-4.999851566**

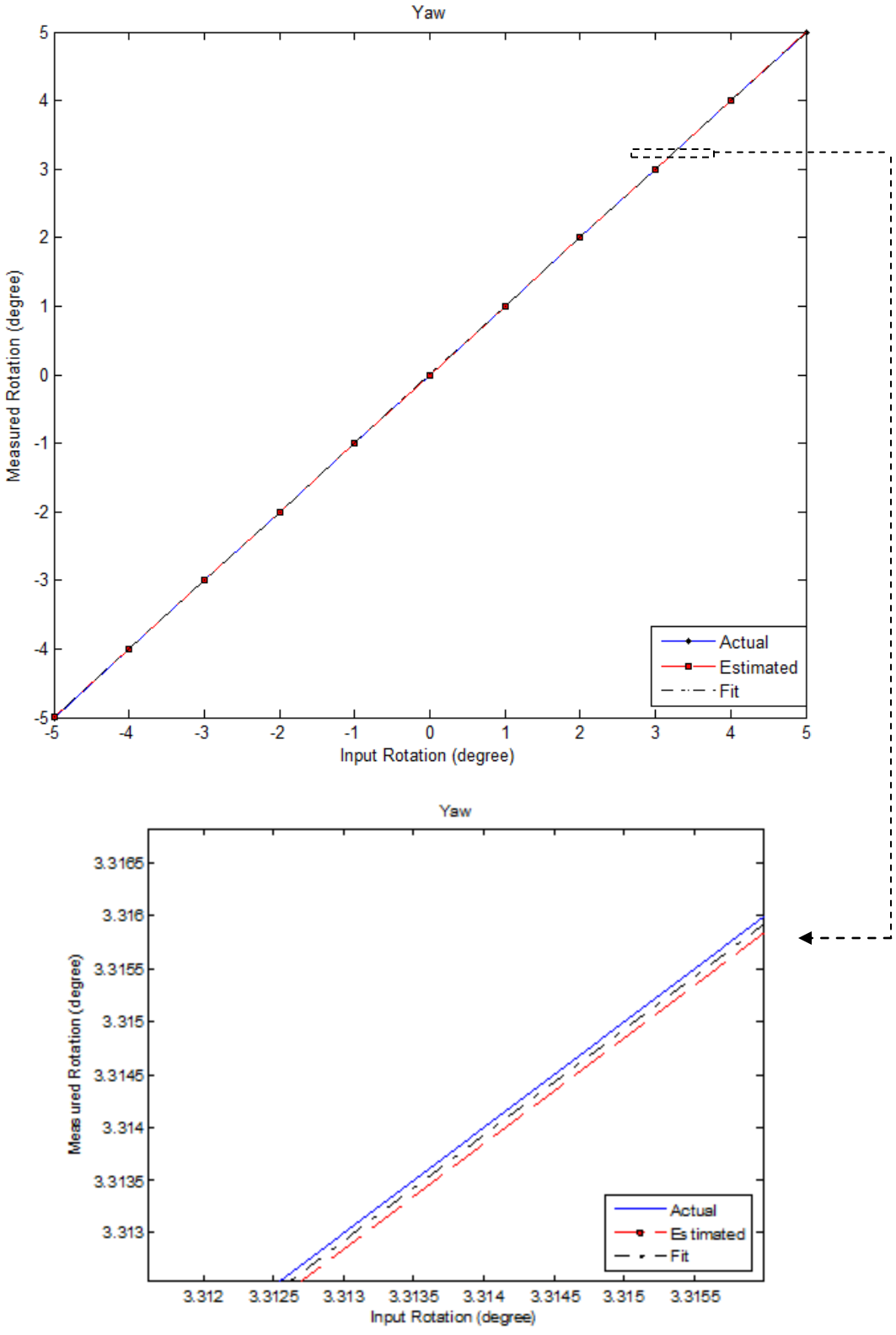

Figure 6.9 Linearity and Accuracy of the MBMD System (Yaw Parameter)

Table 6.20 Comparison of Results Showing Linearity and Accuracy

Motion	Slope		R^2	
	Goldstein	MBMD	Goldstein	MBMD
Axial	0.983±0.004	0.9999±0.00337	0.99987	0.99989
Lateral	0.993±0.003	1.0000±0.00019	0.99998	1.00000
Vertical	1.004±0.002	1.0000±0.00030	0.99987	1.00000
Roll	0.990±0.002	0.9999±0.00001	0.99996	0.99999
Pitch	0.904±0.011	1.0000±0.00005	0.99904	1.00000
Yaw	0.991±0.009	1.0000±0.00010	0.99944	0.99995

Table 6.20, presents the simulation results of the MBMD system (plotted in Figures 6.4-6.9). The results are compared with a well-known algorithm by Goldstein et al.[66] which is an external sensor based method. The MBMD system is simulated with the identical motion parameters of Goldstein's experiment. The slopes and the square correlation coefficient (R^2) are the two important statistical measures to validate the performance of an estimator. The slope of a best fit line indicates the linearity of the estimator. The square correlation coefficient (R^2) of a best fit line through the data points indicates how well the best fit line represents the real data values. MBMD slopes are much closer to unity (within four decimal points) compared to Goldstein method. The square correlation coefficient of the MBMD best fit lines through the data points are higher (within five decimal points) than the Goldstein method. Thus, from the comparisons of the slopes and the square correlation coefficient (R^2) of the best fit lines through the data points, it can be inferred that the MBMD system performs better than that of the Goldstein *et al*.

Table 6.21 Translational Motion Given to the Phantom During Scanning of Projections at 200°, 220°, and 240°

Step	*Roll*	*Pitch*	*Yaw*	t_x (cm)	t_y (cm)	t_z(cm)
200	0°	0°	0°	0.2	0	0
220	0°	0°	0°	0.2	0.4	0
240	0°	0°	0°	0.2	0.4	0.8

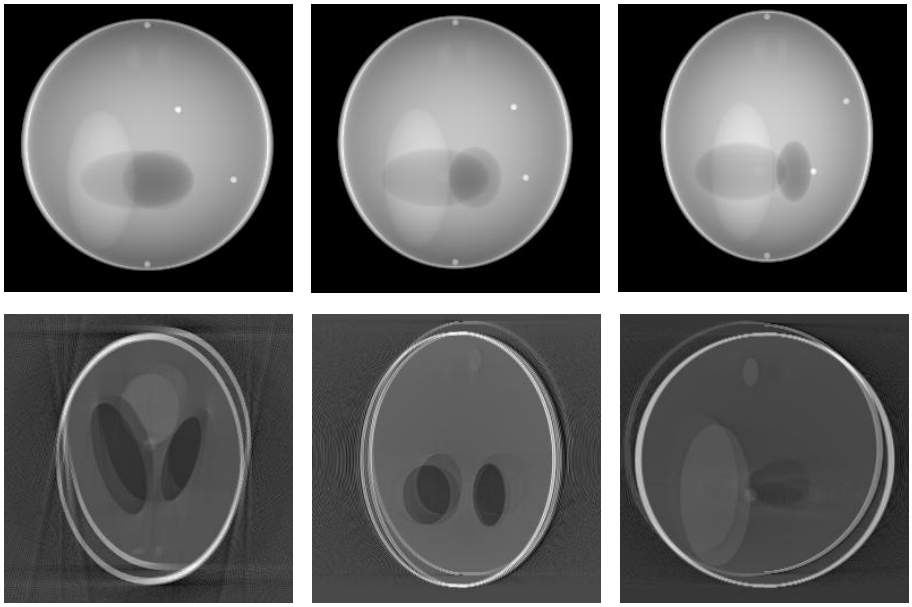

a b c
d e f Figure 6.10 (a-c) Translation Motion Corrupted Projection at 200°, 220° and 240° Source Position. (d-f) Axial, Coronal and Sagittal Slices of the Translational Motion Corrupted Reconstructed Volume.

Table 6.22 Estimated Marker Coordinates
(Translational Motion Corrupted Case)

β_m	Actual Marker Position (cm) (before motion)			Actual Marker position (cm) (after motion)			Estimated marker Position (cm) (after motion)		
	x_i	y_i	z_i	X_I	Y_I	Z_I	x_i'	y_i'	z_i'
200	0	0	9.25	0.20	0.0	9.25	0.2015	0	9.25
	7.25	0	3.25	7.45	0.0	3.25	7.4514	0	3.25
	0	-7.25	-3.25	0.20	-7.25	-3.25	0.2015	-7.25	-3.25
	-0.75	0.75	-9.25	-0.55	0.75	-9.25	-0.5485	0.75	-9.25
220	0.20	0.0	9.25	0.40	0.40	9.25	0.3899	0.4000	9.2499
	7.45	0.0	3.25	7.65	0.40	3.25	7.6399	0.4000	3.2500
	0.20	-7.25	-3.25	0.40	-6.85	-3.25	0.3905	-6.8500	-3.2500
	-0.55	0.75	-9.25	-0.35	1.15	-9.25	-0.3601	1.1500	-9.2499
240	0.40	0.40	9.25	0.60	0.80	10.050	0.5906	0.8000	10.0499
	7.65	0.40	3.25	7.85	0.80	4.0500	7.8406	0.8000	4.0500
	0.40	-6.85	-3.25	0.60	-6.45	-2.4500	0.5891	-6.4500	-2.4500
	-0.35	1.15	-9.25	-0.15	1.55	-8.4500	-0.1589	1.5500	-8.4500

Table 6.23 Comparisons of Estimated and Actual Motion Parameters
(Translational Motion Corrupted Case)

Motion Parameters		$\beta = 200$	$\beta = 220$	$\beta = 240$
Estimated	t_{xe} (cm)	0.2015	0.1900	0.1907
	t_{ye} (cm)	5.6112e-010	0.4000	0.4000
	t_{ze} (cm)	-5.1085e-009	-3.8690e-008	0.8000
	$\vartheta_e{}^o$	5.3459e-007	-8.9305e-007	-6.2537e-006
	$\delta_e{}^o$	-8.4938e-008	8.5328e-006	-2.9586e-005
	$\alpha_e{}^o$	-2.8764e-009	6.6432e-007	-2.4038e-006
Actual	t_x (cm)	0.2	0.2	0.2
	t_y (cm)	0.0	0.4	0.4
	t_z (cm)	0.0	0.0	0.8
	ϑ^o	0.0	0.0	0.0
	δ^o	0.0	0.0	0.0
	α^o	0.0	0.0	0.0

Table 6.24 Rotational Motion Given to the Phantom During Scanning of Projections at 260^o, 270^o, and 280^o

Step	*Roll*	*Pitch*	*Yaw*	t_x (cm)	t_y (cm)	t_z(cm)
260	15°	0°	0°	0	0	0
270	15°	30°	0°	0	0	0
280	15°	30°	25°	0	0	0

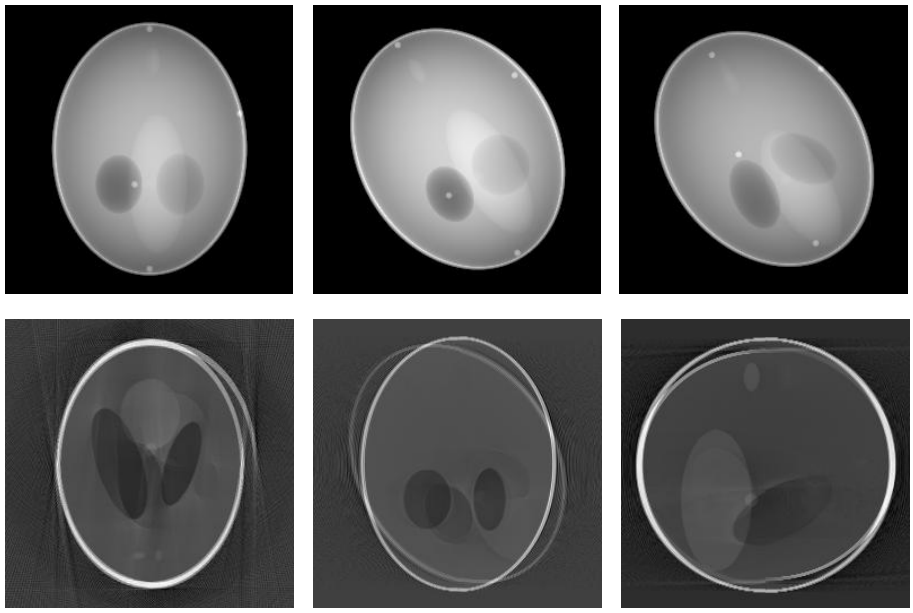

a b c
d e f Figure 6.11 (a-c) Rotational Motion Corrupted Projection at 260^o, 270^o and 280^o Source Position. (d-f) Axial, Coronal and Sagittal Slices of the Rotational Motion Corrupted Reconstructed Volume.

Table 6.25 Estimated Marker Coordinates
(Rotational Motion Corrupted Case)

β_m	Actual Marker Position (cm) (before motion)			Actual Marker position (cm) (after motion)			Estimated marker Position (cm) (after motion)		
	x_i	y_i	z_i	X_I	Y_I	Z_I	x_i'	y_i'	z_i'
260	0	0	9.25	0	-2.3941	8.9348	0.0072	-2.3941	8.9349
	7.25	0	3.25	7.2500	-0.8412	3.1393	7.2572	-0.8412	3.1393
	0	-7.25	-3.25	0	-6.1618	-5.0157	0.0072	-6.1618	-5.0157
	-0.75	0.75	-9.25	-0.7500	3.1185	-8.7407	-0.7428	3.1185	-8.7407
270	0	-2.3941	8.9348	4.0054	-4.6250	6.9375	3.9471	-4.6249	6.9372
	7.2500	-0.8412	3.1393	7.6860	-1.6250	-1.1875	7.6276	-1.6250	-1.1874
	0	-6.1618	-5.0157	-3.2198	-4.6537	-5.5768	-3.2787	-4.6535	-5.5766
	-0.7500	3.1185	-8.7407	-4.4674	5.2745	-6.2377	-4.5262	5.2743	-6.2375
280	4.0054	-4.6250	6.9375	8.2848	-3.0473	2.7640	8.2805	-3.0473	2.7640
	7.6860	-1.6250	-1.1875	5.8557	1.3377	-5.2006	5.8515	1.3377	-5.2006
	-3.2198	-4.6537	-5.5768	-4.2244	-5.3370	-4.0983	-4.2283	-5.3370	-4.0983
	-4.4674	5.2745	-6.2377	-8.4535	3.4610	-1.8020	-8.4574	3.4610	-1.8020

Table 6.26 Comparisons of Estimated and Actual Motion Parameters
(Rotational Motion Corrupted Case)

Motion Parameters		$\beta = 260$	$\beta = 270$	$\beta = 280$
Estimated	t_{xe} (cm)	0.0072	-0.0585	-0.0041
	t_{ye} (cm)	3.7148e-009	-1.0912e-006	2.5090e-007
	t_{ze} (cm)	-1.1130e-008	1.5781e-006	-2.0241e-007
	ϑ_e°	4.4109e-007	29.9988	29.9999
	δ_e°	15.0001	14.9993	14.9999
	α_e°	1.1443e-007	5.8719e-006	24.9989
Actual	t_x (cm)	0.0	0.0	0.0
	t_y (cm)	0.0	0.0	0.0
	t_z (cm)	0.0	0.0	0.0
	ϑ °	0.0	30.00	30.00
	δ °	15.00	15.00	15.00
	α °	0.0	0.0	25.00

Table 6.27 Combined Rotational and Translational Motion Given to the Phantom during Scanning of Projections at 160^o, 180^o, and 200^o

Step	*Roll*	*Pitch*	*Yaw*	t_x (cm)	t_y (cm)	t_z(cm)
160	15°	0°	0°	1.0	0	0
180	15°	20°	0°	1.0	2.0	0
200	15°	20°	25°	1.0	2.0	1.5

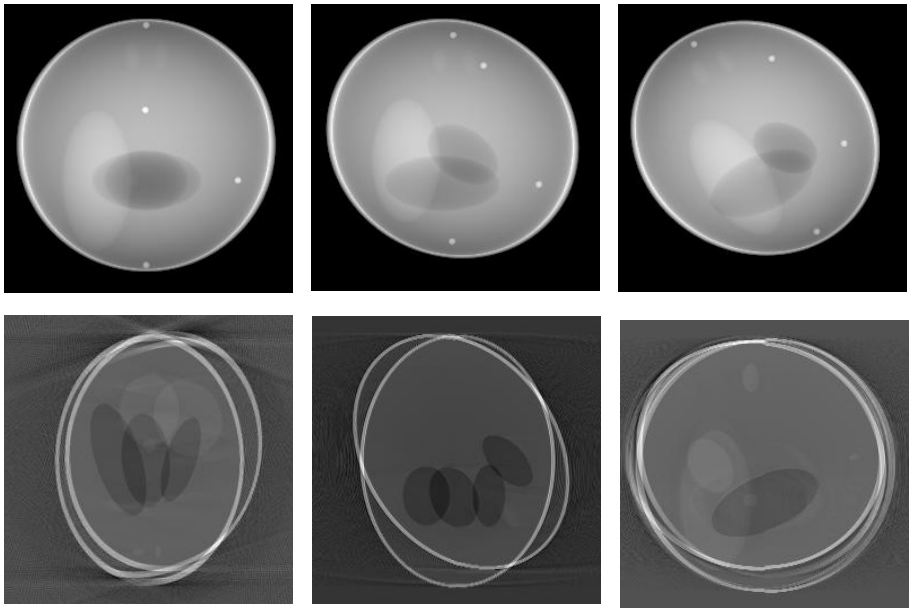

a b c
d e f Figure 6.12 (a-c) Combined Motion Corrupted Projection at 160^o, 180^o and 200^o Source Position. (d-f) Axial, Coronal And Sagittal Slices of the Translational and Rotational Motion Corrupted Reconstructed Volume.

Table 6.28 Estimated Marker Coordinates
(Combined Motion Corrupted Case)

β_m	Actual Marker Position (cm) (before motion)			Actual Marker position (cm) (after motion)			Estimated marker Position (cm) (after motion)		
	x_i	y_i	z_i	X_I	Y_I	Z_I	x_i'	y_i'	z_i'
160	0	0	9.25	1.0000	-2.3941	8.9348	1.0036	-2.3941	8.9348
	7.25	0	3.25	8.2500	-0.8412	3.1393	8.2536	-0.8412	3.1393
	0	-7.25	-3.25	1.0000	-6.1618	-5.0157	1.0036	-6.1618	-5.0157
	-0.75	0.75	-9.25	0.2500	3.1185	-8.7407	0.2536	3.1185	-8.7407
180	1.0000	-2.3941	8.9348	4.6796	-2.6250	7.1855	4.6741	-2.6250	7.1855
	8.2500	-0.8412	3.1393	9.7151	0.3750	-0.1769	9.7091	0.3750	-0.1769
	1.0000	-6.1618	-5.0157	-0.2629	-2.6537	-6.3932	-0.2685	-2.6537	-6.3932
	0.2500	3.1185	-8.7407	-1.3768	7.2745	-7.2607	-1.3824	7.2745	-7.2607
200	4.6796	-2.6250	7.1855	8.7838	0.7798	5.7830	8.7872	0.7798	5.7830
	9.7151	0.3750	-0.1769	9.0786	6.2171	-1.8923	9.0820	6.2171	-1.8923
	-0.2629	-2.6537	-6.3932	-0.9672	0.0802	-4.8584	-0.9632	0.0802	-4.8584
	-1.3768	7.2745	-7.2607	-5.5266	8.7832	-2.8502	-5.5228	8.7832	-2.8502

Table 6.29 Comparisons of Estimated and Actual Motion Parameters
(Combined Motion Corrupted Case)

Motion Parameters		$\beta = 160$	$\beta = 180$	$\beta = 200$
Estimated	t_{xe} (cm)	1.0036	0.9945	1.0037
	t_{ye} (cm)	1.7047e-009	2.0000	2.0000
	t_{ze} (cm)	-5.1528e-009	9.5482e-008	1.5000
	ϑ_e°	2.2245e-007	20.0009	20.0010
	δ_e°	15.0000	14.9999	15.0000
	α_e°	5.7943e-008	-2.9808e-007	24.9991
Actual	t_x (cm)	1.0	1.0	1.0
	t_y (cm)	0.0	2.0	2.0
	t_z (cm)	0.0	0.0	1.5
	ϑ °	0.0	20.00	20.00
	δ °	15.00	15.00	15.00
	α °	0.0	0.0	25.00

6.4 Qualitative and Quantitative Analysis of Artifacts Mitigation Approach

To demonstrate the efficacy of the proposed artifact mitigation technique, the estimated motion parameters are applied to the back-projection stage of the MBMD-FDK algorithm in order to reconstruct the 3D volume from the different cases of motion-corrupted projections data sets. In Figs 6.13, 6.15, and 6.17, the axial, coronal and sagittal slices of reconstructed volume of motion corrupted cases, motion compensated cases, and motion free cases are plotted side by side. From these plots, it can be inferred that the motion artifacts have been significantly reduced by the marker-based artifacts mitigation approach.

In order to assess the accuracy of motion correction, the motion free study is treated as the gold standard. Particularly, the axial slice at z = -2.5cm (which intersects most of the constituent ellipsoids of the 3D Shepp-Logan phantom) is chosen for comparison. The mean square error (MSE) of the motion compensated and uncompensated slices (normalized) are calculated with respect to a motion-free slice (normalized). For the combined motion-corruption case, the MBMD-FDK approach reduced the MSE in the axial slice from 0.0155 (without motion correction) to 0.0051 (a factor of 3.0392). Whereas for the same motion corruption case, correlation-based approach reduced the MSE in the axial slice to 0.0119 (a factor of 1.298). For translational motion-corrupted case, the MBMD-FDK approach reduced the MSE in the axial slice from 0.0103 (without motion correction) to 0.0035 (a factor of 2.943). On the other hand, the correlation based approach reduced the MSE in the axial slice to 0.0041 (a factor of 2.512). For rotational motion-corrupted, the MBMD-FDK approach reduced the MSE in the axial slice from 0.0073 to 0.0037 (a factor of 1.958) and the correlation-

based approach reduced the MSE from 0.0073 to 0.0031 (a factor of 2.354). The improvement in accuracy can also be observed in the one pixel wide intensity profile of Figs. 6.14, 6.16 and 6.18. In the left column, one pixel wide intensity profile of the axial slices at z = -2.5cm of the above motion-corrupted cases and motion-compensated cases are plotted against the motion-free case, keeping Y fixed at 129^{th} position while X varies from 1 to 256. In the right column, the similar intensity profiles are plotted keeping X fixed at 131^{st} position, while Y varies from 1 to 256. These particular X and Y positions are chosen so that the maximum intensity variation can be observed. From these intensity profiles, it is evident that motion correction using the MBMD-FDK approach resulted in a profile very close to that of a motion-free case.

From a finer investigation presented in Figs 6.19 and 6.20, it is revealed that the MBMD-FDK approach produces superior results for the above combined motion corruption case and translation corruption case. Particularly, when motions occur near $\beta = 180^{o}$ positions (in other words, if motions occur in both half circles of the source-detector data acquisition orbit), the MBMD-FDK approach produces finer reconstruction compared to the simple correlation artifact mitigation approach. To investigate the performance of the MBMD-FDK approach on a combined motion-corruption case, the one pixel wide intensity profiles taken from the reconstructed axial slices of a simple correlation case, the MBMD-FDK case, and motion-free ideal case are compared in Fig. 6.19. From these plots it is evident that the MBMD-FDK recovered the broken skull artifacts and produced a reconstruction profile closer to the ideal case. The MBMD-FDK algorithm works best for a translation motion-corrupted case. From Fig 6.17, it is

observed that the MBMD-FDK produces an almost identical reconstruction of a motion-free ideal case.

For rotational motion corruption cases, the MBMD-FDK approach produces inferior results, (as can be seen in Fig. 6.18) compared to the simple correlation artifacts mitigation approach presented in Chapter 4. A closer investigation reveals the fact that rotation during data acquisition time skips some projections, which resulted in an incomplete X-ray projection data set after a full scan. For the particular rotational motion corruption case, consider the instant at $\beta=280^{o}$ position when the phantom moves 30^{0} about z-axis in between 279^{0} to 280^{0} source detector position. If the head moves opposite to the direction of the source-detector pair rotation, then 30 projections will be missed during data acquisition time. If the head moves in the same direction of the source-detector pair rotation, then 30 projections will be missing after the full scan. Due to these 30 unrecoverable missing projections, the MBMD-FDK will have an incomplete X-ray projection set during the reconstruction process, resulting in some distortion of the reconstructed volume. Whereas, in the simple correlation based approach the missing projection are replaced by the counterpart motion free projections. The bottom line is if motions occur during the start or the end of the data acquisition time, then the simple correlation approach produces better results; otherwise the MBMD-FDK approach would produce improve the quality of reconstruction.

Since the correlation-coefficient between the adjacent projections could be affected by the signal to noise ratio (SNR) of the X-ray data acquisition system, small and gradual motion could be undetected by the simple correlation-based approach. In that case, the MBMD-FDK approach would be suitable to detect small and gradual variation

of motions. In the preceding section (6.2), the MBMD system was tested with small and gradual variation motion. Simulation results summarized in Table 6.20 validates that the MBMD approach can estimate rotation and translational parameters of small and gradual motion within acceptable range of accuracy.

Most of the existing 3D CT motion artifacts mitigation techniques are tested either on the physical phantom or on human. Since the author did not have any access to the CT scanner, the author could not compare the proposed artifacts mitigation techniques with the existing technique. That being said, one important advantage of the proposed techniques over the existing marker based techniques [91-93] is that the proposed techniques do not use any curve fitting or linear interpolation techniques which often fail to tackle large or abrupt variation of head motion.

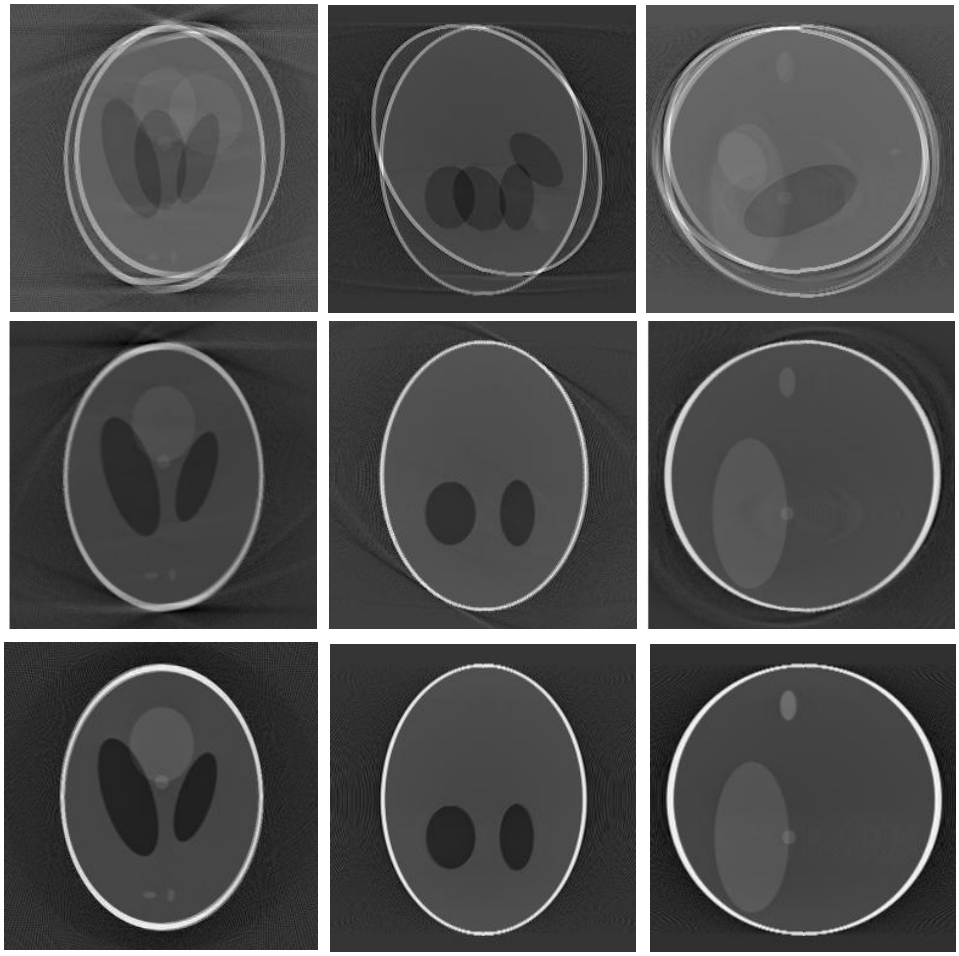

a b c
d e f
g h i

Figure 6.13 (a-c) Axial, Coronal, and Sagittal Slices of the Combined Motion Corruption Case. (d-f) Similar Slices after MBMD-FDK Motion Compensation. (g-i) Similar Slices for Motion Free Ideal Case.

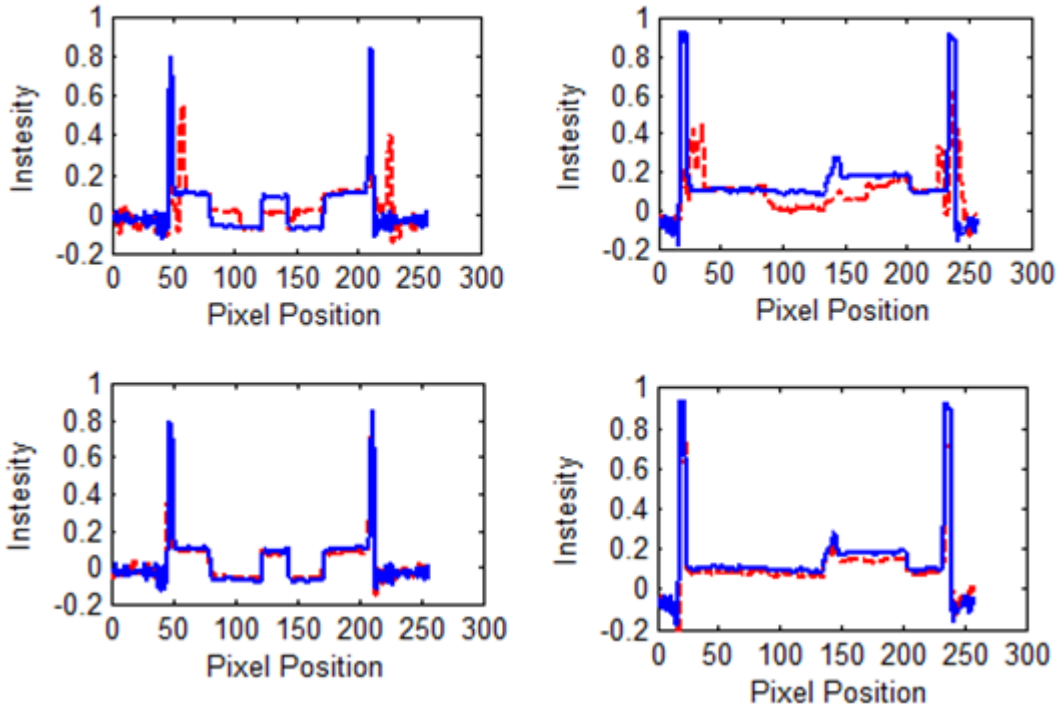

Figure 6.14 Comparison of One Pixel Wide Intensity Profiles Taken From the Axial Slices at Z =-2.5 Cm. (Combined Motion Corruption Case)

Motion free case (solid line). Left col.- Intensity profiles at Y=129th position,

Right col.-Intensity profiles at X=131st position.

(1st row - Motion corrupted case, 2nd row – Motion compensated case)

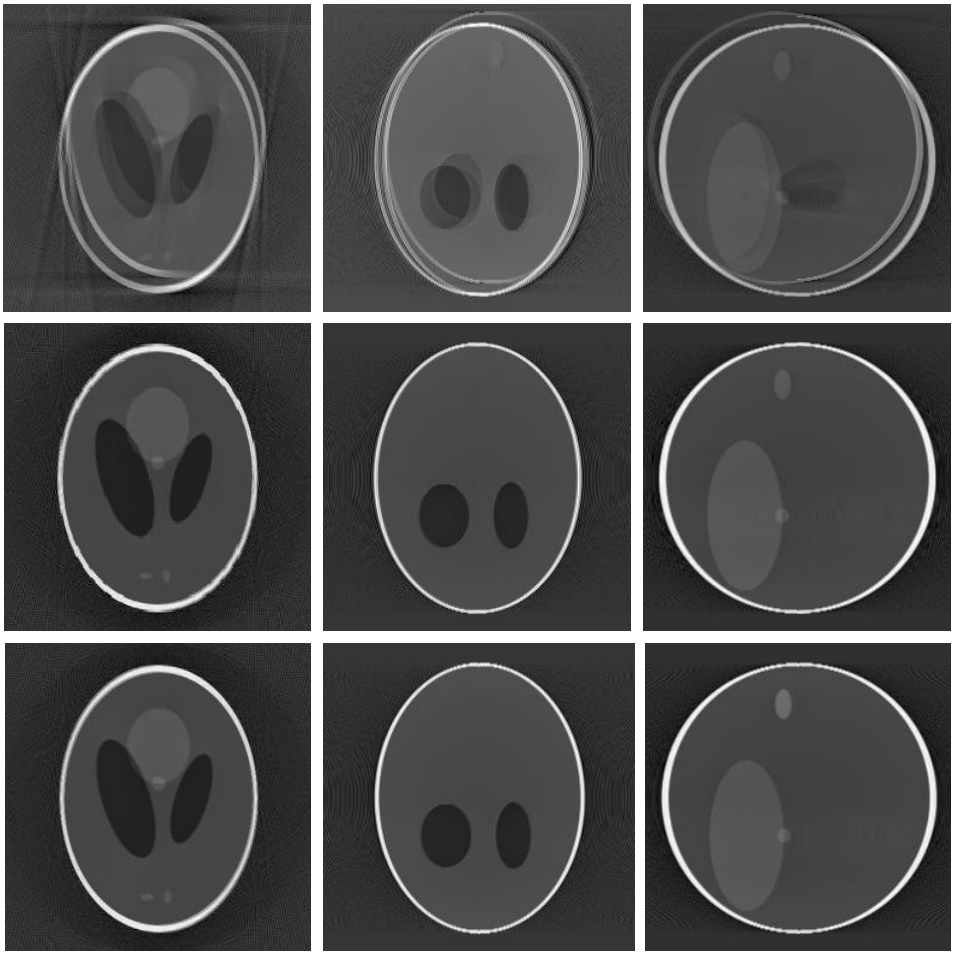

a b c
d e f
g h i

Figure 6.15 (a-c) Axial, Coronal, and Sagittal Slices of the Translation Motion Corruption Case. (d-f) Similar Slices after Motion Compensation. (g-i) Similar Slices of Motion Free Ideal Case.

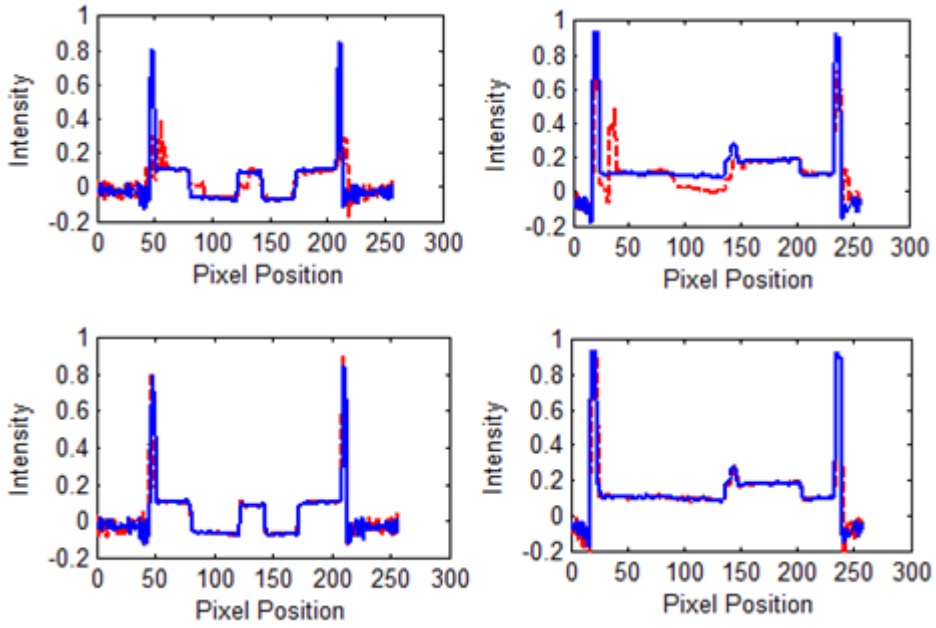

Figure 6.16 Comparison of One Pixel Wide Intensity Profiles Taken From the Axial Slices at z =-2.5 Cm. (Translation Motion Corruption Case)

Motion free case (solid line). Left col.- Intensity profiles at Y=129th position,

Right col.-Intensity profiles at X=131st position.

(1st row - Motion corrupted case, 2nd row – Motion compensated case)

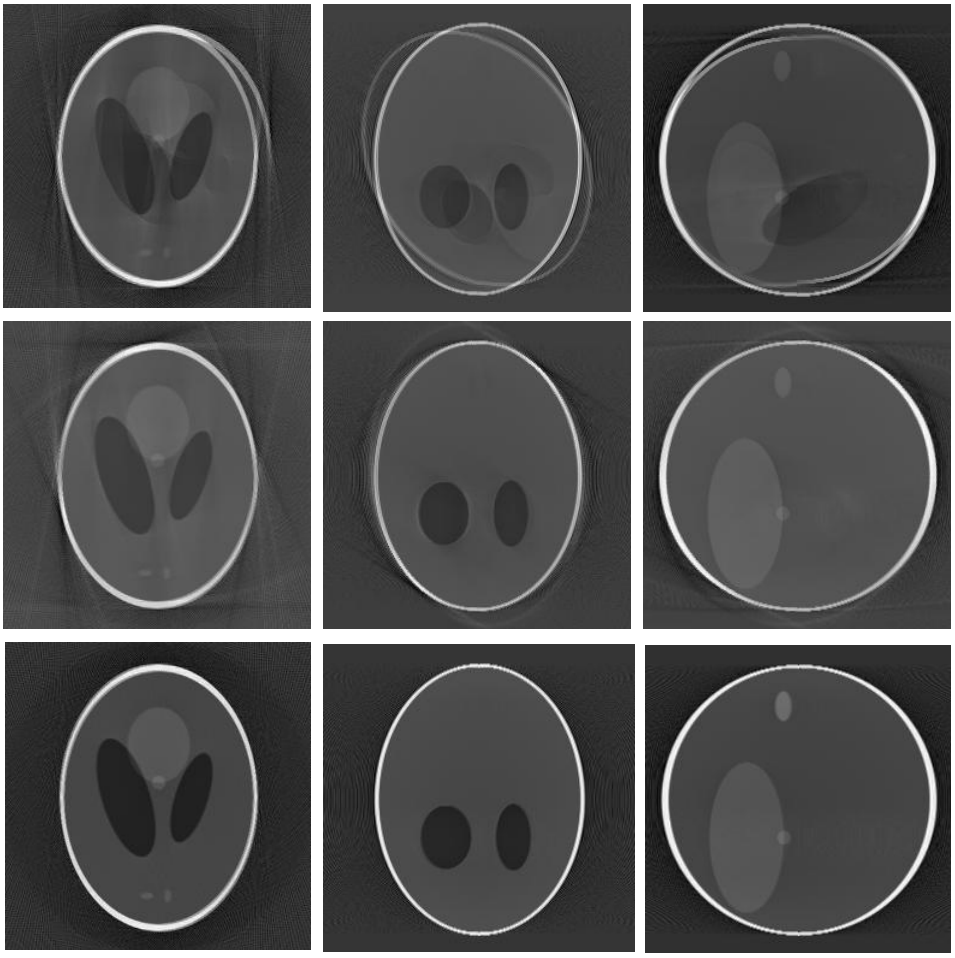

a b c
d e f
g h i

Figure 6.17 Axial, Coronal, and Sagittal Slices of the Rotational Motion Corruption Case. (d-f) Similar Slices after Motion Compensation.(g-i) Similar Slices of Motion Free Ideal Case.

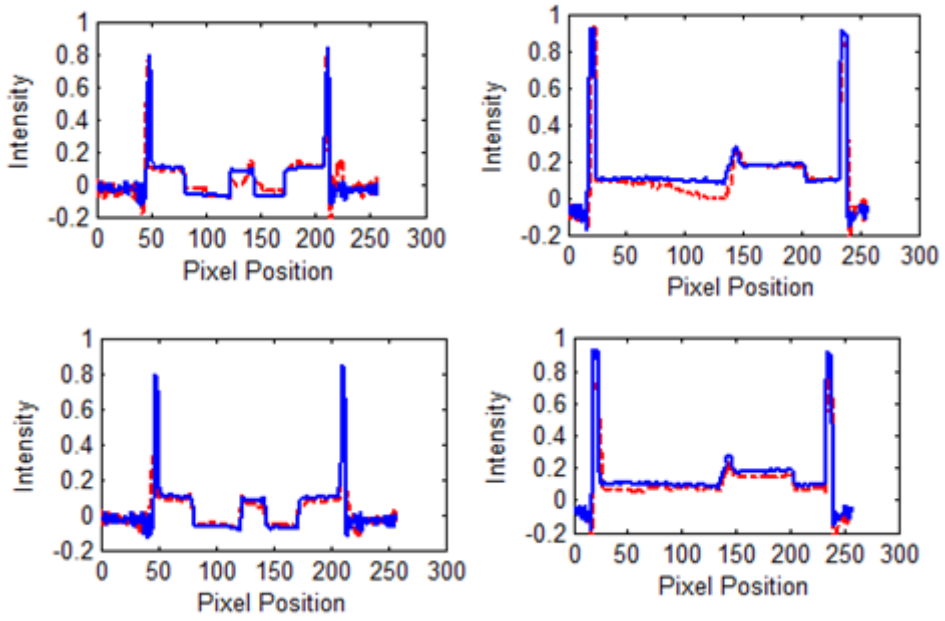

Figure 6.18 Comparison of One Pixel Wide Intensity Profiles Taken From the Axial Slices at z =-2.5 Cm. (Rotational Motion Corruption Case)

Motion free case (solid line). Left col.- Intensity profiles at Y=129th position,

Right col.-Intensity profiles at X=131st position.

(1st row - Motion corrupted case, 2nd row – Motion compensated case)

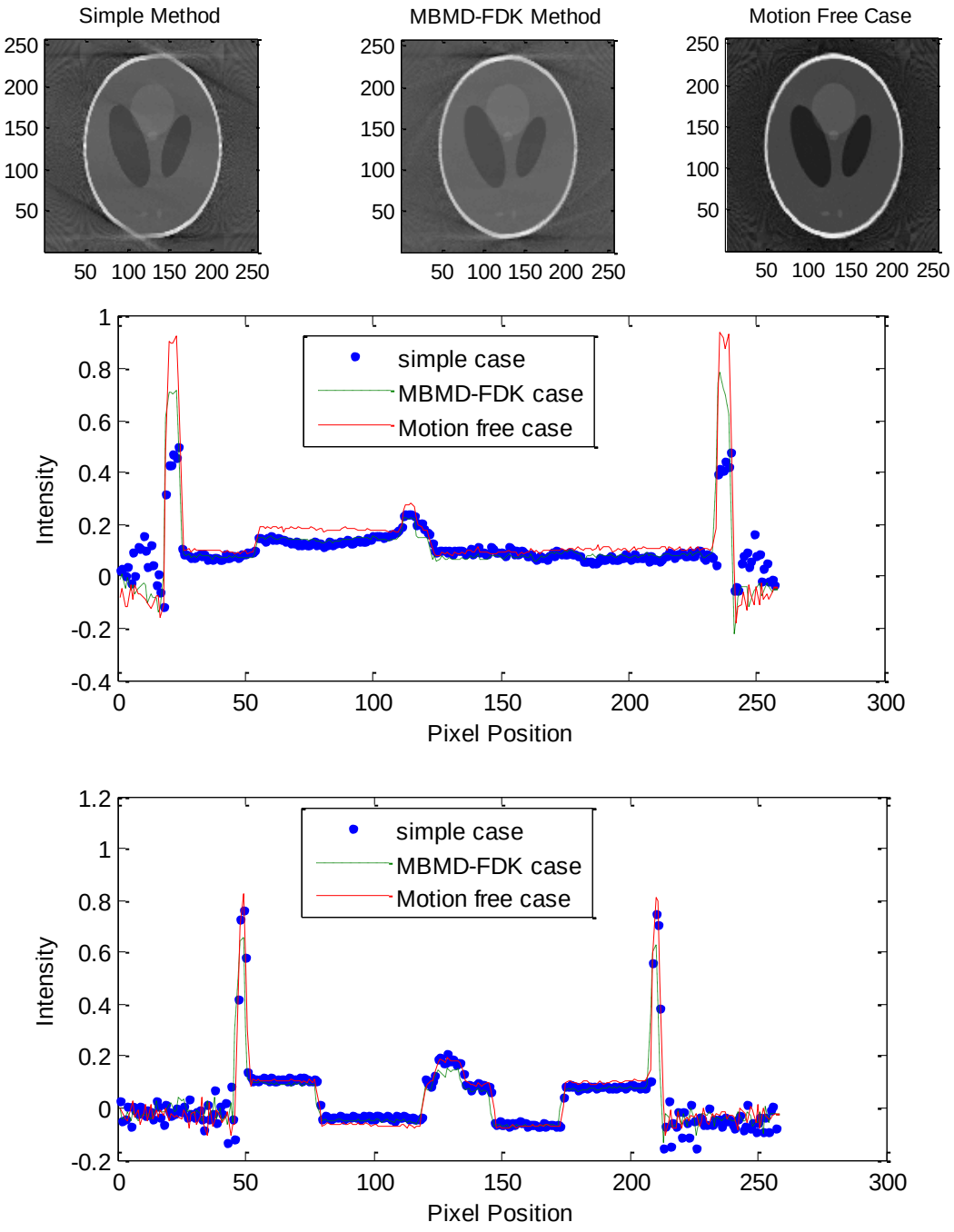

Figure 6.19 Comparison of One Pixel Wide Reconstruction Line
(Combined Motion Corruption Case)

Axial slices of the Simple case, MBMD-FDK case, and the Ideal case (1st row).
Intensity profiles at X=118th position (2nd row), Y=129th position (3rd row)

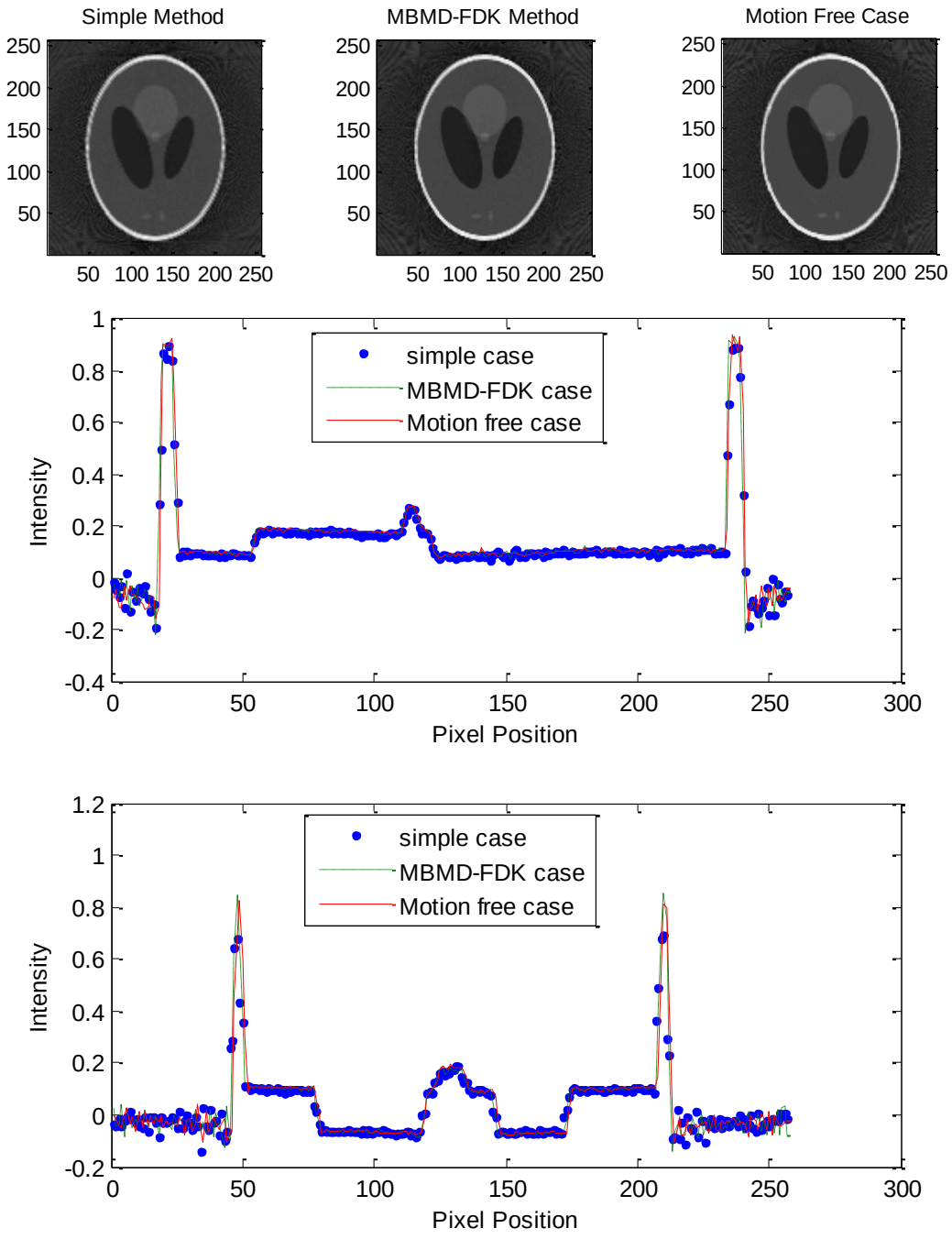

Figure 6.20 Comparison of One Pixel Wide Reconstruction Line
(Translation Motion Corruption Case)

Axial slices of the Simple case, MBMD-FDK case, and the Ideal case (1st row).
Intensity profiles at X=118th position (2nd row), Y=129th position (3rd row)

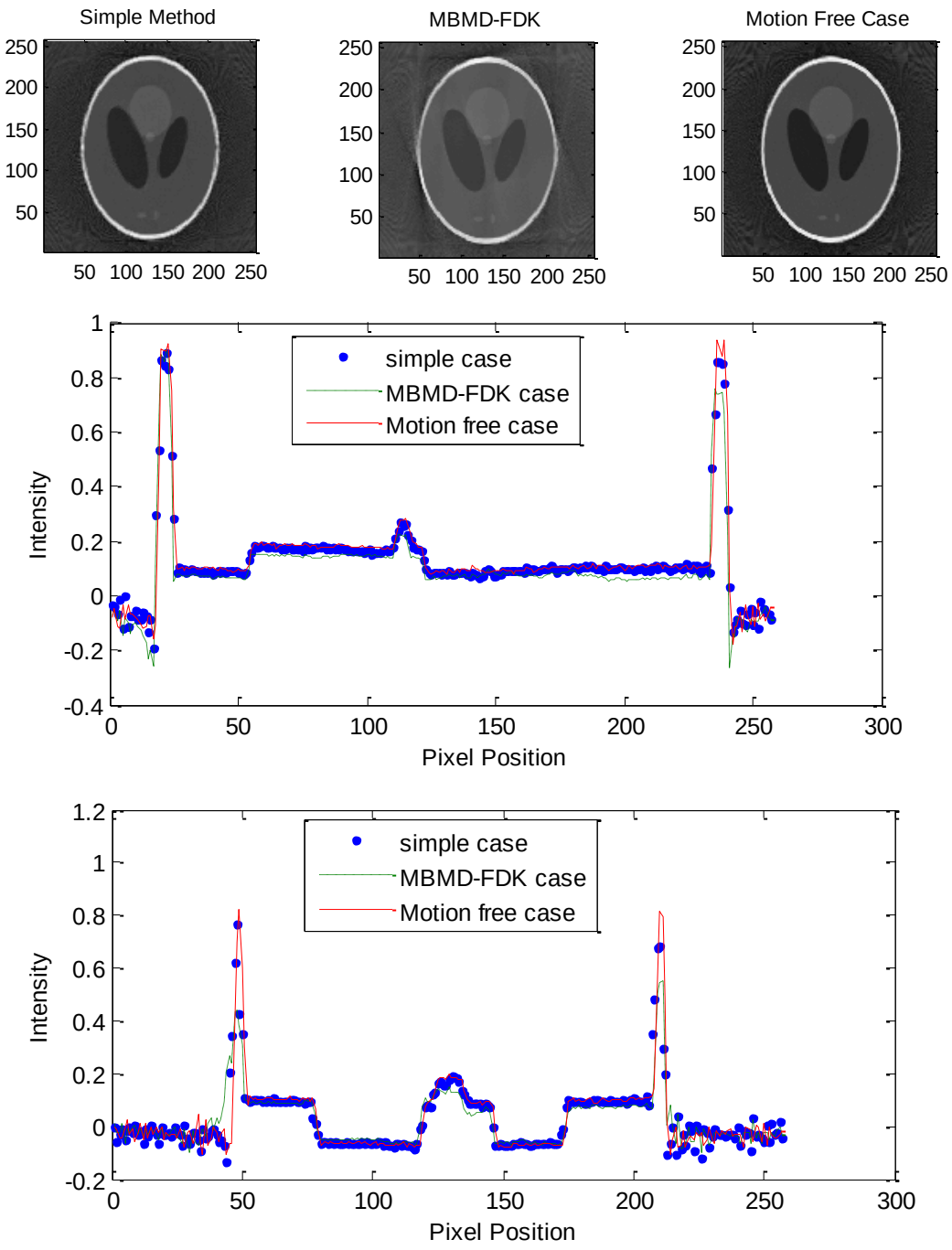

Figure 6.21 Comparison of One Pixel Wide Reconstruction Line
(Rotation Motion Corruption Case)

Axial slices of the Simple case, MBMD-FDK case, and the Ideal case (1st row).
Intensity profiles at X=118th position (2nd row), Y=129th position (3rd row)

CHAPTER 7

CONCLUSION AND FUTURE WORKS

7.1 Introduction

Head motion remains as one of the significant sources of problem in three-dimensional tomographic (CT) brain imaging studies. Even with substantial amount of head restraints some form of head motion is inevitable, especially with less cooperative patient like children. Head motion can cause blurring, doubling, loss of resolution and other related artifacts during reconstruction process. Motion artifacts are clinically significant because they degrade images and interfere with diagnosis. In some cases, artifacts sometimes obscure anatomy, sometimes mimic some pathology which can lead to misdiagnosis of diseases, sometimes radiologists are forced to discard the motion corrupted scanned data set and rescan the patient, which is not only wastage of time, resource and money but also harmful for the patient because of radiation overdose.

While the CT systems have been improved significantly over the last two decades, there still remains a need to mitigate motion artifacts in 3D cone-beam CT system. The existing popular artifacts mitigation techniques (external sensor-based method and sinogram/linogram method) have some limitations. In particular, the external sensor-based methods are affected by the systematic biasing of the external sensors and sometimes become difficult to implement. Sinogram/linogram techniques often fail to

produce desired results in case large and abrupt variation of motion. In this dissertation, two techniques have been proposed to resolve the shortcoming of the existing techniques. One is correlation based technique and the other is marker based technique (called MBMD-FDK technique). Unlike using sinogram/linogram technique or external sensor-based method, the proposed techniques are developed with a goal to form a comprehensive artifacts-reduction methodology. The potential of the proposed techniques have been demonstrated with computer simulations of a well-known mathematical phantom (known as 3D Shepp-Logan phantom).

The remainder of this chapter discusses briefly the major contribution of this research followed by the challenges and future works.

7.2 Design and Implementation of a Computer Simulation Platform

In this dissertation, a computer simulation platform has been designed and implemented to simulate any form of practical motion artifacts. OSCaR-02 implementation steps are used for efficient FDK based 3D reconstruction. However, OSCaR-02 was developed for computing three-dimensional reconstruction from data gathered from practical cone-beam X-ray CT scanning geometries; therefore the OSCaR-02 source code has been modified to interface it with the 3D Shepp-Logan mathematical phantom. In order to simulate motion, the existing X-ray projection equations (Zhu *et al*. [82] an A. C. Kak *et al.*[80]) have been modified. The existing projection equations work only on the phantom listed in Table 3.1. However, for more general cases like if the ellipsoids need to be reoriented to some other places or if the phantom needs to be perturbed during data acquisition process, the existing projection equations will not work.

In this dissertation, a general form projection equation, which allows the provision for reorienting the constituent ellipsoids of the phantom, has been derived. The proposed X-ray projection equation also incorporates six-degrees of freedom of motion parameters to simulate any form practical head motion during X-ray scanning process. In chapters (4, 6), simulation results of different motion corrupted cases demonstrated the functionality of this simulation platform. The computer simulation platform implemented in this research could also encourage future researchers to test their own motion compensation algorithms.

7.3 Design and Implementation of a Correlation-Based Artifacts Mitigation Approach

In this research, a simple correlation-based technique has been proposed to detect location of motion (in other words, source detector positions where motion occurred during X-ray scanning time) and mitigate motion artifacts in 3D cone-bean CT system. The idea behind the motion detection originated from the fact that the correlation between the adjacent projections should be very high for motion free ideal case because projections are taken only one degree apart. If there is any head motion during data acquisition time, the correlation between adjacent projections would drop to the projection pair (position) where motions occur. Simulation results demonstrated the validity of our assumption. After knowing the location of motion, artifacts caused by motion are mitigated by replacing the motion corrupted projection by their counterpart stable projections. Simulation results demonstrated in chapter (4) validates the above claim. This simple technique produces desired results if motions occur near the beginning and the end of data acquisition time. If motions occur near 180^0 of the data scanning path

or both half circle of the data acquisition path then this technique could not produce desired results. The correlation-based motion detection works very well in case of large and abrupt variation of motion. However, correlation-based motion detection may not work well in case of small or gradual variation of motion because projection could be affected by the signal to noise ratio of the X-ray acquisition system. In order to resolve these shortcomings marker-based system was developed in this research.

7.4 Marker-Based Head Motion Measurement System

A Marker-Based Motion Detection (MBMD) system consists of four markers (with high attenuation constant) placed on the surface of head are used to estimate the parameters of head motion. Markers are placed in such a way that their position will be linearly independent and the marker projections on the detector plate will never cross each other in case of any practical head motion. Coordinates of the markers on head and their corresponding projections on the detector plate are known for motion free ideal case. In case of any head motion the markers and their projections will shift from their ideal position. The shifted position of the markers can be estimated from the shifted position of their projections using a numerical iterative technique. The key parameter that is used in the iteration process is the relative distance between the markers that always remain constant as because they are on a solid body. After knowing the shifted position of the markers a matrix manipulation is used to extract the parameters of motion. The marker based system is tested with two different data sets. First, the linearity and accuracy of the system was tested with small and gradual variation of each of the six parameters of motion. Simulation results demonstrated that the marker-based system has

pre requisite linearity and accuracy. Secondly, the MBMD system is tested with large and abrupt variation of motion. Simulation results verified the accuracy of the system. One important issue needs to be mentioned is that the X-ray projections, from which the coordinate markers projection cannot be detected, need to be discarded from the reconstruction process. That is why, in the simulation process it is assumed that the head remains stationary during the acquisition of individual projections and only moves between the projections.

After finding the location and parameters of motion, a modified FDK algorithm is used to mitigate motion artifacts. In the modified FDK algorithm (MBMD-FDK), a coordinate transformation is used to correct the position of the reconstruction grid according to the estimated motion parameters so that the contribution of every projection will be placed in its corresponding reconstruction grid. Simulation results validated the efficacy of the MBMD-FDK approach. From the simulation results, it was also concluded that if motion occur near the beginning or the end of the data acquisition path then the correlation-based approach produced better results otherwise marker-based approach would produce better reconstruction.

A fundamental limitation of the research presented in this dissertation is that no practical data was utilized. The system was verified on a synthetic data set (a perfect mathematical model) only. Processing of the projection is a crucial element for of all CT systems and greatly affects the quality of the resulting images. In our future endeavor, efforts will be made to implement the proposed techniques on a practical data set so that the clinical significance of this technique can be established.

7.5 Challenges and Future Work

In this dissertation, it is assumed that the head remains stationary during the acquisition of individual projections and only moves between projections. Although the current CT system's scanning speed is extremely high (about 3 to 5sec) [90], a situation may arise where the X-ray projections are affected by head motion in such a way that the coordinates of the marker projections cannot be detected from some of the X-ray projections. In that scenario, those X-ray projections affected by motion need to be discarded from the reconstruction process. However, In order to have better reconstruction, those discarded projections have to be estimated by a suitable predictor. The author is currently working on improving the performance of a Least Square Support Vector Machine (LS-SVM) based time series predictor. A brief discussion about the LS-SVM predictor is given in the following section. Streaking artifacts also remain another major problem in 3D cone-beam CT systems. The author has done some preliminary research on mitigating streaking artifacts. A brief discussion of the streaking artifacts mitigating technique [59] is also presented in the subsequent section.

7.5.1. LS-SVM Time Series Prediction

Suppose motions occur at source positions 160^{o} to 180^{o} in such a way that the corresponding X-ray projections need to be discarded from the reconstruction process. But discarding projections would affect the quality of the reconstructed image because of incomplete data set. Therefore, in order to improve the quality of the reconstructed image, it is necessary to estimate those discarded projections from the available stable projection. The LS-SVM-based time series predictor could be used to predict every pixel

of the motion corrupted projections ($\beta = 160^o$ to 180^o) from the corresponding pixels of previous stable projections at $\beta = 1^o$ to $\beta = 159^o$ positions. A more complete description can be found in Ujjal *et al.*[87]. In the near future, the author intends to incorporate the LS-SVM predictor into the current MBMD-FDK system and compare the results with the other approaches.

7.5.2. Streaking Artifacts

Another major form of artifacts inherent in the cone-beam CT system is the streaking artifacts. Several factors such as the effect of the nonlinear components of the partial volume error (which occurs when an object partially enters into the scanning plane), the large variations and discrepancies in the projection (which are created because of the presence of small bone structure), metal artifacts, and motion of the organ, all may originate in streaking artifacts [79]. The author has done some preliminary work to mitigate the streaking artifacts (as shown in Fig. 7.1) originating from the large variations and discrepancies in the projections. A detailed description of the technique can be found in Ujjal *et al.* [59]. The author intends to extend this work to mitigate streaking artifacts originating from other factors.

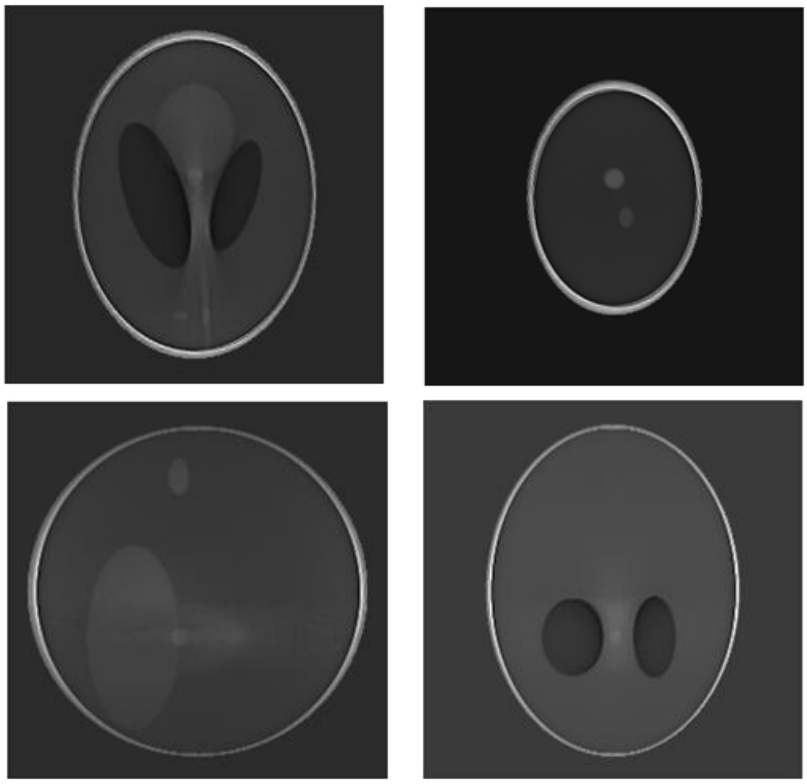

a b
c d Figure 7.1 Streaking Artifacts originated from the large variations and discrepancies in the projections (a) & (b) Axial Slices at z = -2.5cm and z = 6.5cm (c) Sagittal Slice (d) Coronal Slice

APPENDIX

Matlab Code to generate X-ray projection of the 3D Shepp-Logan Phantom

```
clear all;
tic;
s1='Proj_0000';
s3='.tif';
dso=4*400;
dde=4*100;



%      p0    A      B     C     x0      y0      z0    phi      xi     psi
%   ------------------------------------------------------------------------
e =  [ 1000 6.900  9.20  9.00      0      0       0      0       0       0
       -800  6.624  8.74  8.80      0      0       0      0       0       0
       -200  4.100  1.60  2.10   -2.2      0    -2.5     72       0       0
       -200  3.100  1.10  2.20    2.2      0    -2.5    108       0       0
        100  2.100  2.50  5.00      0    3.5    -2.5      0       0       0
        100  0.460  0.46  0.46      0     1.    -2.5      0       0       0
        100  0.460  0.23  0.20   -0.8   -6.5    -2.5      0       0       0
        100  0.460  0.23  0.20    0.6   -6.5    -2.5     90       0       0
        100  0.560  0.40  1.00    0.6   -1.05    6.25    90       0       0
        100  0.560  0.56  1.00      0    1.00    6.25     0       0       0
];

ellipse=e;

%for projection data
[j,i]=meshgrid(1:256,1:256);
j=gpuArray(flatten(j));
i=gpuArray(flatten(i));


R=zeros(256,256);sR=prod(size(R));
R=flatten(R);
R1=R;
R2=R;


phim=0;
psim=0;
xim=0;

beta=[0.0085:(pi/180):2*pi];
betaD=beta.*(180/pi);
[ic,jc]=size(beta);
```

```
%% generate combined motion

for n=1:jc
    Beta=beta(n);
    if (n >= 160 & n<180 )
        phiR=15;xiR=0;psiR=0;
        tx=1;
    elseif (n >= 180 & n<200 )
            phiR=15;xiR=20;psiR=0;
            ty=.8;
    elseif (n >= 200)
            phiR=15;xiR=20;psiR=25;
            tz=.4;
    else
        phiR=0;xiR=0;psiR=0;tx=0;ty=0;tz=0;
    end

      for k = 1:size(ellipse,1)
          p0 = ellipse(k,1);      % Amplitude change for this ellipsoid
          A = ellipse(k,2);        % A
          B = ellipse(k,3);        % B
          C = ellipse(k,4);        % C
          x0 = tx+ellipse(k,5);           % x offset
          y0 = ty+ellipse(k,6);           % y offset
          z0 = tz+ellipse(k,7);           % z offset
          phi = (phim+ellipse(k,8));   % first Euler angle in radians
          xi = (xim+ellipse(k,9)); % second Euler angle in radians
          psi =(psim+ellipse(k,10));  % third Euler angle in radians

%         xn=x0;yp=y0;

              % Local Rotation around Each Ellipse

              RR=pmhRotationMatrixR(phi,xi,psi);
              R11=RR(1,1);R12=RR(1,2);R13=RR(1,3);
              R21=RR(2,1);R22=RR(2,2);R23=RR(2,3);
              R31=RR(3,1);R32=RR(3,2);R33=RR(3,3);

              Qc=pmhRotationMatrixR(phiR,xiR,psiR);
              QQ=RR*Qc; %Rotation About Origin xyz

              Q11=QQ(1,1);Q12=QQ(1,2);Q13=QQ(1,3);
              Q21=QQ(2,1);Q22=QQ(2,2);Q23=QQ(2,3);
              Q31=QQ(3,1);Q32=QQ(3,2);Q33=QQ(3,3);

              %Calculate Cx,Cy,Cz
              Cx=R11*x0+R12*y0+R13*z0;
              Cy=R21*x0+R22*y0+R23*z0;
              Cz=R31*x0+R32*y0+R33*z0;

              %Calculate Dxx,Dyy,Dzz,Dxy,Dyz,Dxz and K

              Dxx=(B*C)^2*Q11^2+(A*C)^2*Q21^2+(A*B)^2*Q31^2;
              Dyy=(B*C)^2*Q12^2+(A*C)^2*Q22^2+(A*B)^2*Q32^2;
              Dzz=(B*C)^2*Q13^2+(A*C)^2*Q23^2+(A*B)^2*Q33^2;
```

```
                Dxy=(B*C)^2*Q11*Q12+(A*C)^2*Q21*Q22+(A*B)^2*Q31*Q32;
                Dxz=(B*C)^2*Q11*Q13+(A*C)^2*Q21*Q23+(A*B)^2*Q31*Q33;
                Dyz=(B*C)^2*Q12*Q13+(A*C)^2*Q22*Q23+(A*B)^2*Q32*Q33;

                Dx=(B*C)^2*Q11*Cx+(A*C)^2*Q21*Cy+(A*B)^2*Q31*Cz;
                Dy=(B*C)^2*Q12*Cx+(A*C)^2*Q22*Cy+(A*B)^2*Q32*Cz;
                Dz=(B*C)^2*Q13*Cx+(A*C)^2*Q23*Cy+(A*B)^2*Q33*Cz;

                Kc=(B*C)^2*Cx^2+(A*C)^2*Cy^2+(A*B)^2*Cz^2-(A*B*C)^2;


[a1,b1,c1]=arrayfun(@fn3DMprojectionGM,dso,dde,i,j,Beta,Dxx,Dyy,Dzz,...
                Dxy,Dxz,Dyz,Dx,Dy,Dz,Kc);

            ac1=gather(a1);
            bc1=gather(b1);
            cc1=gather(c1);
            temp1=2.*p0.*sqrt(bc1.^2-ac1.*cc1)./ac1;
            idx1=find((bc1.^2-ac1.*cc1)>0);
            R1(idx1)=R1(idx1)+temp1(idx1);

      end

  Rg11=gpuArray(R1);
  R1=zeros(1,sR);
  Rg1=reshape(Rg11,[256,256]);
  Rp=gather(Rg1);


 negi=Rp(:,:)./max(max(Rp));


    s2=num2str(n);
    if n>=1000
        s1='Proj_0';
    elseif n>=100
        s1='Proj_00';
    elseif n>=10
        s1='Proj_000';
    end

    filename=strcat(s1,s2,s3);
    imwrite(negi,filename);
    filename1={strcat(s1,s2,s3)};
    dlmcell('filename.txt',filename1,'-a');
   % negi=[];
end

negi=[];negp=[];

xlswrite('beta',betaD');
toc;
```

```
function
[a,b,c]=fn3DMprojectionGM(dso,dde,i,j,beta,Dxx,Dyy,Dzz,Dxy,Dxz,Dyz,Dx,D
y,Dz,Kc);

   %% Geometric Parameters equivalence

    ppri=12.8.*(j-129)./128
    p=ppri.*(dso/(dso+dde));
    t=p.*(dso./sqrt(dso^2+p.^2));
    theta=beta+atan(p./dso)+pi/2;

        zetapri=12.8.*(i-129)/128;
        zeta=zetapri.*(dso/(dso+dde));
        r=zeta.*(dso./sqrt(dso^2+zeta.^2));
        gama=atan(zeta./dso);

   %% ***************************************

   %% Parametric Equation's parameter
   ax=sin(theta).*cos(gama);

   ay=-cos(theta).*cos(gama);
   oy=t.*csc(theta);

   az=-sin(gama);
   oz=t.*cot(theta).*tan(gama)+r.*sec(gama);


   %% Calculating Coefficient


a=ax.^2.*Dxx+ay.^2.*Dyy+az.^2.*Dzz+2.*ax.*ay.*Dxy+2.*ax.*az.*Dxz+2.*ay.
*az.*Dyz;


b=oy.*ay.*Dyy+oz.*az.*Dzz+ax.*oy.*Dxy+ax.*oz.*Dxz+(oy.*az+ay.*oz).*Dyz-
ax.*Dx-ay.*Dy-az.*Dz;

c=oy.^2.*Dyy+oz.^2.*Dzz+2.*oy.*oz.*Dyz-2.*oy.*Dy-2.*oz.*Dz+Kc;


function R = pmhRotationMatrixR(phi,theta,psi);

Theta = theta*pi/180;
Phi = phi*pi/180;
Psi = psi*pi/180;
%% XYZ rotation Phi-Z axis, Theta-Y axis, psi-X axis;
%
R =  [ cos(Phi)   -sin(Phi)  0
       sin(Phi)    cos(Phi)  0
      0           0         1 ] ...
      * ...
    [ cos(Theta)  0        sin(Theta)
      0           1         0
```

```
     -sin(Theta)  0         cos(Theta)] ...
     * ...
    [ 1           0         0
      0           cos(Psi)  -sin(Psi)
      0           sin(Psi)  cos(Psi)];
Return


function out = flatten(in)

out = reshape(in,[1 prod(size(in))]);

return;


function dlmcell(file,cell_array,varargin)
%% <><><><><><><><><><><><><><><><><><><><><><><><><><><><><><><><><><>
%%
% <><><><><>     dlmcell - Write Cell Array to Text File
<><><><><> %
%
<><><><><><><><><><><><><><><><><><><><><><><><><><><><><><><><><><><><>
%

%% Check input arguments
if nargin < 2
    disp('Error - Give at least two input arguments!');
    return;
elseif nargin > 4
    disp('Error - Do not give more than 4 input arguments!');
    return;
end
if ~ischar(file)
    disp(['Error - File input has to be a string (e.g. ' ...
        char(39) 'output.txt' char(39) '!']);
    return;
end;
if ~iscell(cell_array)
    disp('Error - Input cell_array not of the type "cell"!');
    return;
end;
delimiter = '\t';
append = 'w';
if nargin > 2
    for i = 1:size(varargin,2)
        if strcmp('-a',varargin{1,i}) == 1
            append = 'a';
        else
            delimiter = varargin{1,i};
        end;
    end;
end

%% Open output file and prepare output array.
output_file = fopen(file,append);
output = cell(size(cell_array,1),size(cell_array,2));
```

```
%% Evaluate and write input array.
for i = 1:size(cell_array,1)
for j = 1:size(cell_array,2)
    if numel(cell_array{i,j}) == 0
        output{i,j} = '';
    % Check whether the content of cell i,j is
    % numeric and convert numbers to strings.
    elseif isnumeric(cell_array{i,j}) || islogical(cell_array{i,j})
        output{i,j} = num2str(cell_array{i,j}(1,1));

    % Check whether the content of cell i,j is another cell (e.g. a
    % string of length > 1 that was stored as cell. If cell sizes
    % equal [1,1], convert numbers and char-cells to strings.
    %
    % Note that any other cells-within-the-cell will produce errors
    % or wrong results.
    elseif iscell(cell_array{i,j})
        if size(cell_array{i,j},1) == 1 && size(cell_array{i,j},1) == 1
            if isnumeric(cell_array{i,j}{1,1})
                output{i,j} = num2str(cell_array{i,j}{1,1}(1,1));
            elseif ischar(cell_array{i,j}{1,1})
                 output{i,j} = cell_array{i,j}{1,1};
            end;
        end;

     % If the cell already contains a string, nothing has to be done.
     elseif ischar(cell_array{i,j})
         output{i,j} = cell_array{i,j};
     end;

     % Cell i,j is written to the output file. A delimiter is appended
     % for all but the last element of each row.
     fprintf(output_file,'%s',output{i,j});
     if j ~= size(cell_array,2)
         fprintf(output_file,'%s',delimiter);
     end
end;
% At the end of a row, a newline is written to the output file.
fprintf(output_file,'\r\n');
end;

%% Close output file.
fclose(output_file);

end
```

REFERENCES

[1] Cormack, A.M., "Early two-dimensional reconstruction and recent topics stemming from It-Nobel lecture," *Science,* Vol. 209, no. 4464, pp. 1482-1486, 26 September 1980.

[2] Di Chiro, Giovanni, and Rodney A. Brooks, "The 1979 Nobel Prize in Physiology or Medicine," *Science,* Vol. 206, no. 4422, pp. 1060-1062, November 30, 1979.

[3] C. J. Ritchie, "Methods for reducing motion artifacts in computed tomography scans of the chest," Ph.D. Dissertation, Univ. Washington,seattle, 1993

[4] M. V. Green, J. Seidel, S. D. Stein, T. E. Tedder, K. M. Kempner, C. Kertzman, and T. A. Zeffiro, "Head movement in normal subjects during simulated PET brain imaging with and without head restraint," *J. Nucl. Med.*, vol. 35, pp. 1538–1546, 1994.

[5] U. E. Ruttimann, P. J. Andreason, and D. Rio, "Head motion during positron emission tomography: Is it significant?," *Psych. Res: Neuroimag.*, vol. 61, pp. 43–51, 1995.

[6] N.C. Linney, and P.H. Gregson , " Organ motion detection in ct images using opposite rays in fan-beam projection systems *IEEE Trans. Med. Imaging* Vol. 20, pp.1109-22, 2001.

[7] X. Pan, J. Siewerdsen, P. J. Riviere, W.A. Kalender, "Anniversary Paper: Development of x-ray computed tomography: The role of Medical Physics and AAPM from the 1970s to present," *Med. Phys.,* Vol. 35 , no. 8, August 2008, pp-3728-3739

[8] E. C. McCullough, "Photon attenuation in computed tomography," *Med. Phys.*, Vol. 2, pp. 307–320, 1975.

[9] E. C. McCullough and J. T. Payne, "X-ray-transmission computed tomography," *Med. Phys.*, Vol. 4, pp. 85–98, 1977.

[10] W. D. McDavid, R. G. Waggener, W. H. Payne, and M. J. Dennis, "Spectral effects on three-dimensional reconstruction from x rays," *Med. Phys.*, Vol. 2, pp. 321–324, 1975.

[11] W. D. McDavid, R. G. Waggener, W. H. Payne, and M. J. Dennis, "Correction for spectral artifacts in cross-sectional reconstruction from x-rays," *Med. Phys.*, vol. 4, pp. 54–57, 1977.

[12] M. R. Millner, W. H. Payne, R. G. Waggener, W. D. McDavid, M. J. Dennis, and V. J. Sank, "Determination of effective energies in CT calibration," *Med. Phys.*, vol. 5, pp. 543–545, 1978.

[13] B. K. P. Horn, "Fan beam reconstruction methods." *IEEE Proc.*, vol. 67, pp. 1616-1623, Dec. 1979.

[14] G. H. Glover and N. J. Pelc, "An algorithm for the reduction of metal clip artifacts in CT reconstructions," *Med. Phys.*, vol. 8, pp. 799–807, 1981.

[15] D. L. Parker, J. L. Couch, K. R. Peschmann, V. Smith, M. Jimbo, and E. C. Wang, "Design constraints in computed tomography: A theoretical review," *Med. Phys.*, vol. 9, pp. 531–539, 1982.

[16] R. G. Simpson, C. T. Chen, E. A. Grubbs, and W. Swindell, "A 4-MV CT scanner for radiation therapy: The prototype system," *Med. Phys.*, vol. 9, pp. 574–579, 1982.

[17] L. Feldkamp, L. Davix, and J. Kress, "Practical Cone- beam Algorithm," *J. Opt. Soc. Am.*, Vol. A 1, pp 612-619, 1984.

[18] C. R. Crawford and K. F. King, "Computed tomography scanning with simultaneous patient translation," *Med. Phys.*, vol. 17, pp. 967–982, 1990.

[19] G. Wang and M. W. Vannier, "Helical CT image noise-analytical results," *Med. Phys.*, vol. 20, pp. 1635–1640, 1993.

[20] W. Huda and J. V. Atherton, "Energy imparted in computed tomograpy," *Med. Phys.*, vol. 22, pp. 1263–1269, 1995.

[21] 102J. V. Atherton and W. Huda, "Energy imparted and effective doses in computed tomography," *Med. Phys.*, vol. 23, pp. 735–741, 1996.

[22] W. A. Kalender, H. Wolf, and C. Suess, "Dose reduction in CT by anatomically adapted tube current modulation. II. Phantom measurements," *Med. Phys.*, vol. 26, pp. 2248–2253, 1999.

[23] A. Polacin, W. A. Kalender, and H. Eidloth, "Simulation study of cerebral blood flow measurements in xenon-CT: Evaluation of washin/washout procedures," *Med. Phys.*, vol. 18, pp. 1025–1031, 1991.

[24] C. Ling, C. C. Rogers, and R. J. Morton, "Computed Tomography in Radiation therapy," *Raven*, New York, 1983.

[25] T. Takahashi, M. Nakagawa, M. Yoshida, and H. Takeuchi, "Highly stable solid-state x-ray detector array," *Med. Phys.*, vol. 19, pp. 1161–1166, 1992.

[26] T. Flohr, K. Stierstorfer, H. Bruder, J. Simon, A. Polacin, and S. Schaller, "Image reconstruction and image quality evaluation for a 16-slice CT scanner," *Med. Phys.*, vol. 30, pp. 832–845, 2003.

[27] S. Mori, M. Endo, T. Tsunoo, S. Kandatsu, and S. Tanada, "Physical performance evaluation of a 256-slice CT-scanner for four-dimensional imaging," *Med. Phys.*, vol. 31, pp. 1348–1356, 2004.

[28] M. Kachelrieß, S. Schaller, and W. A. Kalender, "Advanced single-slice rebinning in cone-beam spiral CT," *Med. Phys.*, vol. 27, pp. 754–772, 2000.

[29] C. Bontus, T. Köhler, and R. Proksa, "A quasiexact reconstruction algorithm for helical CT using a 3-Pi acquisition," *Med. Phys.*, vol. 30, pp. 2493–2502, 2003.

[30] J. J. Sonke, L. Zijp, P. Remeijer, and M. Van Herk, "Respiratory correlated cone beam CT," *Med. Phys.*, vol. 32, pp. 1176–1186, 2005.

[31] G. H. Chen, "An alternative derivation of Katsevich's cone-beam reconstruction formula," *Med. Phys.*, vol. 30, pp. 3217 _2003.

[32] M. Marxen, M. M. Thornton, C. B. Chiarot, G. Klement, J. Koprivnikar, J. G. Sled, and R. M. Henkelman, "MicroCT scanner performance and considerations for vascular specimen imaging," *Med. Phys.*, vol. 31, pp. 305–313, 2004.

[33] M. A. Anastasio, D. Shi, and X. Pan, "A preliminary investigation of local tomography for megavoltage CT imaging," *Med. Phys.*, vol. 30, pp. 2969–2980, 2003.

[34] J. G. Mainprize, K. A. Bloomquist, M.P. Kempston, and M. J. Yaffe, "Resolution at oblique incidence angles of a flat panel imager for breast tomosynthesis," *Med. Phys.*, vol. 33, pp. 3159–3164, 2006.

[35] J. H. Siewerdsen, M. J. Daly, B. Bakhtiar, D. J. Moseley, S. Richard, H. Keller, and D. A. Jaffray, "A simple, direct method for x-ray scatter estimation and correction in digital radiography and cone-beam CT," *Med. Phys.* , vol. 33, pp.187–197, 2006.

[36] D. J. Godfrey, H. P. McAdams, and J. T. Dobbins III, "Optimization of the matrix inversion tomosynthesis _MITS_ impulse response and modulation transfer function characteristics for chest imaging," *Med. Phys.*, vol. 33, pp.655–667, 2006.

[37] I. B. Tutar, R. Managuli, V. Shamdasani, P. S. Cho, S. D. Pathak, and Y. Kim, "Tomosynthesis-based localization of radioactive seeds in prostate brachytherapy," *Med. Phys.*, vol. 30, pp. 3135–3142, 2003.

[38] G. M. Stevens, R. Fahrig, and N. J. Pelc, "Filtered backprojection for modifying the impulse response of circular tomosynthesis," *Med. Phys.*, vol. 28, pp. 372–380, 2001.

[39] S. Li and H. Jiang, "A practical method for three-dimensional reconstruction of joints using a C-arm system and shift-and-add algorithm," *Med. Phys.*, vol. 32, pp. 1491–1499, 2005.

[40] Y. Chen, J. Y. Lo, and J. T. Dobbins III, "Importance of point-by-point back projection correction for isocentric motion in digital breast tomosynthesis: Relevance to morphology of structures such as microcalcifications," *Med. Phys.*, vol. 34, pp. 3885–3892, 2007.

[41] T. Wu, R. H. Moore, E. A. Rafferty, and D. B. Kopans, "A comparison of reconstruction algorithms for breast tomosynthesis," *Med. Phys.*, vol. 31, pp. 2636–2647, 2004.

[42] Y. Zhang, H.-P. Chan, B. Sahiner, J. Wei, M. M. Goodsitt, L. M. Hadjiiski, J. Ge, and C. Zhou, "A comparative study of limited-angle conebeam reconstruction methods for breast tomosynthesis," *Med. Phys.*, vol. 33, pp. 3781–3795, 2006.

[43] J. T. Rakowski and M. J. Dennis, "A comparison of reconstruction algorithms for C-arm mammography tomosynthesis," *Med. Phys.*, vol. 33, pp. 3018–3032, 2006.

[44] Costello P, Damian E, Dupuy DE, et al., " Spiral CT of the thorax with reduced volume of contrast material: a comparative study," *Radiology*, vol. 183, pp. 663–666, 1992

[45] Colsher J. G., Pelc N. J., "Computerized tomography systems and performance," *Radiology*, Taveras JM, Ferrucci JT, eds. Radiology. Philadelphia: J.B. Lippincott, pp. 1-13, 1987.

[46] Parker D L, Smith V and Stanley J H, "Dose minimization in computed tomography overscanning," *Med. Phys.*, vol. 8, pp. 706-1, 1981

[47] H. I. Goldberg, R. G. Gould, I. M. Feuerstein, J. S. Sigeti, and M. J. Lipton, "Evaluation of ultrafast CT scanning of the adult abdomen", *Invest. Radiology*, vol. 24, pp.537 - 543, 1989.

[48] Gould RG. Principles of ultrafast computed tomography: historical aspects, mechanism of action, and scanner characteristics. In: Stanford W, Rumberger JA, eds. *Ultrafast Computed Tomography in Cardiac Imaging: Principles and Practice*. Mount Kisco, NY: Futura, pp.1-15, 1992.

[49] Mayo J. R., Müller N. L. and Henkelman R. M., "The double-fissure sign: a motion artifact on thin-section CT scans," *Radiology*, vol. 165, pp. 580-81, 1987

[50] Crawford C.R., Godwin J.D., and Pelc N.J., "Reduction of motion artifacts in computed tomography," *proc IEEE EMBS*, pp. 485-486, 1989.

[51] Moore S.C., and Judy P.F., "Cardiac computed tomography using redundant-ray prospective gatting," *Med. Phys.*, vol. 14, pp. 193-196, 1987.

[52] Herman G. T., "Reconstruction and imaging of the beating heart," *Mayo Clin Proc., Suppl.* 57, pp. 92-95, Jul. 1982.

[53] Godwin JD, Johnson GA, Fram EK., "A phantom for testing ECG-gated computed tomography of the heart," *Invest Radiol.*, Vol. 19, no. 4, pp. 279-83, Jul-Aug. 1984.

[54] Y Oyama, T Uji, T Hirayama, Y Inada, T Ishikawa and M Fujii, "Gated cardiac imaging using a continuously rotating CT scanner," *AJR Am J Roentgenol*, vol. 142, pp. 865–876, 1984.

[55] Garnic JD, Moore SC, Judy PF, Harrington DP, Lois J, Levin DC., "Prospectively gated cardiac CT. Preliminary results in normal and postinfarction animal models," *Invest Radiol*., vo. 18, no. 5, pp. 419-24, sept.-Oct.1983

[56] Morin R. L. and, D E Raeside D. E., "A pattern recognition method for the removal of streaking artifact in computed tomography," *Radiology*, vol. 141, pp. 229-233, 1981.

[57] Joseph PM, Spital RD., "A method for correcting bone induced artifacts in computed tomography scanners," *J Comput Assist Tomogr*., Vol. 2, no. 1, pp. 100-108, Jan. 1978.

[58] Pelc N. J., and Glover G. H., "Method for reducing image artifacts due to projection measurement inconsistencies. *U. S. Patent* 4,580,219, 1986.

[59] U. Bhowmik, S. Aravetti, R. Adhami, "An Innovative Approach to Reduce Streaking Artifacts in FDK Based 3D Cone-beam Tomography" *IEEE Southeastcon 2011*, Nashville, USA.

[60] Yang CK, Orphanoudakis SC, Strohbehn JW. A simulation study of motion artefacts in computed tomography. *Phys Med Biol.*, vol. 27, no. 1, pp. 51-61, Jan. 1982.

[61] Carl R. Crawford," Senior Member, IEEE, Kevin F. King, Cameron J. Ritchie, amd J. David Godwin, "Respiratory Compensation in Projection Imaging Using a Magnification and Displacerrient Model," *IEEE trans. on med. Imag*., vol. 15, no. 3, june 1996

[62] Ritchie CJ, Crawford CR, Godwin JD, King KF, Kim Y., "Correction of computed tomography motion artifacts using pixel-specific back-projection," *IEEE Trans Med Imaging*. Vol. 15, no. 3, pp. 333-42, 1996.

[63] H. W. Korin, J. P. Felmee, R. L. Ehman, and S. J. Riederer, "Adaptive tecnique for three-dimensional MR imaging of moving structures," *Radiology*, vol. 177, pp. 217–221, 1990.

[64] Bergin CJ, Noll DC, Pauly JM, Glover GH, Macovski A., "MR imaging of lung parenchyma: a solution to susceptibility," *Radiology*, vol. 183, no. 3, pp. 673-676, 1992.

[65] Noll DC, Meyer CH, Pauly JM, Nishimura DG, Macovski A., "A homogeneity correction method for magnetic resonance imaging with time-varying gradients," *IEEE Trans Med Imaging*, Vol. 10 no. 4, pp.629-637. 1991

[66] R. Goldstein, E. Margaret, and W. Dube, "A Head Motion Measurement System Suitable for Emission Computed Tomography," *IEEE Trans. Of Medical Imaging*, Vol. 16, No. 1, pp 17-27, February 1997.

[67] R.R. Fulton, S**.** Eberl, S.R. Meikle, M. Braun, "**A** Practical 3D Tomographic Method for Correcting Patient Head Motion in Clinical SPECT," *IEEE Trans. On Nuclear Science***,** Vol. 46, No. 3, June 1999.

[68] R.D. Beach, H.C. Gifford, S. Shazeeb, P.P. Bruyant, B. Feng, M.A. Gennert, S. Nadella, and M.A. King, "Stereo Infrared Tracking to Monitor and Characterize rigid-body Motion and Respiration During Cardiac SPECT Imaging:Progress Towards Robust Clinical Utilization," *in Proc. Of IEEE Nuclear Science Symp. Conf. Rec.*, Vol. 3, pp.1731-1735, Oct 23-29, 2005

[69] S. Sarkar, M. A. Oghabian, I. Mohammadi, A. Mohammadpour, and A. Rahmim , "A Linogram/Sinogram Cross-Correlation Method for Motion Correction in Planar and SPECT Imaging," *IEEE Trans. On Nuclear Science*, Vol. 54, No. 1, February 2007.

[70] L.Weiguo and R. Mackie, "Tomographic Motion Detection and Correction Directly in Sinogram space," *Phys. Med. Biol*, Vol. 47, pp- 1267-1284, 2002.

[71] S. Ens, J. Müller, B. Kratz and T.M. Buzug "Sinogram-Based Motion Detection in Transmission Computed Tomography,"*Proc. 4th European Congress for Medical and Biomedical Engineering, Springer IFMBE Series*, Vol. **22**, p.505–508, 2008.

[72] A. Rahmim, P. Bloomfield, S. Houle, M. Lenox, C. Michel, K. R.Buckley, T. J. Ruth, V. Sossi, "Motion Compensation in Histogram-Mode and List-Mode EM Reconstruction: Beyond the Event-Driven Approach", *IEEE. Trans. Nucl. Sci.* vol. 51, pp. 2588-2596, 2004.

[73] M.B. Ooi, S. Krueger, W.J. Thomas, S.V. Swaminathan and T.R. Brown, "Prospective real-time correction for arbitrary head motion using active markers," *Magn Reson Med*, vol. **62, no.** 4, pp. 943–954, 2009

[74] L. Qin, P. van Gelderen, J.A. Derbyshire, F. Jin, J. Lee and J.A. de Zwart, *et al.*, " Prospective head-movement correction for high-resolution MRI using an in-bore optical tracking system," *Magn Reson Med*, vol. 62, no**.** 4, pp. 924–934, 2009.

[75] Schäfer D., Bertram M., Conrads N., Wiegert J., Rose and G., Rasche V., " Motion compensation for cone-beam CT based on 4D motion field of sinogram tracked markers", *In the Proceedings of CARS'*, pp.189~194, 2004.

[76] Beddar A.S., Kainz K, Briere T.M., "Correlation between internal fiducial tumor motion and external marker motion for liver tumors imaged with 4D-CT," *Int J Radiat Oncol Biol Phys*, vol. 67, pp. 630–638, 2007.

[77] D.P. Gierga, Brewer J, G.C. Sharp, "The correlation between internal and external markers for abdominal tumors: implications for respiratory gating," *Int J Radiat Oncol Biol Phys.*, vol. 61, pp. 1551–1558, 2005.

[78] N. Rezvani, D. Arullah, K. Jackson, D. Mosley and J Siewerdsen, "An Open Source Cone-Beam CT Reconstruction Tool for Imaging Research," *Poster AAPM*, 2007.

[79] Jiang Hsieh, "Computed Tomography: Principles, design, artifacts, and recent advances," Bellingham, Washington, USA, *SPIE PRESS*, 2002.

[80] A.C. Kak and M. Slaney, "Principle of Tomographic Imaging," *IEEE Press*, 1999

[81] L. A. Shepp and B.F. Logan, "The Fourier Reconstruction of a Head Section," *IEEE trans. On Nuclear Science*, Vol. NS-21, June 1974.

[82] J. Zhu, S. W. Lee, Y. Ye, S. Zhao and G. Wang, "X-ray Transform and 3D Radon Transform for ellipsoids and tetrahedral," *J. of X-ray Sci. and Tech*, Vol. 12, pp. 215- 229, 2004

[83] S. R. Dean, "The Radon Transform and Some of its Application," *Dover Publications, Inc, Mineola, NY*, 1993

[84] Richard Hartley, and Andrew Zisserman, "*Multiple View Geometry in computer vision*," Cambridge University Press, First Edition, 2000.

[85] James D. Foley, Adrries Van Dam, Steven K. Feiner, and John F. Hughes, "Computer Graphics Principle and Applications", *Addison- Wesley Publishing Company*, 2nd Edition, 1996.

[86] U. Bhowmik and R. Adhami, "Motion Artifacts Compensation in FDK based 3D cone-beam Tomography Using Correlation of X-Ray Projections," *Proceedings of The International Conference on Image Processing, Computer Vision & Pattern Recognition (IPCV 2011)*, July 18-21, 2011, Las Vegas, USA.

[87] U. Bhowmik and R. Adhami, "A Correlation and LS-SVM Based Approach to Mitigate Motion Artifacts in FDK Based 3D Cone-Beam Tomography," *International Conference of the IEEE Engineering in Medicine and Biology Society (EMBC '11)*, Boston, USA

[88] U. Bhowmik, M. Iqbal, and R. Adhami, "A Head Motion Measurement System Suitable for 3D Cone-beam Tomography Using Markers," submitted to *IEEE Trans. Of Medical Imaging*

[89] D. P. Boyd and M. J. Lipton, "Cardiac computed tomography," *Proc. IEEE*, vol. 71, pp. 298–307, Mar. 1983.

[90] C. R. Crawford, J. D. Godwin, and N. J. Pelc, "Reduction of motion artifacts in computed tomography," in *Proc. IEEE Engineering Medicine and Biology Society*, vol. 11, 1989, pp. 485–486.

[91] M. Menke, M. S. Atkins, and K. R. Buckley, "Compensation methods for head motion detected during PET imaging," *IEEE Trans. Nucl. Sci.*, vol. 43, pp. 310–317, Feb. 1996.

[92] Imad Ali, Salahuddin Ahmad, Nesreen Alsbou, Dale-Michael Lovelock, Sergey Kriminski and Howard Amols, "Correction of image artifacts fromtreatment couch in cone-beam CT from kV on-board imaging," *Journal of X-Ray Science and Technology*, Vol. 19, pp. 321-332, 2011.

[93] Ali I., Alsbou N., Herman T., Ahmad S.," An algorithm to extract three-dimensional motion by marker tracking in the kV projections from an on-board imager: four-dimensional cone-beam CT and tumor tracking implications," *J Appl Clin Med Phys*, Vol.12(2), pp. 223-238, 2011 Feb 1